UNIVERSIDADE D COIMBRA
FACULDADE DE CIÊNCIAS E TECNOLOGIA

Maria João Anjo Carriço

Monte Carlo Investigations for a Novel Small-Animal Proton Radiographic Setup based on a Pixelated Silicon Detector and Energy Stacking

Thesis submitted to the
University of Coimbra for the degree of
Master in Biomedical Engineering

Supervisors:
Prof. Dr. Paulo Alexandre Vieira Crespo (Physics Department, University of Coimbra)
Prof. Dr. Katia Parodi (Chair of Experimental Physics, LMU Munich)

Coimbra, 2018

This work was developed in collaboration with:

University of Coimbra, Faculty of Science and Technology
Physics Department

Ludwig-Maximilians-Universität München, Faculty of Physics
Chair of Experimental Physics, Medical Physics

In order to succeed, your desire for success should be greater than your fear of failure. - Albert Einstein

To my Mom.

Acknowledgments

First of all, I would like to thank Prof. Dr. Paulo Crespo for being so passionate about his work and for transmitting that passion to his students. Thank you for inspiring me.

Prof. Dr. Katia Parodi gave me the opportunity of developing my Thesis at the Chair of Medical Physics, and for that, I will be forever grateful. Thank you for the support and for always finding the time to help me. Even the shortest conversations on our way from the U-Bahn to the office or in the middle of the hallway were always enlightening.

To Matthias, I want to thank all his patience and time. Thank you for always being there for me, for not letting me give up, for always pushing me to try harder and for making me realize that in order to succeed we have to fail first. Sometimes it was not easy but thank you for annoying me every day; now I know it was for my own good.

I want to thank all my former colleagues in Garching for letting me be a part of the Physicists family. My special thanks go to Ines, for starting the project and helping me whenever I needed, to Sebastian, for all his ideas, for all his help and for being always so available even with one thousand things to do, and to all the ones who made my days at the office less boring (particularly the ones who brought cake!).

To all my friends in Coimbra, I want to thank all the moments we spent together. Thank you for putting up with my peculiar temper and for making these five years the best of my life. Together we made mistakes, we learned, we grew, and we created memories that will comfort us in this new chapter of our lives.

Last but not least, I want to thank my family. More importantly, I want to thank my Mom. Everything I had, have and will have will always be thanks to and for you. Your unconditional love, support, and sacrifices allowed me to get to where I am. Thank you for being the most important person in my life. I love you.

Resumo

O cancro é um dos maiores problemas de saúde pública, sendo a segunda maior causa de morte no mundo. Mais de 100 tipos diferentes de cancro foram reportados até ao presente, existindo diversas abordagens para os combater. Uma delas, um tipo de radioterapia, é a terapia com protões.

O conceito de *image-guidance* é crucial para melhorar a precisão de estudos como a irradiação protónica de pequenos animais. Este projeto investigou a viabilidade de uma nova configuração para imagiologia de radiografias protónicas de pequenos animais baseada num detetor de silício pixelizado e na noção de empilhamento de energias. O método para verificação de posição, e medição direta da distribuição bidimensional da Espessura Equivalente a Água (WET) de um objeto com o tamanho de um pequeno animal, consistiu no varrimento de um fantoma com 2 × 2 × 2 cm^3 de água, includindo quatro inserções de diferentes materiais (0,3 × 0,3 × 2 cm^3 cada), com 61 feixes de protões com energias entre 45 e 75 MeV. A deposição de energia foi registada num modelo simplificado de um detetor CMOS pixelizado comercialmente disponível (1024 × 512 pixels com 48 μm de lado e uma espessura sensível de 2 μm), colocado em diferentes distâncias a jusante do fantoma. Para cada pixel do detector, a deposição de energia versus a energia inicial do feixe de protões foi registada e convertida em valores de WET através de uma decomposição de sinal, usando uma matriz de consulta baseada em Monte Carlo (LUT).

Para um conjunto de parâmetros de simulação de Monte Carlo, os valores de WET foram obtidos com uma precisão de cerca de 96,1%. Resoluções espaciais submilimétricas de (0,59 ± 0,02) mm e (0,67 ± 0,01) mm foram obtidas em ambas as dimensões. Com uma dose total para o objeto de 69,7 mGy, o tempo total de aquisição radiográfica para esta abordagem foi estimado em 14 a 33 minutos, dependendo do acelerador utilizado.

Palavras-chave: Terapia com Protões, Radiografia Protónica, Estudos Pré-Clínicos, Simulações de Monte Carlo, Espessura Equivalente a Água.

Abstract

Cancer is one of the biggest public health issues, being the second leading cause of death worldwide. More than 100 different types of cancer have been reported until the present day, and there are several approaches to combat them. One of them, a type of radiation therapy, is proton therapy.

Image-guidance is crucial for improving the precision of experiments such as small-animal proton irradiation. This project investigated the feasibility of a novel small-animal proton radiographic imaging setup based on a pixelated silicon detector and the concept of energy stacking. The method for position verification, and direct measurement of the two-dimensional Water Equivalent Thickness (WET) distribution of a small-animal sized object, consisted of scanning a $2 \times 2 \times 2$ cm^3 water phantom, including four different material inserts ($0.3 \times 0.3 \times 2$ cm^3 each), with 61 proton energies ranging from 45 to 75 MeV. Different beam shapes were tested. Energy deposition was scored in a simplified model of a commercially available pixelated CMOS detector (1024×512 pixels with 48 μm pixel pitch, 2 μm sensitive thickness), placed at varying distances downstream of the phantom. For each detector pixel, the energy deposition versus initial proton beam energy was recorded and converted to WET values by a signal decomposition using a Monte Carlo-based lookup-table (LUT) matrix.

For a set of Monte Carlo simulation parameters, including the use of a combination of two perpendicular rectangular proton beams, WET values were obtained with an accuracy of about 96.1%. Sub-millimeter spatial resolutions of (0.59 ± 0.02) mm and (0.67 ± 0.01) mm were obtained in both dimensions. With a total dose to the object of 69.7 mGy, the entire radiographic acquisition time for this approach was estimated to range from 14 to 33 minutes, depending on the used accelerator.

Keywords: Proton Therapy, Proton Radiography, Pre-Clinical Studies, Monte Carlo Simulations, Water Equivalent Thickness.

List of Acronyms

ASCII American Standard Code for Information Interchange

BP Bragg Peak
BPD Bragg Peak Decomposition

CG Combinatorial Geometry
CMOS Complementary Metal Oxide Semi-Conductor
CMOS APS Complementary Metal Oxide Semi-Conductor Active Pixel Sensor
CSDA Continuous Slowing Down Approximation
CT Computed Tomography

FLAIR FLUKA Advanced Interface
FLUKA Fluktuierende Kaskade
FWHM Full Width at Half Maximum

GEM Gas Electron Multiplier
GUI Graphical User Interface

IAEA International Atomic Energy Agency
IMRT Intensity-Modulated Radiation Therapy

LLUMC Loma Linda University Medical Center
LSF Line-Spread Function
LUT Lookup-Table

MC Monte Carlo
MCS Multiple Coulomb Scattering
MCTP Monte Carlo-based Treatment-Planning
MLP Most Likely Path
MTF Modulation Transfer Function

NCI National Cancer Institute
NRMSE Normalized Root-Mean-Square Error

pCT Proton Tomography
PET Positron Emission Tomography
PF Peak Finding
PGI Prompt Gamma-Ray Imaging
PMMA Poly(Methyl Methacrylate)
pRG Proton Radiography
PSD Position-Sensitive Detector

RE Relative Error
RERD Residual Energy-Range Detector
RMSE Root-Mean-Square Error
ROI Region of Interest

SARRP Small Animal Radiation Research Platform
SD Signal Decomposition
SIRMIO Small Animal Proton Irradiator for Research in Molecular Image-guided Radiation-Oncology
SOBP Spread-Out Bragg Peak
SP Stopping Power
SPR Stopping Power Ratio

VMAT Volumetric Modulated Arc Therapy

WEPL Water Equivalent Path Length
WET Water Equivalent Thickness

List of Figures

List of Tables

Contents

1

Introduction

This chapter will explore the context of this thesis, giving an insight of its overall interest and motivation (section 1.1). Section 1.2 will establish the main goals and the last section will present the outline of the document (section 1.3).

1.1 Contextualization and Motivation

Cancer is one of the biggest public health issues, being the second leading cause of death worldwide [1, 2] (figure 1.1). According to the National Cancer Institute (NCI), it can be described as a group of diseases in which abnormal cell growth can lead to invasion and spreading of these anomalous cells throughout the nearby tissue, arising tumors in many parts of the body [3].

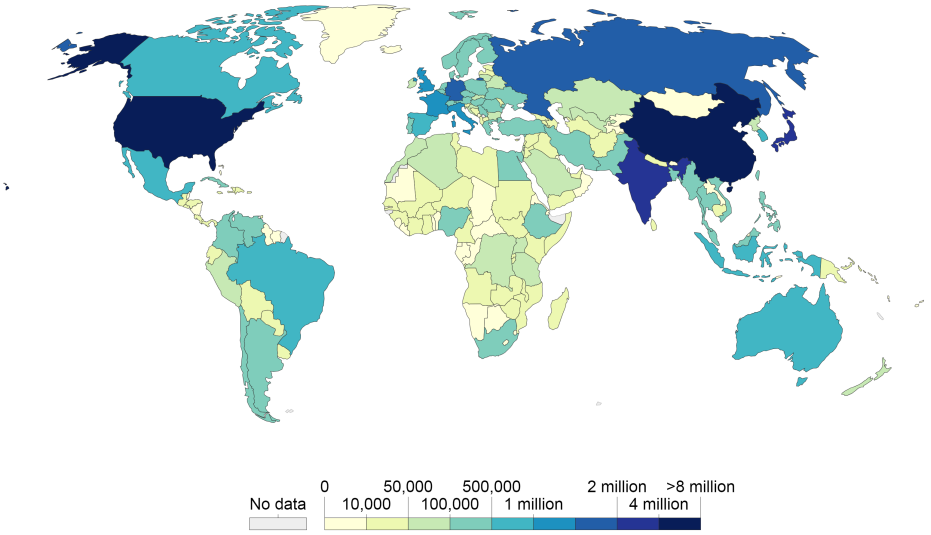

Figure 1.1: Total number of people suffering from any type of cancer at a given time, during the year 2016 [3].

Many are the factors responsible for this illness, but the most relevant ones are tobacco, alcohol abuse, obesity, infections, exposure to ionizing radiation and environmental contaminants [4]. Although there are some typical symptoms and signs, an accurate diagnosis requires investigation via medical imaging and confirmation via biopsy.

According to the World Cancer Report 2014 provided by the World Health Organization, lung cancer, prostate cancer, colorectal cancer, and stomach cancer are the most common types of cancer in the male population, while breast cancer, colorectal cancer, lung cancer, and cervical cancer are the most prevalent cancers in the female population [5].

More than 100 different types of cancer have been reported until the present day, and there are several approaches to combat them. Amongst the most common existing treatments, there is surgery, chemotherapy, and radiation therapy [6]. Depending on the case, these three modalities can be used separately or combined. Thus, an effective treatment is the one that combines tumor control with low side-effects, determining the probability of cancer recurrence afterwards. With the aim of obtaining more effective treatments, new treatment variations have been proposed throughout the years. One of them, a type of radiation therapy, is proton therapy.

Radiation therapy, also called radiotherapy, is a type of cancer treatment that makes use of high-energy X-rays — ionizing radiation — to harm the DNA of cancerous tissue and thus provide tumor control. The physical quantity related to this principle is dose, the energy deposition in the tissue. The depth-dose profile of high-energy X-rays is depicted in the figure below (figure 1.2).

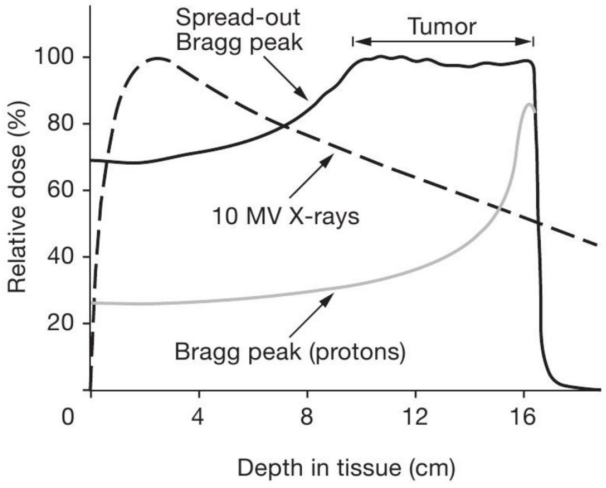

Figure 1.2: Comparison between the depth-dose profiles of high-energy X-rays and proton beams [7].

Analyzing figure 1.2, one can state that the relative dose of photons (X-rays) decreases with increasing depth in tissue (dashed line). In other words, there is a build-up region close to the surface, resulting in a large delivery of energy. Consequently, to reach deeper tumors, undesired amounts of energy will be deposited in the surrounding healthy tissue. Taking into account the radio-sensitivity of some organs, this can be profoundly harmful.

Techniques like Intensity-Modulated Radiation Therapy (IMRT) and Volumetric Modulated Arc Therapy (VMAT) try to compensate this side effect of radiotherapy by providing *highly conformal dose distributions with improved target volume coverage and sparing of normal tissues* [8, 9]. On the other hand, the hypothesis of using relativistic proton beams from particle accelerators to treat deep-seated tumors in humans was first introduced by Robert Wilson in 1946 [10, 11]. Going back to figure 1.2, in contrast to photons, the depth-dose curve of protons (gray line) is described in an inverse way, corresponding the highest energy deposition to the end of the particle range — the so-called Bragg peak. Moreover, the overlap of various Bragg curves with different beam energies allows the complete coverage of the tumor volume — the Spread-Out Bragg peak (SOBP). As a result — and if information such as patient anatomy or proton stopping power is well-known — it is possible to fully exploit the characteristics of these particles and hence obtain more conformal therapies, with a more precise and accurate dose deposition to the target volume, sparing the healthy surrounding tissue.

In light of this, proton therapy requires that two out of several main aspects are taken into account. Firstly, in order to assess the dose distribution to be delivered, the patient anatomy has to be known. Secondly, the exact position of the energy deposition in the target volume needs to be acknowledged, which means the proton range is a crucial measure. Uncertainties in the calculation of the proton range can result in inconsistencies between the planned and the delivered dose distribution. These inconsistencies can translate into over-dosage in the healthy tissue surrounding the tumor, causing posterior detrimental side effects, or under-dosage at the tumor site, leading to inefficient tumor treatment. As X-ray Computed Tomography (CT) images do not provide a direct functional relationship concerning the range of ions — due to the different physics of X-rays/proton interactions — large safety margins are employed around the target volume during the treatment planning [12]. These safety margins try to attenuate the effects of range uncertainties of about 1% to 3% [13], which also include patient position and organ motion and vastly constraint the performance of this technique.

Reducing the size of the safety margins would greatly improve the outcomes of proton therapy. In this regard, there are many ongoing pieces of research related to this topic and *in vivo* range verification. Techniques such as Positron Emission Tomography (PET), Prompt Gamma-Ray Imaging (PGI) or ionoacoustic are good examples [14–16].

Another important concept related to radiotherapy, proton therapy, and range verification, in general, is imaging. Radiography and tomography are the two primary modalities for position verification and treatment planning, correspondingly. Radiography is a technique that uses radiation energy to penetrate the objects being studied. Depending on the inherent density, thickness or structural composition, certain amounts of energy will be absorbed inside the tissue, while other amounts will reach the detector positioned behind the object. From the information scored within the detector, two-dimensional flat images will be generated thus yielding a representation of the structure of the tissues. The transition to tomography requires the generation of three-dimensional cross-sectional images from the original two-dimensional flat images. The difference between conventional X-ray radiography and proton radiography are the energy beams. While the first case uses X-ray beams, the second case uses proton beams. Comparing both of them in terms of image quality, the former one provides better spatial resolution, while the latter one has the advantage of an improved density resolution [17].

Finally, one needs to take into account that new techniques always go through an extensive testing process, before they can be safely introduced as common human treatments. When it comes to X-rays, several setups make use of animal models to perform research related to tumor response and control, tumor micro-environment characterization, amongst many others. One of them — available at the University Hospital in Großhadern, Munich — is the Small Animal Radiation Research Platform (SARRP), manufactured by Xstrahl (figure 1.3).

Figure 1.3: Small Animal Radiation Research Platform (SARRP) [18].

When it comes to protons, there are also some setups available for testing; however, none of them is as complete as, for example, the SARRP. Due to this fact, the investigation of a new system for proton radiography of small-animals motivates the present work.

1.2 Objectives

According to the notions presented in the previous section, the goal of this thesis is to develop a novel small-animal proton radiographic imaging setup based on a pixelated silicon detector and the concept of energy stacking — further explained in section 4.1. The developed setup should be reliable, consistent and valuable.

In order to analyze the suitability of the presented proposal and its outcomes, several steps will be carried out, such as the inclusion of evaluation metrics for performance assessment and the calculation of the time resources required for such an irradiation scheme. Moreover, the central ambition of this work is the development of a robust method for Water Equivalent Thickness (WET) reconstruction.

All the mentioned stages, as well as their essential concepts, will be explained in subsequent chapters.

1.3 Outline of the Dissertation

This document is structured as follows: chapter 2 explores the theoretical background behind the developed work and chapter 3 analyzes the current state of proton radiography, referring to several studies. In chapter 4, an overview of all the materials and methods used for the experiments, simulations and data evaluation is presented, and the obtained outcomes are further critically investigated and analyzed in chapter 5. Finally, chapter 6 highlights the main findings of the thesis, proposing new ideas and suggestions for future work.

2

Theoretical Background

In this chapter, the essential aspects regarding the physical and theoretical background of this thesis will be presented.

2.1 Interaction of Protons with Matter

Heavy charged particles, such as protons (when compared to electrons), interact with matter via various processes as they traverse it. These interactions have electromagnetic and hadronic nature and result in the pronounced energy deposition at the end of the particle range, the so-called Bragg peak [19].

Protons have a rather continuous kinetic energy loss due to numerous interactions with atomic electrons, the inelastic Coulomb interactions. Most of these protons traverse matter in an approximately straight line as they encounter electrons, as their rest mass is almost 2000 times larger than the electron rest mass. When near to atomic nuclei, their trajectory undergoes a deflection from the initial *straight-line* path owing to repulsive elastic Coulomb interactions [10].

Comparing elastic and non-elastic nuclear reactions between the atomic nucleus and protons, the latter are less regular but have a more significant impact [10]. Moreover, protons can lose energy via radiative losses. However, the *Bremsstrahlung emitted from the collision of heavy charged particles with an atom can be ignored because particles are not accelerated* [20]. In other words, the proton Bremsstrahlung contribution is negligible when considering therapeutic proton beam energies (50 – 250 MeV) and is only important for electrons. Figure 2.1 and table 2.1 depict and summarize the relevant aspects of all the named proton interaction processes.

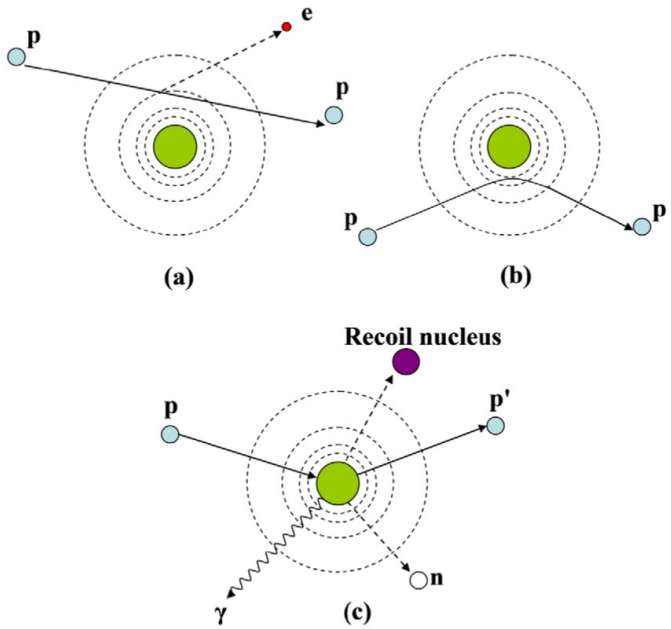

Figure 2.1: Proton interaction mechanisms. (a) Energy loss via inelastic Coulomb interactions, (b) deflection of proton trajectory by repulsive Coulomb elastic scattering with nucleus, (c) removal of primary proton and creation of secondary particles via non-elastic nuclear interaction (p: proton, e: electron, n: neutron, γ: gamma rays) [10].

Table 2.1: Summary of proton interaction types, targets, ejectiles, influence on projectile, and selected dosimetric manifestations [10].

Interaction Type	Interaction Target	Principal Ejectiles	Influence on Projectile	Dosimetric Manifestation
Inelastic Coulomb scattering	Atomic electrons	Primary proton, ionization electrons	Quasi-continuous energy loss	Energy loss determines range in patient
Elastic Coulomb scattering	Atomic nucleus	Primary proton, recoil nucleus	Change in trajectory	Determines lateral penumbral sharpness
Non-elastic nuclear reactions	Atomic nucleus	Secondary protons and heavier ions, neutrons, and gamma rays	Removal of primary proton from beam	Primary fluence, generation of stray neutrons, generation of prompt gammas for in vivo interrogation
Bremsstrahlung	Atomic nucleus	Primary proton, Bremsstrahlung photon	Energy loss, change in trajectory	Negligible

2.1.1 Stopping Power

The linear stopping power, or energy loss rate of ions, is characterized by the average rate at which an ion with energy E loses energy per unit path length dx (equation 2.1):

$$S = -\frac{dE}{dx}. \tag{2.1}$$

The stopping power can also be expressed independent of the mass density of the traversed medium, ρ, by the so-called mass stopping power, which is expressed in units of mass thickness (MeVcm^2/g) (equation 2.2) [21]:

$$\frac{S}{\rho} = -\frac{dE}{\rho dx}. \tag{2.2}$$

The total linear stopping power is a combination of different contributions. As previously stated, the proton Bremsstrahlung, or radiative stopping power, can be neglected for heavy charged particles in the therapeutically relevant energy range [20]. Therefore, the total linear stopping power is the sum of collisional loss and nuclear energy loss (equation 2.3):

$$S = S_{col} + S_{nuc}. \tag{2.3}$$

In the equation above, S_{col} is the collision or electronic stopping power, coming from the inelastic Coulomb scattering with atomic electrons, and S_{nuc} is the nuclear stopping power, coming from the elastic collisions with atomic nucleus.

Energy loss due to the elastic scattering of heavy charged particles with a nucleus in the energy range lower than 10 keV cannot be ignored (figure 2.2) [20]. Therefore, considering the relevant energy range for protons with regard to therapy (50 – 250 MeV), the S_{nuc} component can be neglected except for the end of the particle range. As a consequence, protons will deposit the majority of their energy via inelastic Coulomb collisions with the atomic electrons (figure 2.2) [20].

Collisional energy loss can be described by the Bethe-Bloch equation, the most important equation in proton therapy (equation 2.4) [10, 22, 23]:

$$S = -\frac{dE}{dx} = 4\pi N_A \rho r_e^2 m_e c^2 \frac{Z}{A}\frac{z^2}{\beta^2}\left[\ln\left(\frac{2m_e c^2\beta^2}{I(1-\beta^2)}\right) - \beta^2 - \frac{\delta}{2} - \frac{C}{Z}\right], \tag{2.4}$$

in which N_A is the Avogadro number, r_e and m_e are the classical radius and mass of an electron, respectively, c is the speed of light, Z and A are the atomic number

and the atomic weight of the absorbing material, respectively, z is the charge of the projectile, $\beta = v/c$ in which v represents the velocity of the projectile and I is the mean excitation potential of the absorbing material [24]. The two latter terms inside the square brackets are correction terms, in which the first one, the density effect correction, arises *from the shielding of remote electrons by other close electrons* [10]. This results in a reduction of energy loss at higher projectile energies. The second one, the shell correction, is important for low energies where the velocity of the particle is close to the velocity of the atomic electrons. Furthermore, these corrections embroil relativistic theory and quantum mechanics, raising their need of being taken into account when very low or high proton energies are used in calculations [10].

All the above-described parameters influence the particle energy loss rate. Analyzing equation 2.4, one can highlight the direct proportionality of the stopping power with the square of the projectile charge and with the inverse square of its velocity, meaning an increase in the energy loss with decreasing velocity. On the other hand, there is also a direct proportionality with the electron density of the absorber material. This relation can be explained by the fact that energy loss is mainly due to Coulomb interactions between the proton and atomic electrons [10].

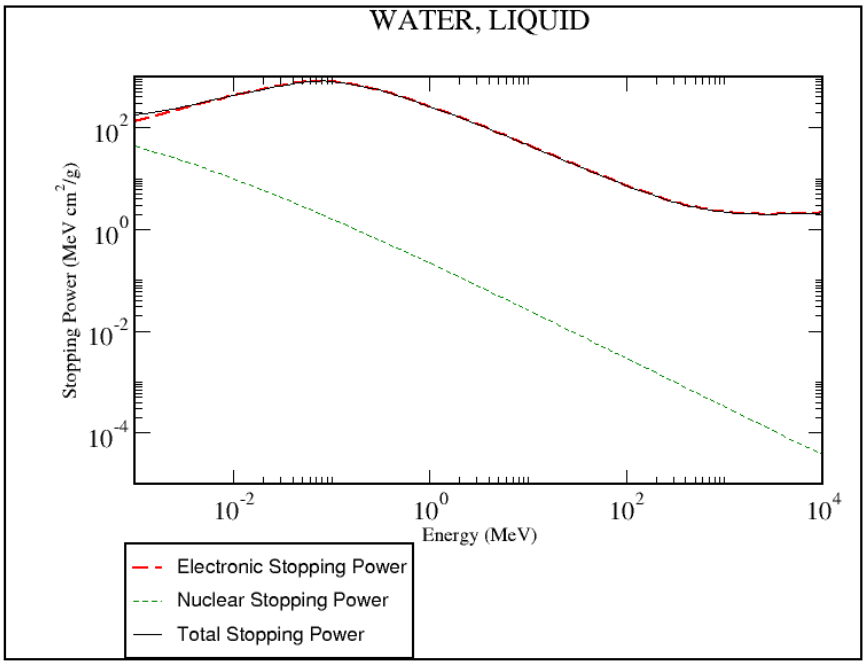

Figure 2.2: Electronic, nuclear and total stopping power of protons in water [25].

Figure 2.2 emphasizes some of the dependencies of equation 2.4. For low energies, approximately 0.1 MeV, the stopping power decreases since recombination processes

between the projectile particles and target atomic electrons are reducing the charge parameter, z, to an effective charge z_{eff}.

This effective charge can be approximated by the semi-empirical Barkas formula (equation 2.5) [26]:

$$z_{eff} = z\left(1 - \exp\left(-125\beta z^{-\frac{2}{3}}\right)\right). \tag{2.5}$$

Combining this decreasing parameter (z_{eff}) at low energies with the $1/\beta^2$ dependence in equation 2.4 arises an almost constant *plateau*, followed by the sharp rise and fall at the end of the particle range — the Bragg curve (figure 1.2).

2.1.2 Dose

The energy deposition in a medium by ionizing radiation is denoted by the absorbed dose — the most important physical macroscopic quantity in radiotherapy (equation 2.6) [27]:

$$D = \frac{d\bar{\epsilon}}{dm}. \tag{2.6}$$

In this equation, $d\bar{\epsilon}$ represents the *mean energy imparted by ionizing radiation to matter per unit mass* [28], dm, and is usually expressed in Gray (1 Gy = 1 J/kg).

Considering a parallel mono-energetic radiation field of fluence Φ, which is the number of particles dN traversing an infinitesimal element of area dA, the absorbed dose can be linked to the stopping power by (equation 2.7) [24]:

$$D = \frac{\Phi}{\rho}\frac{dE}{dx}. \tag{2.7}$$

> This relation only holds when there is secondary electron equilibrium. That means that the amount of energy carried into a small volume of interest by secondary electrons generated outside of the volume is on average equal to the amount of energy transported out of this volume element by secondary electrons created in the volume. [29]

2.1.3 Particle Range

Another parameter of interest concerning the physical background of protons is the range R of a charged particle. This average quantity is defined for a beam as the depth at which protons in the medium come to rest [10, 30].

As already stated in section 2.1, protons traverse matter in a nearly straight line. Hence, range is commonly expressed bearing in mind the approximate continuous energy loss of these particles, instead of multiple discrete losses [29]. This assumption that protons lose energy in a continuous matter translates into a negligible difference between the actual range R and the continuous slowing down approximation range, the CSDA-range (equation 2.8) [30]:

$$R(E) \simeq R_{CSDA}(E) = \int_E^0 \left(\frac{dE}{dx}\right)^{-1} dE, \tag{2.8}$$

in which E represents the initial kinetic energy.

Another way of calculating the range is using this variation of the, originally derived for alpha particles, Bragg-Kleeman rule (equation 2.9) [31]:

$$R(E) = \alpha E^p. \tag{2.9}$$

In the equation above, the relation between the initial beam energy, E, and the range, R, is taken into account. α and p are fitting parameters in which the former one is a material-dependent constant, and the latter one is a constant that accounts for the proton energy or velocity dependence. Both parameters can be obtained by fitting data from either measurements or theory (section 4.4.1).

From equation 2.9, and according to [32], the expression for the point value mass stopping power — another variation of equation 2.2 (section 2.1.1) — can be derived (equation 2.10):

$$\frac{S}{\rho} = -\frac{dE}{\rho dx} \approx -\frac{E^{1-p}}{\rho \alpha p}. \tag{2.10}$$

Proton range calculation is associated with uncertainties, depending on many factors (section 1.1). These uncertainties in the range measurement can be caused by, for example, lack of precision and accuracy of the measurement itself, lack of knowledge related to the energy distribution of the proton beam or the absorbing materials properties [10].

2.1.4 Energy Range Straggling

The continuous energy loss assumption for protons, considered in the previous section, is valid for many clinical calculations, representing a reliable approximation [10]. However, beam particles experience a large number of collisions with

consequent energy transfer as the slowing down process when passing through matter goes by [27]. These collisions give rise to statistical fluctuations of the energy loss, being the range spread around the mean range called energy straggling or range straggling. Consequently, protons with the same initial energy will have different stopping depths [24].

These statistical fluctuations are Gaussian distributed for thick absorbers and have a broad and asymmetric profile in the case of thin absorbers [33–35]. In the former, the straggling width, σ_R, relates to the mean range, R, via (equation 2.11):

$$\frac{\sigma_R}{R} = \frac{1}{\sqrt{M}} f\left(\frac{E}{Mc^2}\right). \tag{2.11}$$

The parameters of this equation are the mass M and the energy E of the ion projectile, and an absorber dependent slowly varying function f [36]. The $1/\sqrt{M}$ component is the explanation for the smaller straggling width of heavier ions, such as carbon ions, compared to protons.

2.1.5 Multiple Coulomb Scattering

Together with the longitudinal beam energy spread caused by range straggling, ions are also deflected laterally. This lateral scattering is caused by repeated elastic Coulomb interactions with the atomic nucleus, the so-called multiple Coulomb scattering (MCS) [24, 27]. The lighter the particle is, the more it will be deflected.

According to Paganetti, the theoretical challenge of the multiple Coulomb scattering

> (...) is (a) to predict the exact form of the MCS angular distribution and (b) to predict its characteristic width as a function of proton energy as well as scattering material and thickness. [24]

Scattering is described by the Molière analytical solution [37].

> Ignoring the small probability of large-angle single scattering ($> 10°$), the angular distribution of a large number of independent scattering events can be well approximated by a Gaussian distribution with a standard deviation. [29]

This Gaussian distribution with a standard deviation was introduced in 1975 by

Highland (equation 2.12) [38]:

$$\sigma_\theta\,[rad] = \frac{14.1MeV}{\beta pc} z \sqrt{\frac{d}{L_{rad}}} \left[1 + \frac{1}{9}\log_{10}\left(\frac{d}{L_{rad}}\right)\right]. \tag{2.12}$$

In this approximation to the Molière equation, p is the projectile momentum, d is the absorber material specific thickness and L_{rad} is the radiation length of that traversed material. The $1/\beta pc$ term shows the inverse proportionality between the multiple Coulomb scattering and the particle energy. Accordingly, heavier ions scatter less, which in some cases might result in an improved spatial resolution. However, spatial resolution does not exclusively depend on scattering.

2.1.6 Nuclear Interactions

Besides the processes already depicted, protons can also experience interactions with the atomic nucleus via non-elastic nuclear reactions. These nuclear interactions might cause fragmentation of target nuclei or even projectile nuclei, in the case of particles heavier than protons [27, 29]. The abrasion-ablation model created by Serber uses a two-step process to describe the geometrical reasons that make these collisions mostly peripheral [39]. Due to these nuclear collisions, the initial particle fluence Φ_0 decreases with increasing depth x (equation 2.13):

$$\Phi(x) = \Phi_0 e^{-N\sigma_R x}. \tag{2.13}$$

N represents the nuclear density of the medium and σ_R represents the total reaction cross section for nucleus-nucleus collisions.

2.1.7 Water Equivalent Thickness

Water is an excellent tissue-like phantom material for measurement of beam range and absorbed dose when it comes to proton therapy [40]. The reason for this is that in proton therapy it *closely mimics the properties of human tissues in terms of energy loss, MCS, and nuclear interactions* [10], due to its similar density, effective Z/A, and other properties. Thus, the beam penetration range, as well as the thickness of components in the proton beam path, are commonly described regarding the penetration depth in liquid water [32]. Accordingly, one of the quantities of interest in ion beam therapy and, therefore, in ion-based imaging, is the Water Equivalent Thickness (WET).

As previously described, the Bragg peak position depends not only on the material properties but also on the initial beam energy. To assess how far the proton beam can penetrate tissue, the shift of the measured energy deposition signal relative to a reference energy deposition signal measured in water is taken, and the ion range in a material is scaled to an equivalent range in water [32]. Hence, this WET can be

> (...) experimentally determined in a water block system by measuring the relative range shift for homogeneous materials of known thickness compared with the reference Bragg peak obtained without the material. [41]

Given a block of a specific material with thickness t_m and mass density ρ_m, the WET of that material is the thickness of water (t_w) that results in the same range (equation 2.14, figure 2.3) [32]:

$$t_w = t_m \frac{\rho_m}{\rho_w} \frac{\bar{S_m}}{\bar{S_w}}. \tag{2.14}$$

In this general equation for the WET calculation, ρ_m and ρ_w are the mass densities of the material and of water, respectively. According to [32], $\bar{S_m}$ and $\bar{S_w}$ are the mean proton mass stopping power values of the material and of water and are defined by (equation 2.15):

$$\bar{S} = \frac{\int_E S dE}{\int_E dE}. \tag{2.15}$$

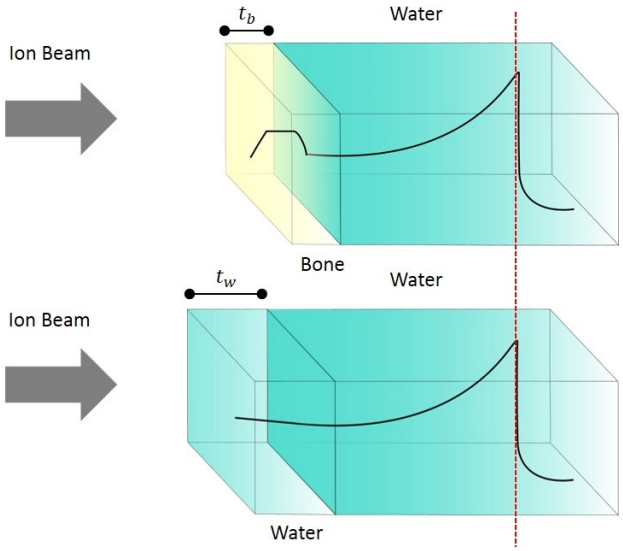

Figure 2.3: Schematic drawing of the WET concept. It represents which thickness of water (t_w) results in the same residual range as a specific thickness of a given material, in this case bone (t_b). Redrawn from [32].

Depending on whether the target is thin or thick, equation 2.14 slightly changes. A thin target corresponds to a target in which only a small fraction of the proton beam energy is lost. In contrast, a thick target corresponds to a target *in which the proton energy loss is sufficiently large* [32]. Being *sufficiently large* means that the incident proton beam is either entirely stopped inside the target or significantly degraded in terms of energy, as reported by the International Atomic Energy Agency (IAEA) [42]. These concepts depend on parameters such as the initial beam energy, the material composition, the material density, and the physical thickness [32]. In light of this, there are several approaches for obtaining the WET of different materials. In their 2009 publication, Zhang and Newhauser derived and described various approximations for the WET calculation of thin and thick targets [32].

2.1.7.1 Thin-Target Approach

The methods for calculating the WET of thin targets are based on the assumption that the energy change of a proton beam in those targets is negligible [32].

The relationship between the energy and range of proton beams in any given material can be determined using the Bragg-Kleeman rule. Substituting equation 2.10 into equation 2.14, the most relevant thin-target approximation for this work is obtained (equation 2.16) [32]:

$$t_w \approx t_m \frac{\rho_m}{\rho_w} \frac{S_m}{S_w} = t_m \frac{\alpha_w p_w}{\alpha_m p_m} E^{p_w - p_m}. \tag{2.16}$$

As before, α is a material-dependent constant, E is the initial energy of the proton beam and p is an energy-dependent fitting parameter.

2.1.7.2 Thick-Target Approach

When it comes to thick targets, the energy changes cannot be neglected and, the mean mass stopping powers in equation 2.14 must be calculated [32].

IAEA proposes the following thick-target approximation (equation 2.17) [43]:

$$t_w = t_m \frac{\rho_m}{\rho_w} c_m, \tag{2.17}$$

in which c_m represents the depth scaling factor. This parameter can be approximately calculated as the ratio of the CSDA-range in water, R_w, to that in the target

material, R_m (equation 2.18):

$$c_m = \frac{\rho_w R_w}{\rho_m R_m}. \tag{2.18}$$

Finally, equation 2.17 can be rewritten as

$$t_w \approx t_m \frac{R_w}{R_m}. \tag{2.19}$$

In ion radiography, the measured quantity is the residual energy behind the irradiated object being studied. The difference between the initial beam energy and the residual energy corresponds to the integrated energy loss of particles when traversing that object. According to Telsemeyer *et al.* the integration of the stopping power ratio (SPR) over the thickness equals to the WET of an object with dimension L (equation 2.20) [44]. In this case, the SPR corresponds to the ratio between the mean stopping power of the target material, $\overline{SP}_m$, and the mean stopping power of water, $\overline{SP}_w$. Therefore,

$$WET = \int_0^L \frac{\overline{SP}_m}{\overline{SP}_w} dl. \tag{2.20}$$

Moreover, and as also stated in that publication, the Water Equivalent Path Length (WEPL), important for assessing the trajectory of protons, can be obtained by (equation 2.21) [44]:

$$WEPL = \frac{\overline{SP}_m}{\overline{SP}_w}. \tag{2.21}$$

2.2 Radiation Detectors

One of the requirements for performing imaging in proton therapy is choosing an appropriate detector, according to the necessary characteristics for the desired researches, tests and studies. The inherent specifications of a detector will influence the outcoming results so they should be a compromise between suitability, efficiency, usability, and cost.

Radiation detectors can be used on solid, liquid or gaseous media and they give information concerning the presence of ionizing particles. This information can be translated into energy, charge, type, momentum or even spin of a specific ion.

Commonly, the principle behind the detection relies on the creation of free charge carriers or carrier pairs due to processes such as photo-absorption, Compton scattering or pair production, by ionizing particles or γ rays. These created free charge

carriers can then be collected, amplified and converted into measurable signals.

2.2.1 Semiconductor Detectors

The principle behind semiconductor detectors is the creation of free charge carriers by ionizing radiation. When in the presence of an electric field, these free charge carriers drift to the opposite electrodes, generating a signal. This signal will be proportional to the energy deposition inside the detector.

Within semiconductor detectors, there are germanium detectors and silicon detectors. The latter ones can be composed by a series of narrow parallel strip electrodes or by small individual electrodes, small pixels.

The pixelated silicon detector chosen for the performed tests in the present dissertation will be presented in section 4.3.1.

2.3 Proton Radiography

In the matter of therapy, it is required that protons stop at the proximity of the tumor, in order to deposit their maximum energy and thus irradiate the diseased tissue. Contrarily, proton transmission imaging requires the passage of protons through the patient allowing them to reach a detector [45]. In other words, this means that the range in tissue of the energies needs to be larger than the object being studied. As a consequence, the energy needed for imaging is higher than the one needed for treatment.

The mechanisms for achieving image contrast are the ones described in the preceding sections (sections 2.1.1 to 2.1.6), mainly the energy loss of each proton. As already stated before, when a proton interacts with matter it loses its energy. This energy loss equals to the difference between the initial beam energy and the residual energy that reaches the detector. Therefore, if the energy that reaches the detector is small, the energy loss will be close to the initial beam energy, resulting in better contrast.

3

State of the Art

Throughout the previous sections, the physical background of proton therapy, proton radiography as well as the motivation of this work were introduced. As already pointed out before, relatively new techniques like these always go through an extensive testing process (section 1.1), and this is one of the main reasons why they have not reached clinics so far. This chapter will present some of the already existing studies related to these topics, mainly proton radiography.

3.1 Imaging with Protons

When compared to X-ray imaging techniques, imaging with protons offers a better density resolution — at the cost of a decreased spatial resolution — with a remarkably reduced dose to the surrounding healthy tissue [17]. Nonetheless, the high cost associated with the production of proton beams or, on the other hand, the drawbacks caused by the multiple scattering of the particles in terms of image quality, are two of the factors that contribute for the lack of suitable proton radiography (pRG) and proton tomography (pCT) imaging systems [45].

3.1.1 Historical Analysis

The first planar proton radiography was published by Koehler, in 1968 (figure 3.1). His work showed that high contrast proton radiographies could be obtained by using films as detectors [46]. As cited in the Abstract of his publication in Science,

> Energetic protons from an accelerator may be used to produce radiographs showing unusually high contrast but relatively poor spatial resolution. [46]

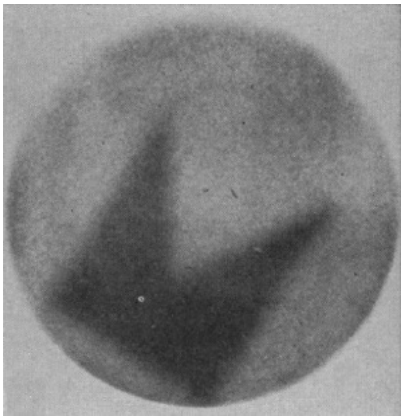

Figure 3.1: First published proton radiography [46].

Together with Steward, the interest of Koehler in pRG continued and in 1972 the technique was proposed as a diagnostic tool at the AAPM Winter Meeting [47]. During that decade, this duo of researchers exploited the use of proton imaging applications in terms of tumors and stroke detection [48, 49], breast carcinoma diagnosis [50] and brain tumor imaging [51].

The evolution of pRG moved along with the development of pCT. In this regard, Cormack and, once again, Koehler, published the first pCT reconstruction, in 1976. Using NaI scintillators coupled to photomultiplier tubes, the WEPL values of a circularly symmetrical phantom were obtained, and *density differences of 0.5% were reconstructed with reasonable accuracy from data obtained with very simple equipment* [52].

At the Los Alamos Laboratory, Hanson was one of the most significant contributors regarding pCT. All his work translated into a *huge step forward, both conceptually and experimentally* [45], concerning imaging with protons. In his 1981 publication, a hyperpure germanium calorimetric detector was used as a residual energy-range detector (RERD), and a multiwire proportional chamber was used as a position-sensitive detector (PSD). The carried out studies showed that scoring the energy loss of individual protons can yield good spatial resolution [53]. Moreover, proton stopping power was assessed relying on a stack of plastic scintillators working as range telescopes, concluding that

> Since the proton method reconstructs the stopping power relative to some reference medium rather than the linear attenuation coefficient for X-rays, proton CT scans provide imaging characteristics different from X-ray scans. It is possible that this alternative imaging modality may provide diagnostic benefits when applied to clinical studies. [53]

Back in 1979 Hanson also stated that

> At first sight, the data handling problems associated with a 10 MHz data rate appear formidable. However, upon closer inspection, these problems are found to be soluble with present-day technology with only a modest amount of multiplexing and parallel processing. [54]

Almost four decades later, achieving a 10 MHz proton detector system is still a struggle for developers [45].

With the increase in the availability of more appropriate accelerators and gantries, the first hospital-based proton beam treatment center was inaugurated in the mid-1990s at the Loma Linda University Medical Center (LLUMC), California [55].

Towards the end of the millennium, other relevant works related to this topic were published. In 1995, Schneider and Pedroni proposed pRG as *a tool for quality control in proton therapy* [56] and in 2000, Zygmanski *et al.* stated that the

> Comparison of the reconstructed proton CT values with X-ray CT derived proton stopping powers shows that there may be some advantage to obtaining stopping powers directly with proton CT. [57]

To accomplish that, he and his contributors implemented an energy modulated cone-beam pCT

> (...) produced by scattering a 160 MeV proton beam with a modifier that results in a signal in the detector system, which decreases monotonically with depth in the medium. [57]

3.1.2 The Contemporary Era

In the present state of imaging with protons, two concepts exist: single proton-tracking and integrating systems [45]. In the following sections, a summary of some of the existing studies will be presented.

3.1.2.1 Tracking Systems

Single proton-tracking systems, both radiography and tomography, consist of a number of PSD modules to assess proton trajectory and RERDs to calculate its residual energy [45].

In 1999, a proton-tracking system consisting of two PSDs — one before and one after the patient — was described by Pemler *et al.*. Scintillating fiber hodoscopes (Sci-Fis) were the selected tracking units and the used RERD was a range telescope. The used phantoms were a 20 mm-thick Plexiglas plate with 10 mm deep and 5 mm in width engraved letters, and a Plexiglas plate with cylindrical holes with different widths and depths. To carry out the irradiation, a 177 MeV proton beam was used. Concerning the results, a spatial resolution of approximately 1 mm and a density resolution of 0.3% for 200 protons/mm^2 were obtained [58]. Later on, using that exact system, Schneider published a study showing

> (...) the feasibility of proton radiography in terms of radiation dose, imaging speed, image quality (density and spatial resolution), and image content under clinical conditions. [59]

Using a 214 MeV proton beam, radiographic images of a canine subject were obtained with a spatial resolution of approximately 1 mm, a range sensitivity of the images of around 0.6 mm and a dose exposure of merely 0.03 mGy (figure 3.2) [59].

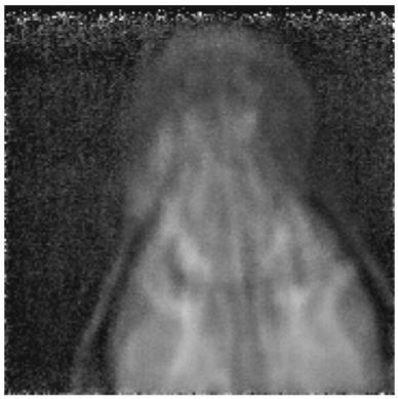

Figure 3.2: Proton radiography of a canine head [59].

The Advanced Quality Assurance in Hadron Therapy project, funded by the National Center for Oncological Hadron Therapy (CNAO) (Pavia, Italy), aimed at proton range radiography. The tracking system, similarly to the work published by Pemler, consisted of two PSDs downstream of the patient. Thus, only exiting proton direction and position were assessed. The tracking units technology was based on gas electron multipliers (GEMs) and the RERD was a stack of plastic scintillators. Using a proton beam energy of 100 MeV, a 20 mm-thick Plexiglas plate was successfully irradiated with a spatial resolution inferior to 1 mm and a density resolution of a few percents [60, 61]. There are many other ongoing investigations concerning this field. All of them rely on different combinations of PSD and RERD technologies [62–67].

3.1.2.2 Integrating Systems

Contrarily to single proton-tracking systems, proton-integrating technology relies on the passage of a number of incident protons to generate the signal [45]. That generated signal relates to the fluence and energy distribution of the protons. Average proton WEPL/WET through the patient is one of the assumed calibration hypothesis for the signal of proton-integrating radiography. One of the drawbacks of the proton-integrating approach is the *halo* effect at material interfaces owed to *the interplay of multiple Coulomb scattering and energy loss* [45].

Studies like the one carried out by Telsemeyer *et al.* in 2012 support the usefulness of amorphous silicon flat-panel detectors for image guidance in carbon ion therapy [44]. In that publication, using a filtered back projection approach for the reconstruction, accuracy better than 0.5 mm WET, and a high spatial resolution given by the pixel size of the detector (0.8×0.8 mm^2) were obtained. Another feature of this carbon ion study that can be highlighted is the so-called energy scanning used for the range measurement. With this technique, the object is irradiated several times with *a number of rectangular monoenergetic fields with different carbon ion beam energies* [44]. This allows the correlation of the measured signal with the initial beam energy and, consequently, the WET of the traversed object can be determined. Later on, the WEPL values can also be assessed (figure 3.3).

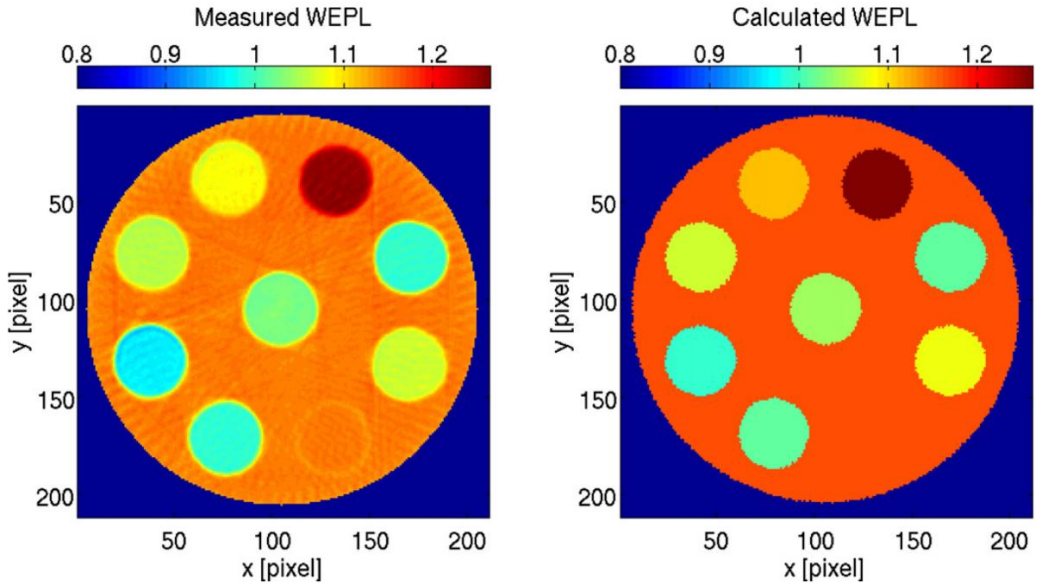

Figure 3.3: Carbon ion tomography. Comparison between the reconstructed WEPL image of the phantom (left) and the expected WEPL image calculated from the known material and geometry [44].

In 2013, Testa *et al.* used a prototype two-dimensional diode-array detector to study pRG and pCT based on time-resolved dose measurements or, in other words, *the time dependence of the dose distribution delivered by a proton beam* [68]. The accuracy of the determined relative stopping power values was negatively influenced by the limited spatial resolution [68]. Several phantoms with varying complexity were used, and figure 3.4 shows the results of one of them, a hollow plastic ball filled with water and with a diameter of 7 cm.

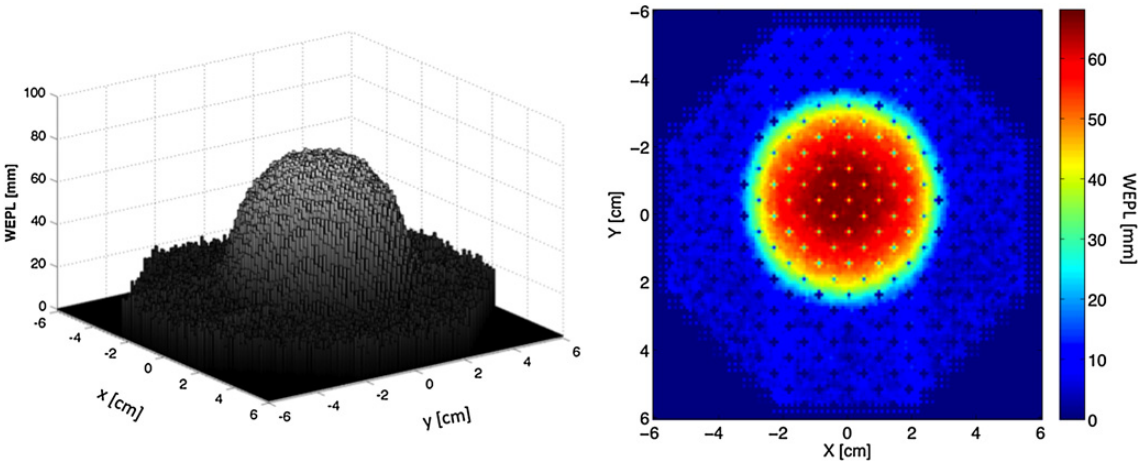

Figure 3.4: Proton radiography of a plastic ball filled with water plotted (a) as a 3D histogram and (b) as a planar image [68].

Using complementary metal oxide semiconductor active pixel sensors (CMOS APSs), Seco and Poludniowski *et al.* obtained proton-integrating projection radiographs of phantoms, therefore demonstrating the potential of such an approach [69, 70]. In the former one, a monochromatic energy beam with 117 MeV was used to irradiate two different setups:

> a pen with two metal screws in order to assess the spatial resolution of the system and a phantom with lung tissue, bone tissue, and solid water in order to assess the density resolution (tissue contrasts) of the CMOS sensor. [69]

In the latter one, a *contrast-detail phantom manufactured from an 8 mm-thick sheet of PMMA, with a number of holes of varying size and depth* [70], was the chosen phantom. In terms of energies, a 36 MeV cyclotron beam and a 200 MeV clinical radiotherapy beam were used.

Similarly to the presented studies, this thesis will propose a proton-integrating system for proton radiography. The required components and their characteristics will be further explained in the next chapter.

4

Materials and Methods

As already presented in section 1.2, this work aims to develop a reliable setup for small-animal proton radiography. To this purpose, a Monte Carlo feasibility study was performed. After a brief overview of the imaging setup (section 4.1), the FLUKA Monte Carlo code and the simulation geometry are presented in sections 4.2 and 4.3, respectively. The development of a method for Water Equivalent Thickness (WET) reconstruction and the creation of evaluation metrics for performance assessment are presented in sections 4.4 and 4.5. Finally, a method to estimate the time required for obtaining radiographic images with the proposed setup is shown in section 4.6.

4.1 Overview

The present thesis was a preparatory simulation work related to the the Small Animal Proton Irradiator for Research in Molecular Image-guided Radiation-Oncology (SIRMIO) project, funded by the European Research Council. Dealing with small animals requires a lower energy range than what is used for the treatment of human size patients. Nonetheless, for transmission imaging, the proton range in tissue needs to be larger than the thickness of the object. This means that the energy required for imaging small animals is higher than the energy required for treatment (section 2.3). Hence, assuming a mouse mostly composed of water, the ideal energy range for imaging is 40 to 90 MeV.

One of the most important notions to bear in mind is that the studied approach does not rely on single particle tracking. In such cases, thin tracking detectors measure the particle trajectories both entering and exiting the phantom, in order to estimate the most likely path (MLP) of individual particles through the phantom. Consequently, multiple scattering is explicitly taken into account. For this project, scattering is not taken into account, and there is no information about the

trajectories of individual particles.

The imaging of the studied object is based on energy modulation using single shots, also known as energy stacking or energy scanning. With this technique, similarly to what was done by Telsemeyer *et al.* [44], the object is irradiated multiple times with different kinetic energies. In this work, each study consists of several simulations in which the beam position and initial beam energy are varied. This means that for each simulation the object will be irradiated with a different proton beam energy. Then, using a pixelated detector the signal of many protons is integrated, allowing its correlation with the initial beam energy and the estimation of the range values.

4.1.1 Simulation Setup

The used setup for the FLUKA Monte Carlo simulations carried out throughout this thesis consisted of a proton beam irradiating a phantom located upstream of a detector (figure 4.1). All these components will be further explained in the subsequent sections.

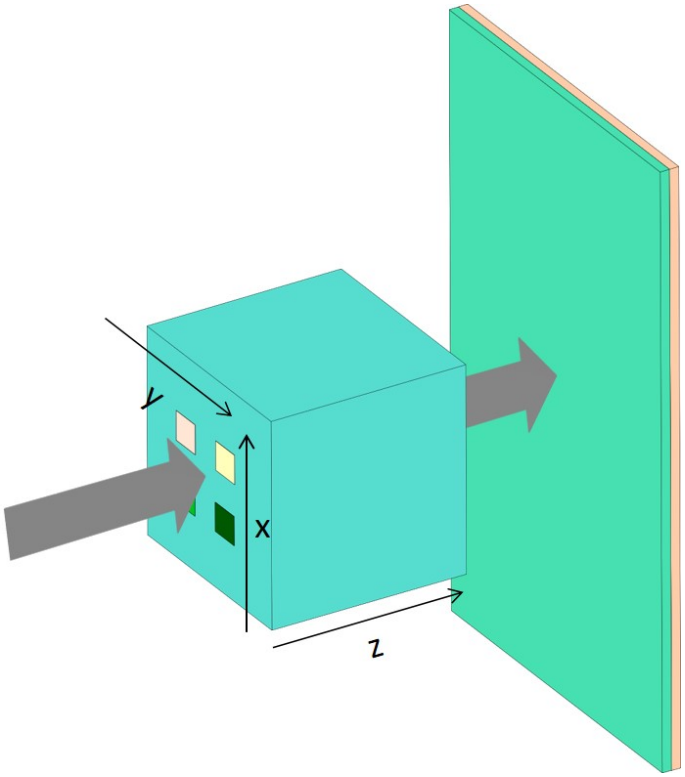

Figure 4.1: Schematic representation of the irradiation setup used for the FLUKA Monte Carlo simulations. The beam (gray) goes through the object (center) and reaches the detector (on the right). The considered coordinates system is also represented.

As already explained in the previous chapters, a proton beam penetrating an object loses energy depending on the initial proton energy and on the material properties of the object. For the same material, the energy loss inside a thin detector located behind the object hence depends on the initial beam energy, as shown schematically in figure 4.2.

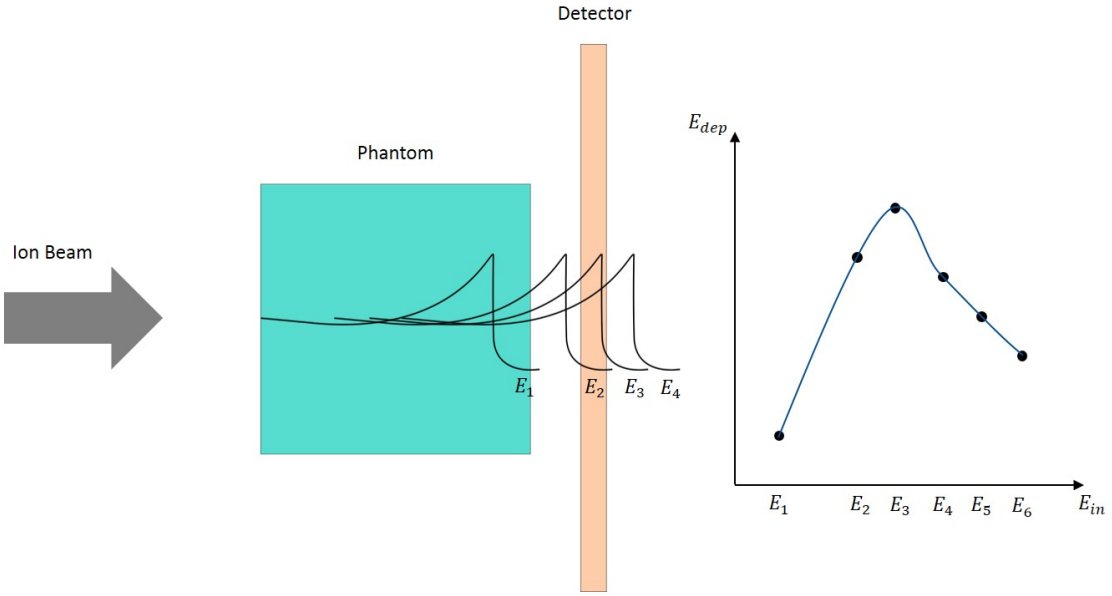

Figure 4.2: Irradiation scheme and corresponding energy deposition (in the detector) vs. initial beam energy graph. This scheme depicts the influence of irradiating an object with different energies.

Analyzing the scheme presented in figure 4.2, what happens in the case of this simulation setup is that each irradiation with a different initial proton beam energy (E_{in}) will yield a different Bragg curve (left, on the phantom) with a corresponding energy deposition inside the detector (E_{dep}). All the obtained points will resemble an *inverted Bragg curve* profile (right, on the graph). Therefore, the information used for imaging is the energy deposition scored within the detector.

The parameters adjusted within the Monte Carlo simulations are:

- The phantom-detector distance;
- The range of initial beam energies;
- The width and spacing of the beams;
- The number of primaries, i.e., the number of protons;
- The beam shape.

4.2 FLUKA Monte Carlo Simulations

Monte Carlo methods comport a broad class of computational algorithms relying on repeated random sampling to extract a given configuration taking into account a probability density function. These probability distributions allow the sampling of certain events to replicate complex physical processes, according to their underlying phenomena [41]. In terms of proton therapy, these methods can be used to calculate the propagation of the beams as they interact with the traversed matter.

A commonly used Monte Carlo code in proton and ion beam therapy applications is FLUKA (Fluktuierende Kaskade). FLUKA is a fully integrated multipurpose tool for the calculation of particle transport and interactions with matter [71, 72].

The range of applications of FLUKA is wide. From proton and electron accelerator shielding to target design, neutrino and cosmic ray physics, calorimetry, amongst many others [72]. It provides high accuracy simulations of interaction and propagation in matter of about 60 different particles from photons and electrons with energies ranging from 1 keV to thousands of TeV to hadrons of energies up to 20 TeV and neutrons down to thermal energies [72]. Additionally, it includes an improved version of the Combinatorial Geometry (CG) package, making it able to handle very complex geometries [72].

There are several examples in the literature that exploit the usefulness of this tool. In 2006, Sommerer *et al.* exhibited in their publication that *proper adjustment of the ionization potential given in input to the program* [73] provides sub-millimeter agreement for the ion range in water, showing also *good agreement with available experimental depth dose distributions* [73]. Later on, Parodi *et al.* presented an adaptation of the FLUKA Monte Carlo code for *calculation of delivered dose and irradiation-induced positron emitter distributions for clinical cases treated with proton beams* [74]. The utility of algorithms using the Monte Carlo technique for treatment planning was demonstrated by Böhlen *et al.* with a MC-based treatment-planning (MCTP) tool for ion beam therapy [75]. In their 2014 publication, Bauer *et al.* stated that validation and support of ion therapy treatment planning could be done making use of Monte Carlo calculations. This powerful tool can even lead to the introduction of *new treatment techniques, indications and ion species in the clinical practice* [76].

4.2.1 Input File

In order to start a FLUKA simulation, an input file has to be created. This input file is a standard ASCII file containing a variable number of *commands*, or *options*, each consisting of one or more *lines*, the so-called *cards*. Each card contains one keyword, six floating point values (*WHATs*) and one character string (*SDUM*) [72].

There are optional and mandatory commands within the input file. In light of this, the user has to specify the particle type and energy, as well as the source position (BEAM and BEAMPOS cards). Furthermore, the description of the setup geometry (GEOBEGIN, SPH, REGION, ..., GEOEND cards), the definition of the materials, including their composition and properties (MATERIAL, COMPOUND and MAT-PROP cards), and their assignment to specific regions of the object (ASSIGNMA card) have to be defined. As an option, the user can add several detectors to the input file to score for example dose, fluence or energy on a user-defined scoring grid, using, for instance, the USRBIN card. Problem settings like physical effects and production or transport thresholds can be established and altered (PHYSICS, DELTARAY, ... cards) and the starting signal and the number of requested histories, or *primaries*, has to be given [29, 72]. The definition of each one of these cards relates to the problem that will be simulated. For the present work, the default HADROTHE card was used. This card provides default configurations for particle beam applications and enables the transport of low-energy neutrons, electrons, photons, and ions. It provides identical thresholds for particle transport and delta ray production and regarding multiple scattering the threshold is at *minimum allowed energy, for both primary and secondary charged particles* [72].

A graphical user interface called FLUKA Advanced Interface (FLAIR), which is based on Python and Tkinter, is available [77]. This interface displays the input file in an easily readable way, offers several plotting utilities, includes a predefined material database, allows monitoring the status of each simulation run, compiling and starting FLUKA jobs from a Graphical User Interface (GUI) environment [29].

Within this thesis, FLUKA version 2011.2x-2 and FLAIR version 2.3-0 were used.

4.2.2 User Routines

Generally, it is possible to run FLUKA simulations without the need to write a single line of code, while the required input is only taken from a single ASCII file [72]. However, for some complex cases, the offered standard options are not sufficient. In

these situations, the user can define non-standard input and output or even alter the normal particle transport up to a certain extent [72]. This is accomplished by using the so-called *user routines*, available as template routines in the FLUKA library. These Fortran 77 routines can be modified and adapted by the user according to the problem being studied. Their activation requires a special command in the FLUKA input file as well as compilation and linking to the FLUKA library [29, 72].

The list of accessible user routines is ample but within this work, only the *source.f* routine was used. When the standard BEAM, BEAMPOS, and BEAMAXES cards hinder the description of distributions in, for example, space, energy and time, sampling of the primary particle properties is carried on by the *source.f* user routine. The necessary values can be assigned, generated by a chosen sampling algorithm or read from a file [72].

Based on previous work [29, 78], new source routines were developed:

- A rectangular-shaped source, described by a one-dimensional Gaussian on one axis with a specific full width at half maximum (FWHM) (figure 4.3 (a));
- A pencil-shaped source, described by a two-dimensional Gaussian with two independent FWHMs (figure 4.3 (b)) [29].

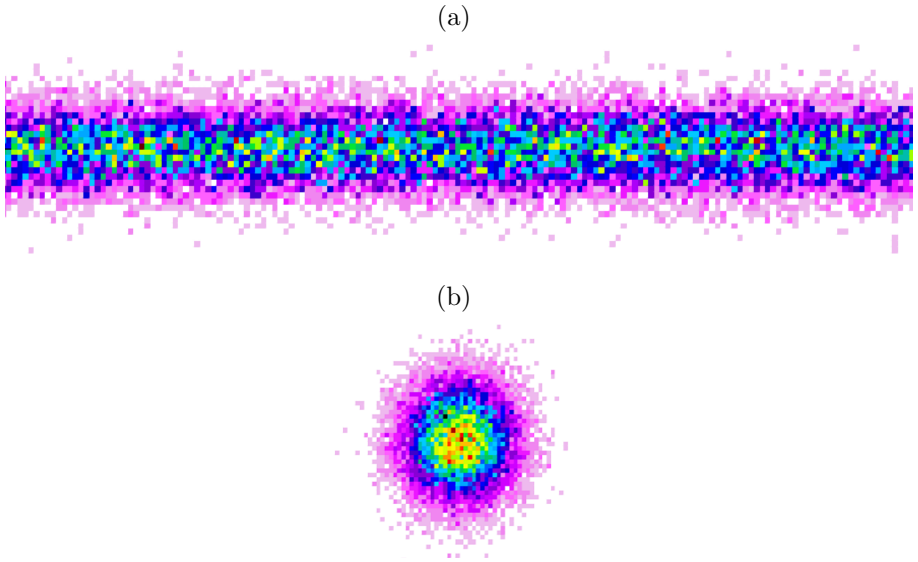

Figure 4.3: Example of (a) a rectangular-shaped source and (b) a pencil-shaped source.

4.2.3 Automatic Input File Update

A Python script was created to automatically adjust the BEAM, SOURCE, GEOMETRY and USRBIN cards in the FLUKA input file. Within this script, the user has the option of changing the parameters mentioned in section 4.1.1. Therefore, it is possible to modify features of the beam such as initial energy, shape, width, spacing between subsequent beams, x and y coordinates, scanning area, or even the total number of protons, and features of the geometry such as the positions of the phantom, of the detector and of the USRBINs.

Once the user defines all the desired parameters and runs the script, a dummy input file will be opened. From this dummy input file, each line will be read, and the commands corresponding to the adjusted parameters will be updated. A new input file will then be saved for each combination of new parameters. Each one of those newly created input files will correspond to a different simulation and are moved into a different run directory. Due to the typically high computation time required for running MC simulations, the user has the option of submitting these simulations to a high performance computing cluster and thus run several jobs or simulations in parallel.

Another available option included in this Python script is the automatic processing of the simulation output (USRBINs). Each input file contains three types of USRBINs:

- DOSE;
- ENERGY;
- PROTON.

The DOSE USRBINs score the total dose delivered to the phantom inside a user-defined area, which can either be a pixel, a slice or the entire volume. The ENERGY and PROTON USRBINs score the energy deposition and the proton fluence inside the active layer of the detector, respectively. The merged USRBINs will then be used for the image reconstruction (section 4.4) and the calculation of the dose deposition inside the phantom. For the latter, the total dose required for imaging will be the sum of dose scored for each beam and for each energy.

4.3 Simulation Geometry

Throughout this section, the selected detector (section 4.3.1), the selected phantom (section 4.3.2), the selected proton beams (section 4.3.3) and the standard simulation parameters (section 4.3.4) will be presented. In terms of the detector and of the phantom, the subsequent sections will go through their geometry, properties and specifications.

4.3.1 Detector

The chosen detector for performing the FLUKA Monte Carlo simulations, explained in section 4.2, is a simplified version of the commercially available RadEye™1 detector.

4.3.1.1 RadEye™1

The RadEye™1 detector is a commercially available large-area image sensor (figure 4.4). This three-side buttable, fully integrated and two-dimensional CMOS photodiode array was designed for both visible and high-energy radiation imaging of photons [79]. Its structure and the fact of being buttable on three sides makes it possible to achieve larger image formats by tiling together multiple sensors. It can be used directly as a visible light detector or with a scintillator directly coupled to detect X-rays [80].

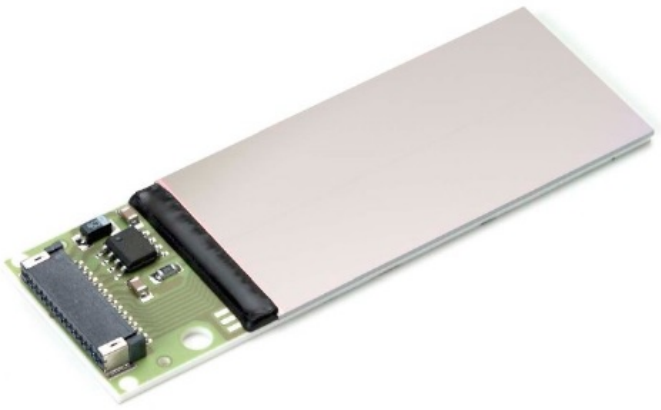

Figure 4.4: RadEye™1 CMOS image sensor [79].

The active silicon area, a photodiode matrix of 512 by 1024 pixels with a spacing of 48 μm, covers 24.6 $\times$ 49.2 mm^2 [80] and a depletion depth of about 2 μm is inherent

to this device. [81]. Moreover, all the operational signals are granted by a small connector placed at a short sensor side, and a pixel fill factor of about 80% arises from the integrated on-chip control circuitry [81]. The sensor can be operated with a maximum frame rate of 4.5 frames per second [80]. A further advantage of this detector is its high dynamic range with a saturation level at a proton fluence around 4.4×10^7 protons/cm^2 [81].

A simplified version of RadEye™1 was modeled in the simulation geometry, consisting of only two layers: the passivation layer and the active layer (figure 4.5, left). The former one is made of silicon oxide (SiO_2) (figure 4.5, center) and has the same thickness (2 μm) as the latter one, a monolithic block of silicon (figure 4.5, right) where the energy deposition in each pixel is scored using an ENERGY USRBIN (section 4.2.3).

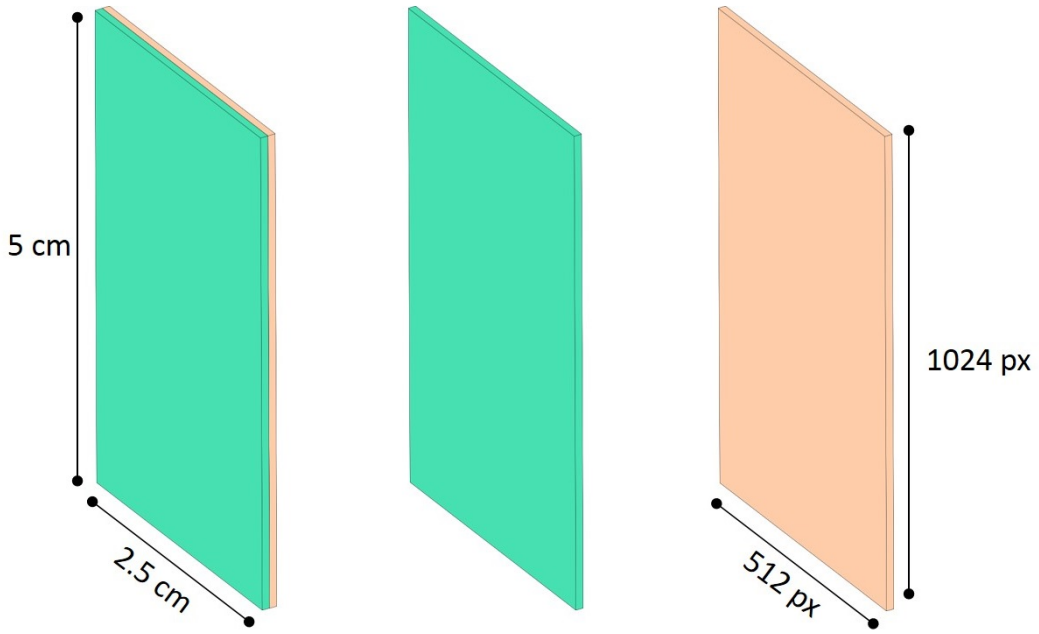

Figure 4.5: FLUKA geometry of the simplified detector model consisting of a silicon oxide passivation layer (center) and of a silicon active layer (right).

Each one of these layers has a height of 1024 pixels and a width of 512 pixels, and each one of those pixels has 48×48 μm^2. This means that the data matrix will have x and y dimensions of 1024 and 512, correspondingly. Moreover, due to the energy stacking principle, the third dimension of the final data matrix will have as many layers as the number of used proton beam energies. To reduce the amount of generated data and computation time, 2×2 adjacent pixels were combined before further analysis. The size of one combined pixel is hence 96×96 μm^2 and thus still sufficiently small for the aimed sub-millimeter spatial resolution.

4.3.2 Phantom

The object to be imaged within this study was a $2 \times 2 \times 2$ cm^3 water block in which tissue and plastic materials were inserted: adipose tissue, compact bone, poly(methyl methacrylate) (PMMA, or Plexiglas), a standard quality assurance material in radiation therapy, and striated muscle (figure 4.6).

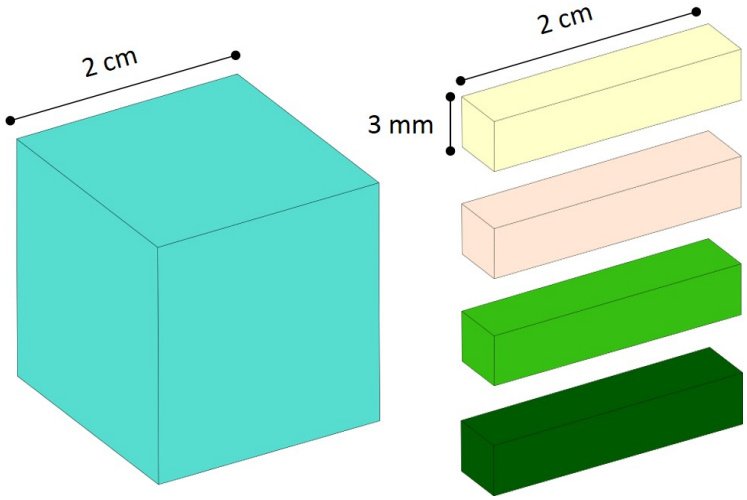

Figure 4.6: Geometry of the water block (left) and of the inserts (right). The inserted materials were (from top to bottom, on the right): compact bone, adipose tissue, PMMA and striated muscle.

The four materials were inserted symmetrically inside the water block, going through the entire thickness of it (figure 4.7). Every insert has the same dimensions: a height of 3 mm, a width of 3 mm and a thickness of 2 cm. Different two-dimensional views of the object are presented in figure 4.8. Table 4.1 summarizes the properties of the phantom materials.

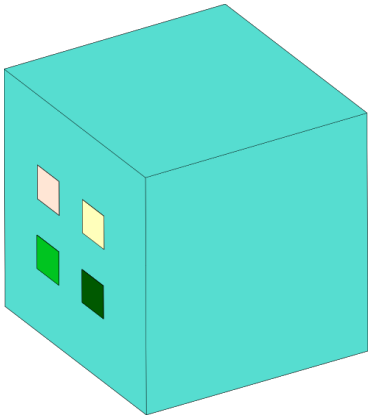

Figure 4.7: FLUKA geometry of the phantom.

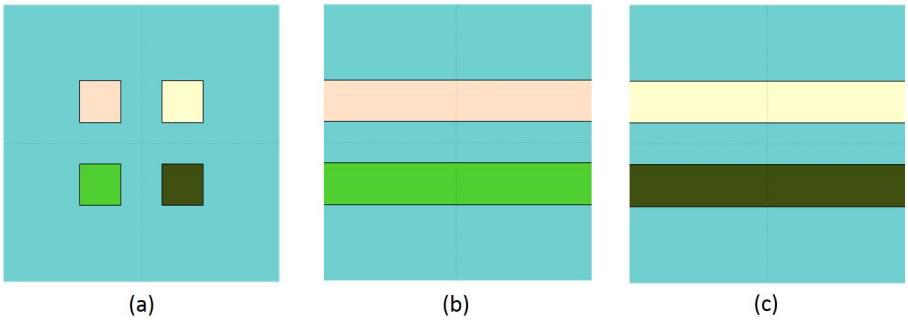

Figure 4.8: Two-dimensional views of the object. (a) Front view, (b) vertical slice view of the adipose tissue and PMMA inserts and (c) vertical slice view of the compact bone and striated muscle inserts.

Table 4.1: Phantom properties.

Material	Density (g/cm^3)	WET (cm)
Water	1.00	2.00
Adipose tissue	0.92	1.89
Compact bone	1.85	3.43
PMMA	1.19	2.31
Striated muscle	1.04	2.06

A 2D distribution of the true WET values of the object of interest was created (figure 4.9). The true WET values of each material, present in table 4.1, were obtained following a similar approach to the one described in figure 2.3 (section 2.1.7). Therefore, five FLUKA Monte Carlo simulations of a water block were carried out. The first one consisted in simply irradiating a water block target with a proton beam of 70 MeV. In the subsequent four simulations, the four insert materials were added upstream of the water block. From here, all the corresponding Bragg curves were extracted and a 4^{th} order polynomial function was fitted to the peak region in water. The shift of the Bragg peak (BP) position relative to water is then the WET (equation 4.1):

$$WET = BP^{position}_{vacuum} - BP^{position}_{material}. \tag{4.1}$$

The true WET values obtained for adipose tissue, compact bone, PMMA and striated muscle were 1.89, 3.43, 2.31 and 2.06 cm, respectively.

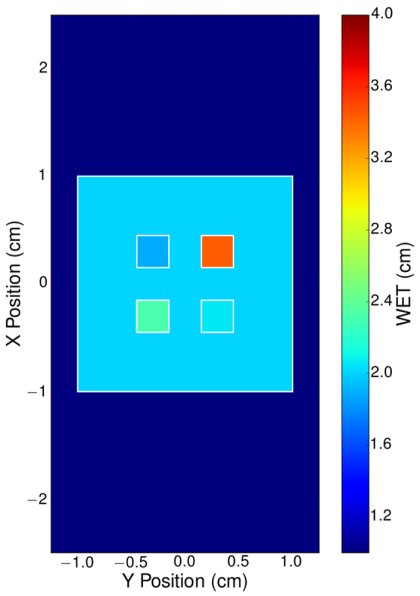

Figure 4.9: True WET image. From left to right, top to bottom the inserts are: adipose tissue, compact bone, PMMA and striated muscle.

4.3.3 Proton Beams

The two source routines described in section 4.2.2 provide two proton beam shapes: the fan beam and the spot scanning approach.

The fan beam approach relies on the rectangular-shaped source, having a Gaussian profile on the scanning dimension. The orientation of the beam can be either horizontal (moving along the x dimension) or vertical (moving along the y dimension), and simulations of both orientations can be combined. To accomplish this merging of information, the mean of both the horizontal and the vertical data array was taken:

$$d_{merged} = \frac{d_x + d_y}{2}, \tag{4.2}$$

in which d_x and d_y correspond to the data arrays of the x fan beam and the y fan beam, respectively. These data arrays contain the energy deposition values of each pixel within the active layer of the detector.

The width and spacing of the different beams, as well as their scanning area, are user-defined. The position of the beams can be adjusted such that the entire phantom is scanned. Within the performed tests in this thesis, the chosen spacing, and FWHM was 1 mm, resulting in a total of 21 fan beams (for each orientation) used for each one of the initial beam energies and covering the 2×2 cm^2 large phantom.

The spot scanning approach relies on the pencil shaped source, consisting of several

round pencil beams with a Gaussian profile in both dimensions. Once again, the entire object is scanned according to the user-defined width, spacing of the different beams and scanning area. For the carried out tests, the chosen spacing between two adjacent pencil beams was 1 mm, which was also their FWHM in the x and y dimensions, resulting in a total of 441 pencil beams used for each initial beam energy and covering once more the entire 2×2 cm^2 large phantom.

Additionally, a third type of proton beam can be used: the so-called broad field approach. As this approach consists of a homogeneous square beam (2×2 cm^2) covering the entire object, no dedicated source routine had to be created, the standard FLUKA commands were sufficient.

4.3.4 Standard Simulation Parameters

The standard parameters established for the majority of the simulations are given in table 4.2. The energy range was chosen according to the explanation given in section 4.1, and the beam width is related to design specifications of the SIRMIO project and the aimed sub-millimeter spatial resolution.

Table 4.2: Standard parameters of the FLUKA Monte Carlo simulations.

Phantom-detector distance	1.5 cm
Energy range	45 – 75 MeV
Energy step	0.5 MeV
Beam shape	Fan beam
Beam width and spacing	1 mm
Number of primaries	100 000

For the tests presented in this thesis, the only changed parameters were the phantom-detector distance, the number of primaries and the beam modality. The different tested phantom-detector distances were: 1.5, 2.0, 2.5 and 3.0 cm. With this test, the goal was to assess to which extent bigger air gaps influence scattering and thus the overall spatial resolution of the images. Regarding the number of primaries, the tested quantities were 2×10^5, 10^5 and 4×10^4 primaries per energy per beam. This parameter is directly related to the total dose given to the object, hence changing it would allow establishing a dose-image quality dependence. Finally, the different beam shapes tested were the fan beam, the spot scanning, and the broad field approaches, already explained in the previous section.

4.4 Image Reconstruction

The information used for imaging is the energy deposition scored within the detector pixels for each initial proton energy and beam position individually. Only the pixels within the central beam position ± half of the spacing between two adjacent beams are taken into account. Therefore, protons with larger deviations from approximately straight paths are not considered for the reconstruction. Thus, a two-dimensional energy deposition map is created for each initial beam energy by combining the information extracted from the individual beams. For each detector pixel there is an energy deposition vs. initial beam energy profile (section 4.1.1, figure 4.2).

Within this thesis, two methods were explored to reconstruct the WET distribution from the energy deposition maps: the peak finding (PF) and the signal decomposition (SD) method.

4.4.1 Peak Finding

For this method, a Python script was created. This script is capable of reading all the output data of the simulations and extracting the peak values from the energy deposition vs. initial beam energy profiles. Based on *scipy.signal.argrelextrema* the relative extrema of data are calculated and a *tuple of ndarrays* containing the indexes of the maxima in arrays of integers is returned, which means the peaks in the noisy data are identified, and an array containing their indexes is returned (figure 4.10).

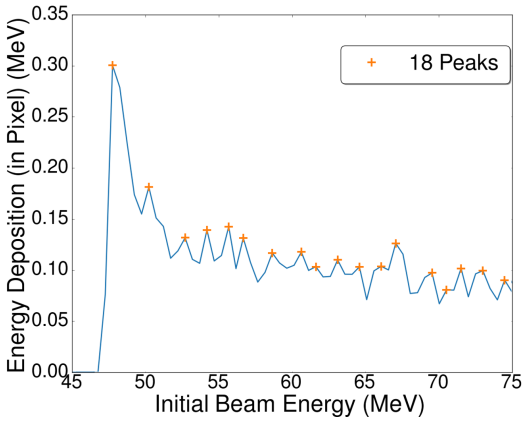

Figure 4.10: Example of an energy deposition vs. initial beam energy profile obtained with the peak finding technique. The orange markers correspond to the peaks found by the *scipy.signal.argrelextrema* function.

From the energy deposition vs. initial beam energy profiles obtained for each individual pixel, the beam energy of the first peak is extracted (figure 4.11, red dashed line) and plugged into equation 2.9 to obtain the corresponding WET values. Therefore, there is a parametrization of the peak position, the energy deposition in the detector, as a function of the initial beam energy. Figure 4.11 is a simplified representation of figure 4.10.

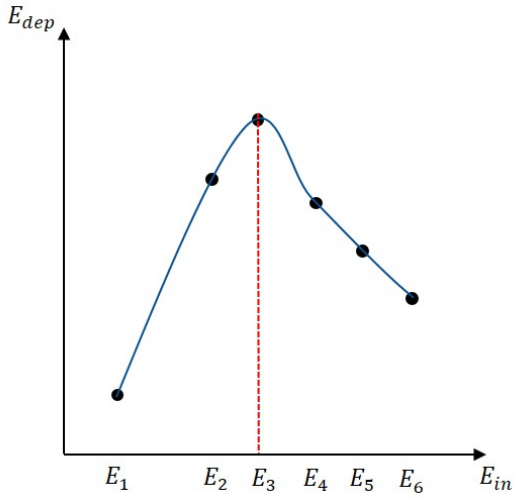

Figure 4.11: Representation of the energy deposition in the detector vs. initial beam energy. This graph corresponds to the outcome of irradiating the object with different energies. Redrawn from figure 4.2.

In equation 2.9, the range $R(E)$ corresponds to the calculated WET value and E corresponds to the initial beam energy extracted from the *inverse Bragg curve* profiles, introduced in section 4.1.1 (figures 4.2, 4.10 and 4.11). Once the α and p fitting parameters are estimated, the equation can be applied to the entire phantom area, to obtain the respective WET values, and a 2D radiographic image of the object can be reconstructed. For getting these parameters, a water calibration was performed.

This water calibration consisted in irradiating a block of 10 cm of water in vacuum with a proton broad field and beam energies ranging from 45 until 100 MeV with 5 MeV steps. For each one of the initial beam energies, the maximum energy deposition inside the water block was retrieved and correlated to its position — the Bragg peak positions, or range values, were extracted from the Bragg curves (figure 4.12). Equation 2.9 was then fitted to the extracted range and corresponding energy values, resulting in α and p fitting parameters equal to 0.0020 MeV/cm^{-1} and 1.7944, respectively (figure 4.13). These values are in agreement with published values for water [82–84].

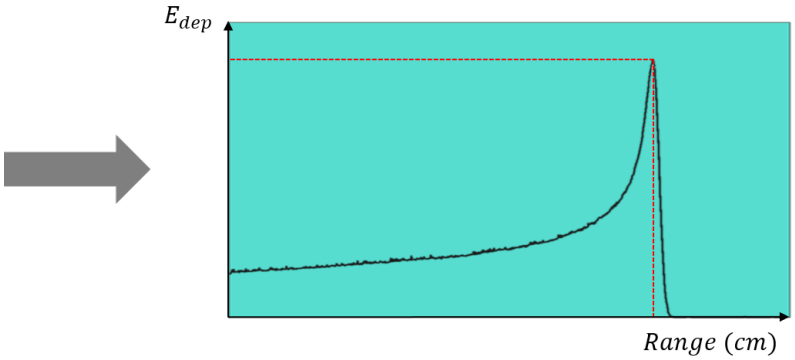

Figure 4.12: Water calibration scheme. After irradiating the water block (blue) with each one of the different energy beams (gray), the maximum energy deposition is scored and the corresponding range values are assessed.

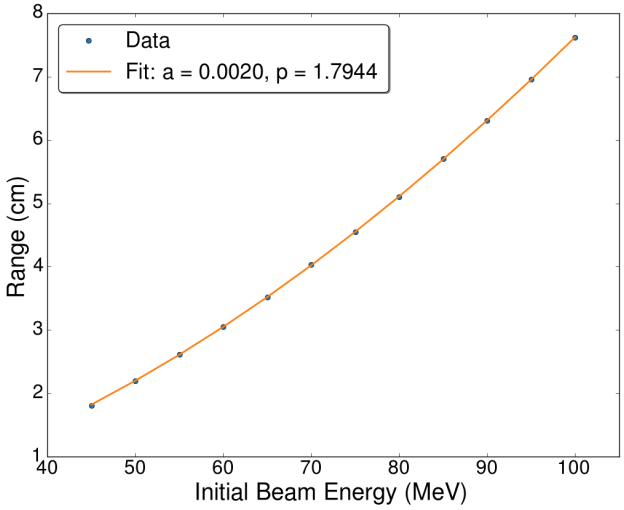

Figure 4.13: Range in water as a function of the initial beam energy. The orange line represents the fit according to equation 2.9.

4.4.2 Signal Decomposition

The signal decomposition (SD) is based on the *Bragg peak decomposition* (BPD) described in [41] and [85].

In the presence of different material interfaces within a phantom, multiple information arises in the signal [85]. Consequently and depending on the beam position relative to those interfaces, the maximum energy deposition in the detector may not always correspond to the most relevant WET contribution [86]. Therefore, a linear combination of multiple overlapping *inverse Bragg curves* describes the signal. Deriving the individual *inverse Bragg curves* within one pixel and their corresponding

WET contributions, the so-called weights, is the rationale of this technique [41]. For that, the measured or simulated signal is decomposed into its several Bragg curves [85]. Afterwards, the decomposed Bragg curves are organized in a Monte Carlo-based lookup-table (LUT) matrix and weighted according to a weight-vector. The specific weight values are obtained by solving a linear least-squares problem, with bound constraints, by means of Euclidean distance minimization [85] (equation 4.3):

$$\min \frac{1}{2} \left(A \cdot \vec{x} - \vec{b} \right)^2, \tag{4.3}$$

where A corresponds to the LUT matrix, $\vec{b}$ corresponds to the Bragg curve signal obtained from the detector, i.e., the energy deposition vs. initial beam energy curve, and $\vec{x}$ corresponds to the weight-coefficient vector to be determined. The LUT matrix was obtained from a series of Monte Carlo simulations of a water block with increasing thickness being irradiated by different initial beam energies. The chosen range of thicknesses was 1.8 cm to 4.6 cm (with 0.05 cm steps) due to the corresponding ranges of protons in water for an energy range of 45 to 75 MeV (with 0.5 MeV steps) [25]. Each entry of the matrix contains the mean energy deposition within the water block for a specific combination of thickness and initial beam energy (figure 4.14).

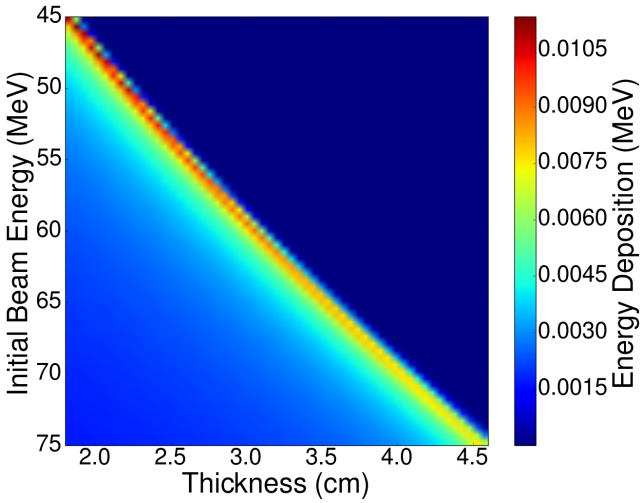

Figure 4.14: Monte Carlo-based lookup-table. The individual Bragg curves used for the signal decomposition are vertically aligned.

For the WET conversion the initial data is median filtered. The signal of each pixel (figure 4.15 (a), blue line) is compared to the LUT matrix so that it can be decomposed in each one of its *inverse Bragg curves*. Subsequently, the contribution of each *inverse Bragg curve* is translated into a weight-thickness dependence (figure

4.15 (b)). This weight-thickness dependence is normalized by the total weight sum and a 10% threshold is defined to minimize the effects of noise (figure 4.15 (c)). Finally, the weighted arithmetic mean of the normalized weights (w_i) for each thickness (x_i) and above the threshold is calculated giving the final WET value for each pixel (figure 4.15 (d)) (equation 4.4):

$$WET = \frac{\sum (w_i x_i)}{\sum w_i}. \tag{4.4}$$

For control purposes, a final signal profile can be obtained and compared to the initial signal. In other words, multiplying the LUT matrix (figure 4.14) by the final weights profile (figure 4.15 (d)), provides the result of the linear least-squares problem solving, the so-called final vector (figure 4.15 (a), orange line). Comparing the final vector with the initial vector (figure 4.15 (a), blue line) allows assessing whether the linear least-squares problem solving was successful or not.

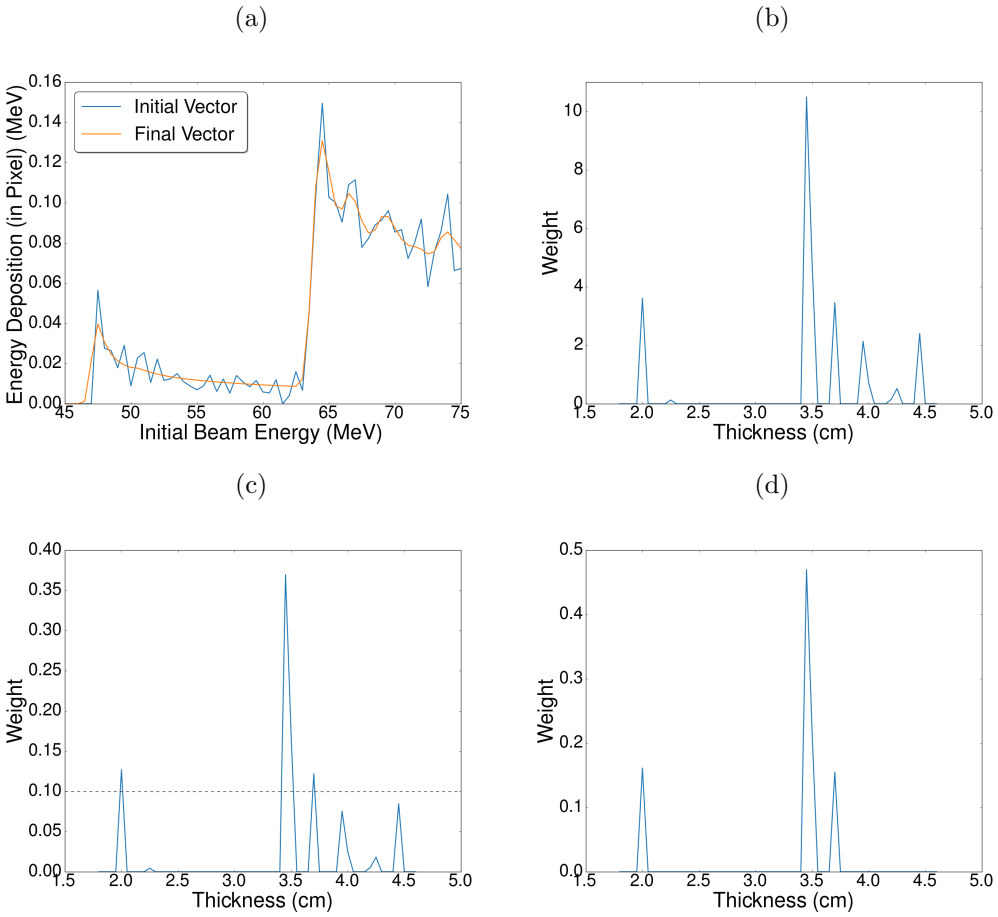

Figure 4.15: Example of the SD process. (a) Energy deposition vs. initial beam energy profile, (b) corresponding weight-coefficient vector profile, (c) normalized weights profile and 10% threshold and (d) final weights profile.

4.5 Image Quality Assessment

This section will present the different quantities used for assessment of the image quality.

In order to compare the reconstructed WET images with the true WET image, all the metrics will be relative to established margins within each insert and within the entire object. Due to the transition between water and each one of the materials, there are large WET gradients close to the interfaces of each entity. These gradients cause scattering and thus a *blurring* effect in those areas. Therefore, the regions of interest (ROIs) are defined by three pixel inner and outer margins (figure 4.16, dashed lines) around the insert interfaces (figure 4.16, non-dashed lines). The inner ROIs are considered for all the calculations concerning the four inserts (adipose tissue, compact bone, PMMA, and striated muscle), and the outer ROIs are considered for all the calculations concerning the water block.

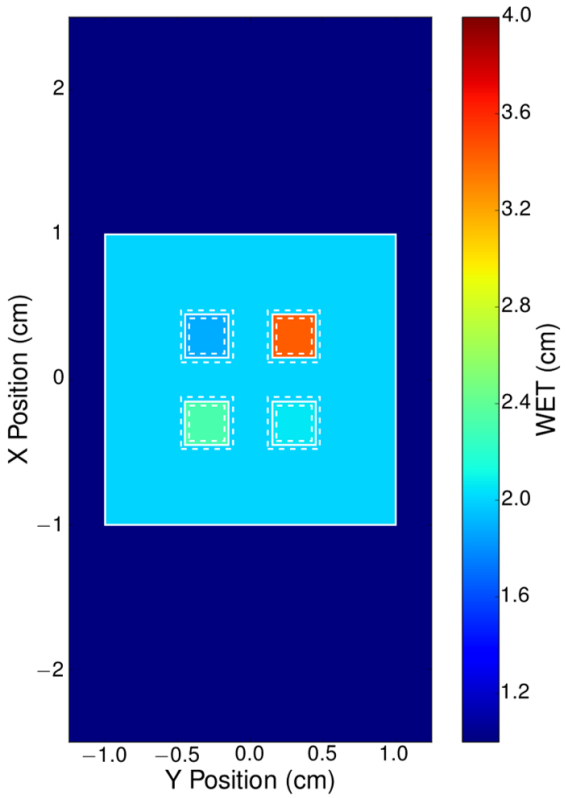

Figure 4.16: Established margins for assessing the image quality. This image contains the true WET values of each material and the corresponding ROIs (dashed lines) around the material interfaces (non-dashed lines). From left to right, top to bottom the inserts are: adipose tissue, compact bone, PMMA and striated muscle.

4.5.1 Relative Error

The relative error (RE) is a measure for the accuracy of the reconstructed WET image. It is calculated for each area of interest according to (equation 4.5):

$$RE = \frac{|WET_{true} - WET_{ROI}|}{WET_{true}}. \tag{4.5}$$

WET_{true} and WET_{ROI} represent the expected and the reconstructed mean WET for a specific region, respectively.

4.5.2 Root-Mean-Square Error

The root-mean-square error (RMSE) is a measure for the differences between reconstructed values and expected values for each pixel individually (equation 4.6):

$$RMSE = \sqrt{\frac{\sum_{i=1}^{N} \left(WET_i^{true} - WET_i^{reconstruction}\right)^2}{N}}, \tag{4.6}$$

where the sum goes over all the N pixels of the area of interest, $\mathrm{WET}_i^{reconstruction}$ is the calculated WET value for the i-th pixel in the reconstructed image and WET_i^{true} is the true WET value for the same pixel.

The normalized root-mean-square error can then be calculated by dividing the RMSE by a mean of normalization (equation 4.7):

$$NRMSE = \frac{RMSE}{WET_{true}}. \tag{4.7}$$

Here, the chosen mean of normalization was the true WET value of the ROI but other options such as the range of the measured data (difference between the maximum and minimum WET values) can be found in the literature.

4.5.3 Spatial Resolution Assessment

To assess the spatial resolution of the obtained images, a method described in [87] was used. In a first step, WET profiles along 10 lines within the central 1 mm of each insert were obtained. The central 1 mm was chosen to reduce the influence of the lateral interfaces. Since the goal was to obtain the spatial resolution in the x and y dimensions, each insert was scanned in two of its interfaces (figure 4.17).

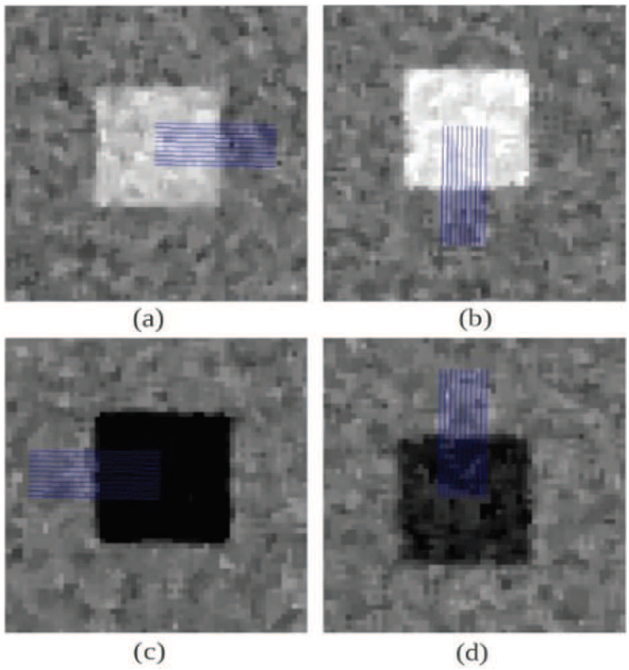

Figure 4.17: Example of the scan lines (blue) across the interfaces of four materials [87].

Afterwards, a sigmoid function was fitted to the mean of these lines (equation 4.8) (figure 4.18) [87]:

$$f(x) = a_1 + \frac{a_2}{1 + e^{-\frac{x-a_3}{a_4}}}, \tag{4.8}$$

where a_1 represents the starting value of the curve, a_2 represents the ending value of the curve, a_3 represents the position of the inflexion point, and a_4 represents the width of the inflection [87].

Subsequently, the 25% and 75% points of the sigmoidal fit were extracted and their physical distance — the FWHM — was determined. Posteriorly, this FWHM was used for creating a Gaussian corresponding to the line-spread function (LSF) (equation 4.9):

$$LSF = \frac{1}{\sigma\sqrt{2\pi}} e^{-\frac{1}{2}\left(\frac{x-\mu}{\sigma}\right)^2}, \tag{4.9}$$

in which μ represents the expected value of the distribution and σ — the standard deviation — equals to FWHM/2.35482.

Ultimately, the MTF is obtained by applying a discrete Fourier transform to the LSF (equation 4.10):

$$MTF = \mathscr{F}[LSF]. \tag{4.10}$$

The final spatial resolution values correspond to the 10% MTF points (figure 4.19).

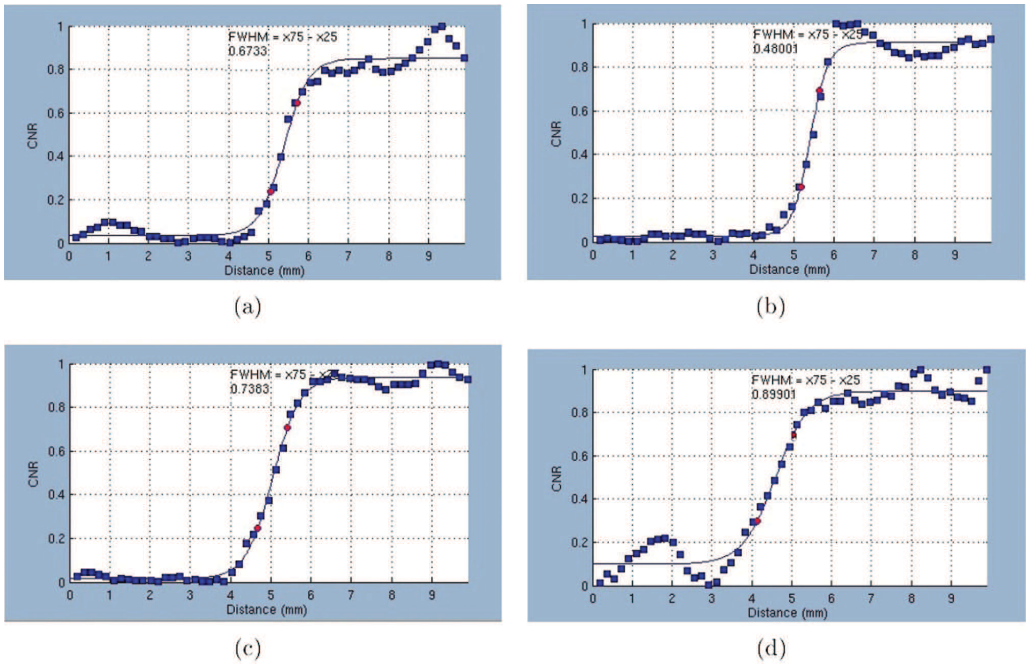

Figure 4.18: Example of the sigmoidal fit of four material interfaces. The 25% and 75% points shown in red are used for calculating the FWHM [87].

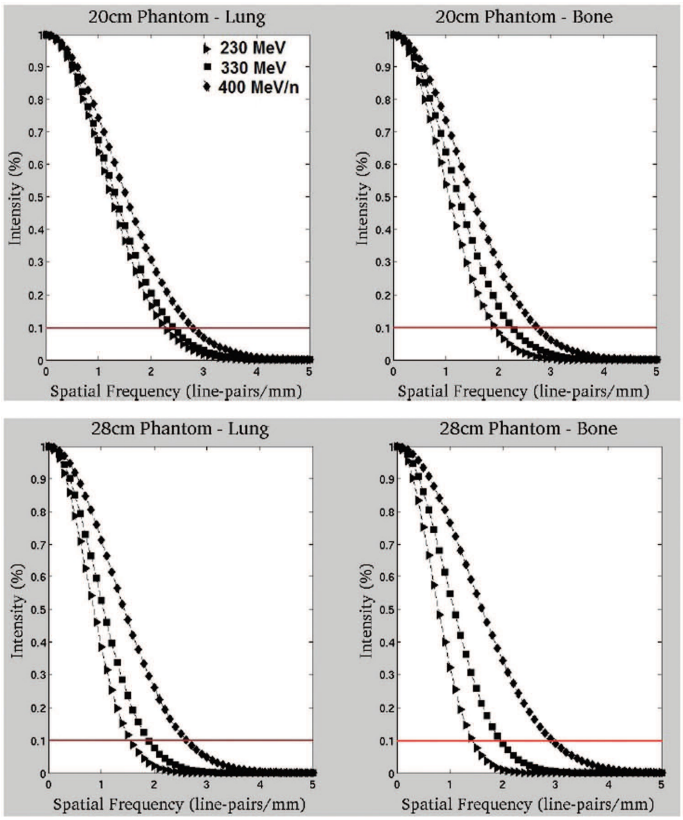

Figure 4.19: Example of the modulation transfer function and of the 10% points [87].

4.6 Time Estimation for Radiographic Imaging

The feasibility of an imaging scheme is also determined by the time required for obtaining a radiographic image. The parameters contributing to the total duration of irradiation schemes such as the one presented (section 4.1.1) are the time required to move the object, the time required for irradiation/imaging and the time required for changing the beam energy, as well as the total number of different beam positions (n_b) and the total number of different energies (n_e).

An ideal system should perform the longest task fewer times. Therefore, in cases where t_e is larger than t_m, the object should be irradiated in all the desired beam positions before changing the energy (figure 4.20). Hence, the object is irradiated in all the different beam positions for one energy. Once the entire object is scanned, the energy is changed and the scanning restarts. This will happen for all the energies. Accordingly, the total duration can be calculated by (equation 4.11):

$$t = n_b \cdot t_i \cdot n_e + n_e \cdot (n_b - 1) \cdot t_m + (n_e - 1) \cdot t_e \tag{4.11}$$

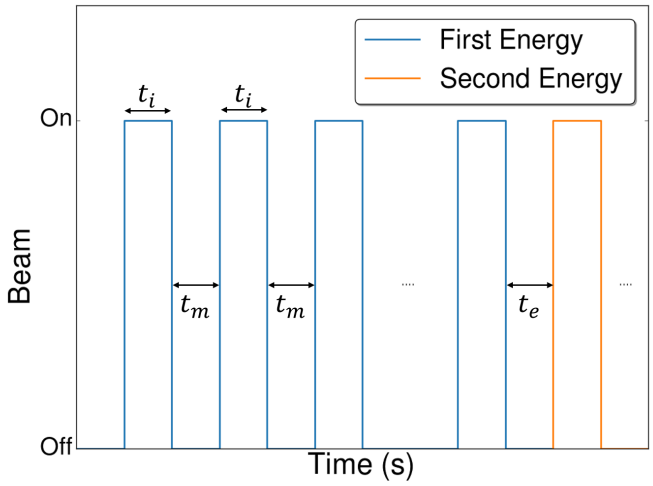

Figure 4.20: Steps of an irradiation setup where the time required for changing the energies is larger than the time required for moving the object. t_i is the irradiation time, t_m is the time for moving the object and t_e is the time for changing the energy.

On the other hand, in cases where t_m is larger than t_e, the object should be irradiated with all energies first before being moved (figure 4.21). The object is thus irradiated with all the different energies for one beam position. Then, the object is moved and

irradiation with all energies restarts. This will happen for all the beam positions. Thus, the total duration can be calculated by (equation 4.12):

$$t = n_b \cdot t_i \cdot n_e + n_b \cdot (n_e - 1) \cdot t_e + (n_b - 1) \cdot t_m \tag{4.12}$$

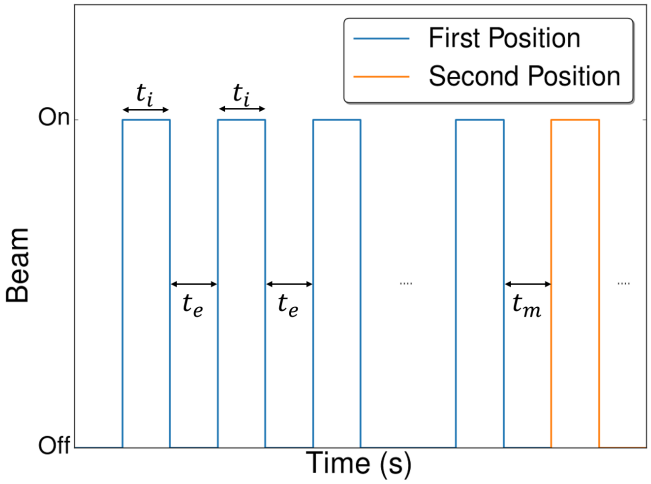

Figure 4.21: Steps of an irradiation setup where the time required for moving the object is larger than the time required for changing the energies. t_i is the irradiation time, t_m is the time for moving the object and t_e is the time for changing the energy.

5

Results and Discussion

Chapter 5 will present all the obtained results for the tests performed throughout this thesis. Firstly, a comparison between the two image reconstruction methods will be made (section 5.1). Next, the impact of changing the different parameters of the FLUKA Monte Carlo simulations will be analyzed (sections 5.2 to 5.4). Finally, the results of the time estimation for obtaining a radiographic image with the proposed setup will be shown (section 5.5).

5.1 Image Reconstruction Methods Comparison

Two image reconstruction methods were presented in section 4.4: the peak finding (PF) and the signal decomposition (SD).

5.1.1 Peak Finding

Using the standard set of parameters for the FLUKA Monte Carlo simulations (section 4.1.1, table 4.2), and the y fan beam approach, the WET distributions shown in figures 5.1 to 5.3 were obtained. Figure 5.1 shows the comparison between the reconstructed WET image and the true WET image. It can easily be seen that in the former one the compact bone and PMMA inserts cannot be distinguished from water. Figure 5.2 depicts the WET profiles along the dimension of the fan beam movement (y dimension), (a) represents a profile along the center of the adipose tissue and compact bone inserts and (b) represents a profile along the center of the PMMA and striated muscle inserts. Likewise, figure 5.3 depicts the WET profiles along the dimension perpendicular to the fan beam movement (x dimension), (a) represents a profile along the center of the PMMA and adipose tissue inserts and (b) represents a profile along the center of the striated muscle and compact bone inserts. In both figures, the dashed lines correspond to the true WET profiles.

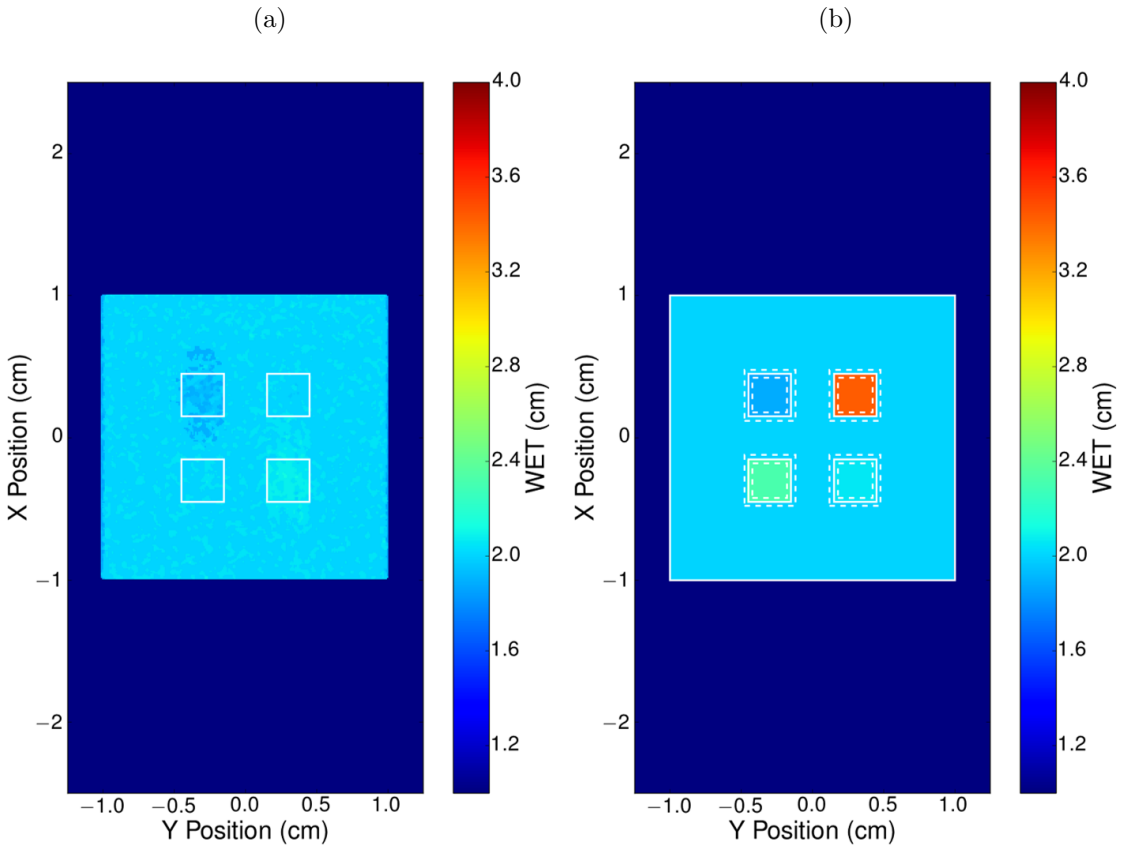

Figure 5.1: Comparison between (a) the reconstructed WET image and (b) the true WET image. In (b), from left to right, top to bottom the inserts are: adipose tissue, compact bone, PMMA and striated muscle. The dashed lines represent the established margins for posterior image quality assessment.

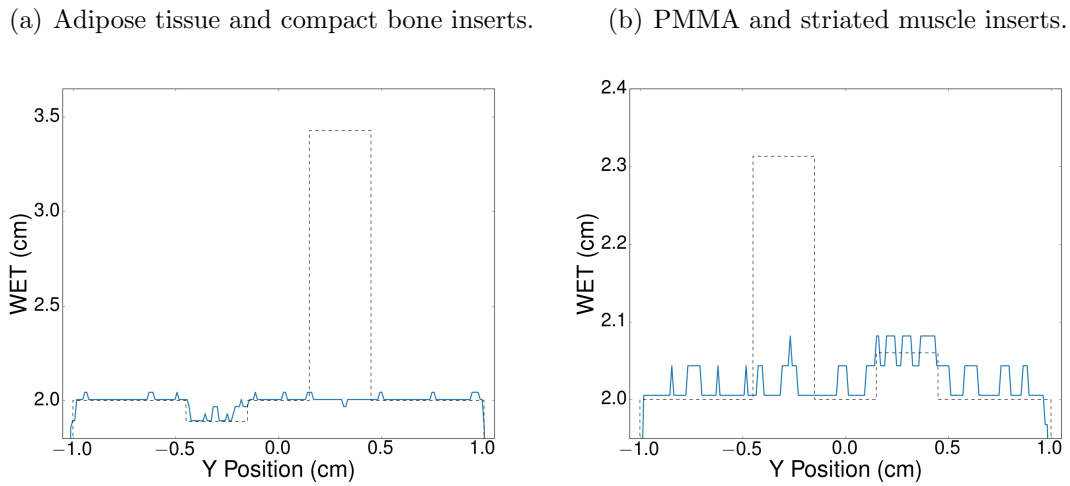

Figure 5.2: WET profiles along the horizontal dimension of (a) the adipose tissue and compact bone inserts and of (b) the PMMA and striated muscle inserts. The dashed lines correspond to the true WET profiles.

(a) PMMA and adipose tissue inserts. (b) Striated muscle and compact bone inserts.

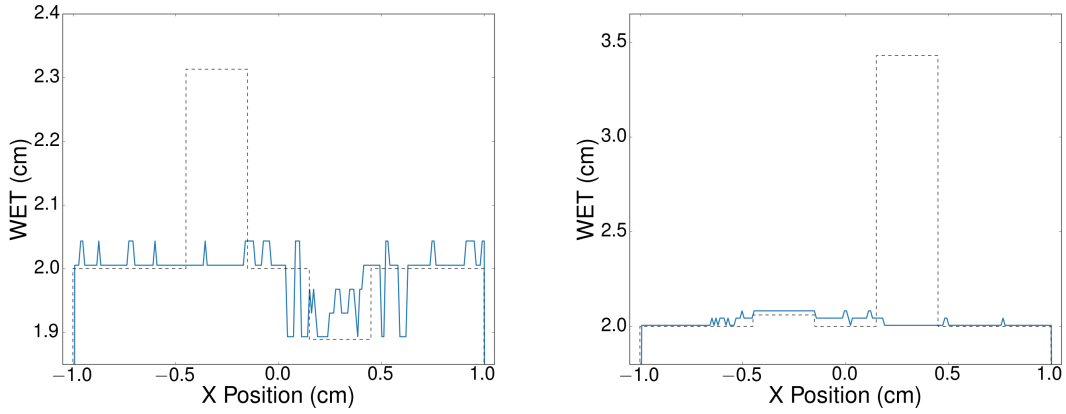

Figure 5.3: WET profiles along the vertical dimension of (a) the PMMA and adipose tissue inserts and of (b) the striated muscle and compact bone inserts. The dashed lines correspond to the true WET profiles.

Analyzing figures 5.2 and 5.3, the poor reconstruction results of the compact bone and PMMA inserts in figure 5.1 are clarified: in none of the cases the true WET value is ever reached. In figure 5.2 (a) and in figure 5.3 (b), the WET values for the compact bone insert do not deviate from approximately 2 cm, instead of the expected 3.43 cm. Similarly, in figure 5.2 (b) and in figure 5.3 (a), the WET values for the PMMA insert also do not deviate from approximately 2 cm, instead of the expected 2.31 cm. In terms of image quality assessment, tables 5.1 and 5.2 corroborate these findings.

Table 5.1: RMSE and NRMSE values of the PF method.

Entity	RMSE (cm)	NRMSE (%)
Water	0.02	1.11
Adipose tissue	0.07	3.88
Compact bone	1.42	41.39
PMMA	0.30	12.89
Striated muscle	0.02	1.08

Table 5.2: Comparison between the true WET values and the mean WET values of the PF method in terms of the relative error.

Entity	True WET (cm)	Mean WET (cm)	Relative error (%)
Water	2.00	2.01	0.59
Adipose tissue	1.89	1.95	3.18
Compact bone	3.43	2.01	41.38
PMMA	2.31	2.02	12.87
Striated muscle	2.06	2.07	0.43

The relative error of the WET reconstruction for the PMMA insert is approximately 13%, while the relative error for the compact bone insert exceeds 40%. The reason for these large discrepancies can be explained by figures 5.4 and 5.5.

Inspecting figure 5.4, the profiles (a) and (d) are characterized by a rather constant falloff in the signal value, while in the profiles (b) and (c) two distinct *peaks* can be found. The justification for this is that, in some occasions, protons going through different paths and, consequently, different materials, reach the same pixel in the detector (figure 5.5, black and red lines). These different paths will influence the overall signal. Taking a look at figure 5.5, proton A, with an initial energy E_1, went through a more dense material, thus having a larger energy loss than proton B, with an initial energy E_2. A larger energy loss translates into a smaller residual energy and a larger energy deposition inside the sensitive detector volume. Hence, correlating the behavior of these two protons with the profile shown in figure 5.4 (b), the second peak, the highest one, would come from protons with a trajectory indicated by A, with a larger energy deposition in the detector, while the first peak, the smaller one, would come from protons with a trajectory indicated by B, with a smaller energy deposition in the detector. In cases like this, because the chosen peak for the WET reconstruction would be the first peak found by the *scipy.signal.argrelextrema* function (figure 5.4 (b), black arrow), the extracted initial beam energy would be the one corresponding to the signal coming from water, although the analyzed detector pixel is behind compact bone (figure 5.5), yielding incorrect WET values.

(a) Adipose tissue insert.

(b) Compact bone insert.

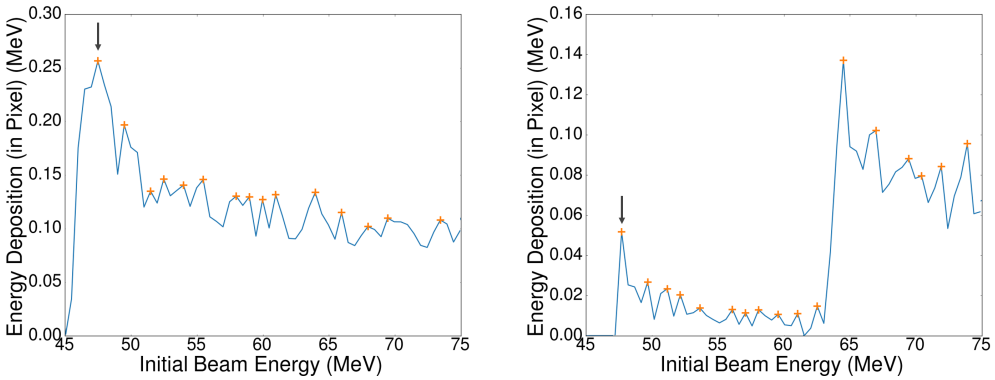

(c) PMMA insert.

(d) Striated muscle insert.

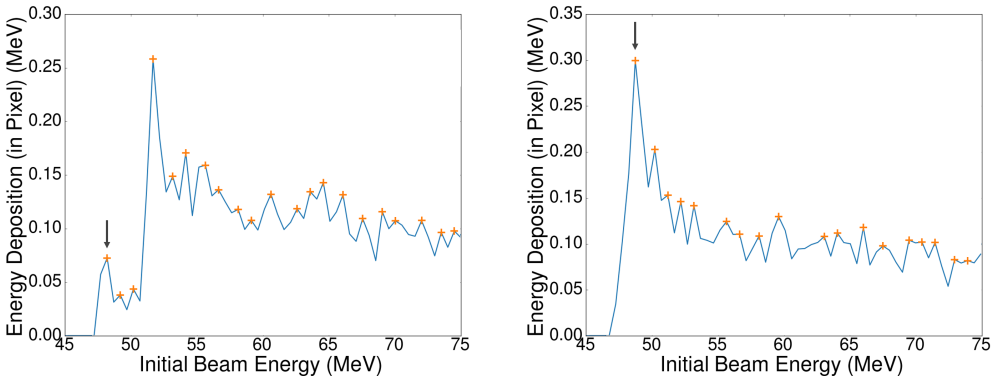

Figure 5.4: Energy deposition vs. initial beam energy profiles of four exemplary pixels corresponding to the four different inserts. The orange markers correspond to the peaks found by the *scipy.signal.argrelextrema* function. The black arrows correspond to the chosen peaks for the WET reconstruction.

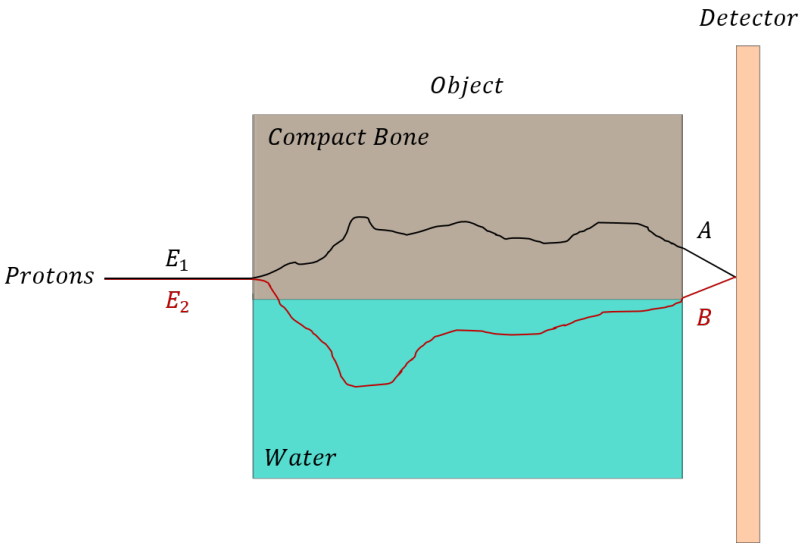

Figure 5.5: Schematic representation of the *double peaks* phenomenon.

Figures 5.6 to 5.8 show the results of choosing the highest peak instead of the first peak found by the *scipy.signal.argrelextrema* function.

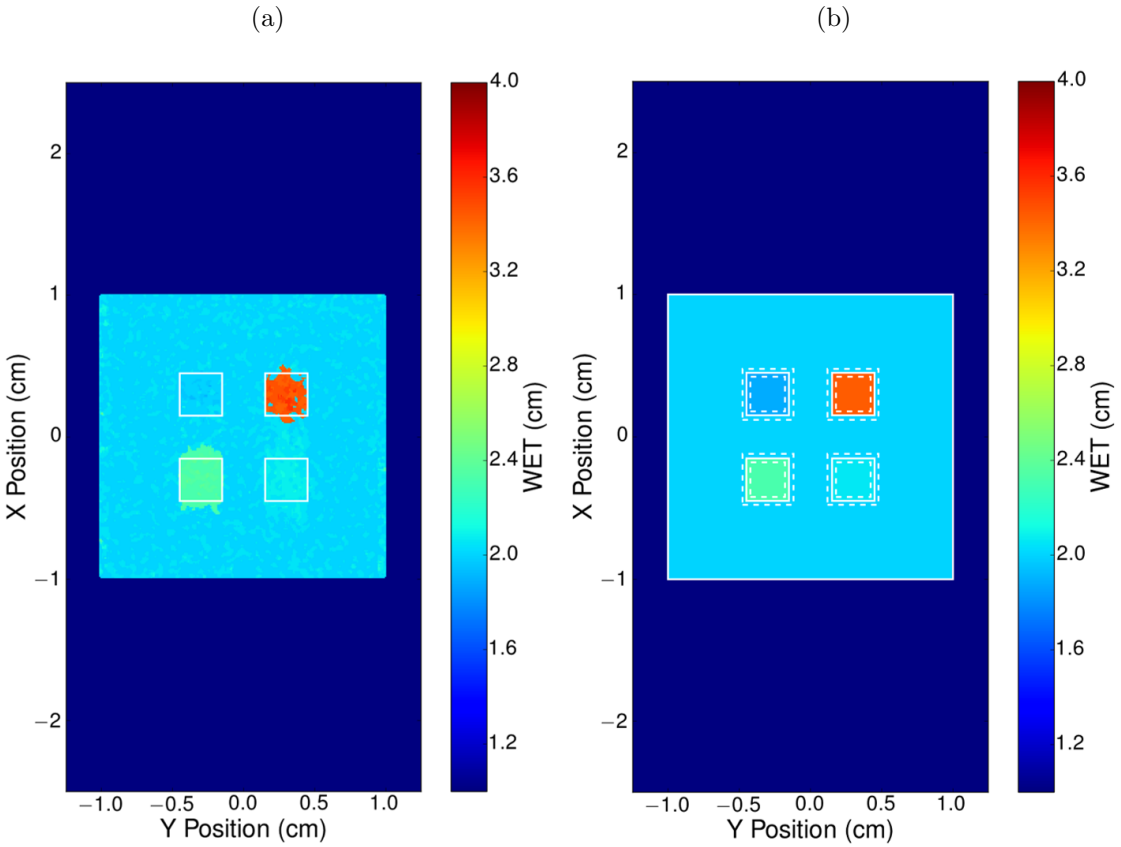

Figure 5.6: Comparison between (a) the reconstructed WET image and (b) the true WET image. In (b), from left to right, top to bottom the inserts are: adipose tissue, compact bone, PMMA and striated muscle.

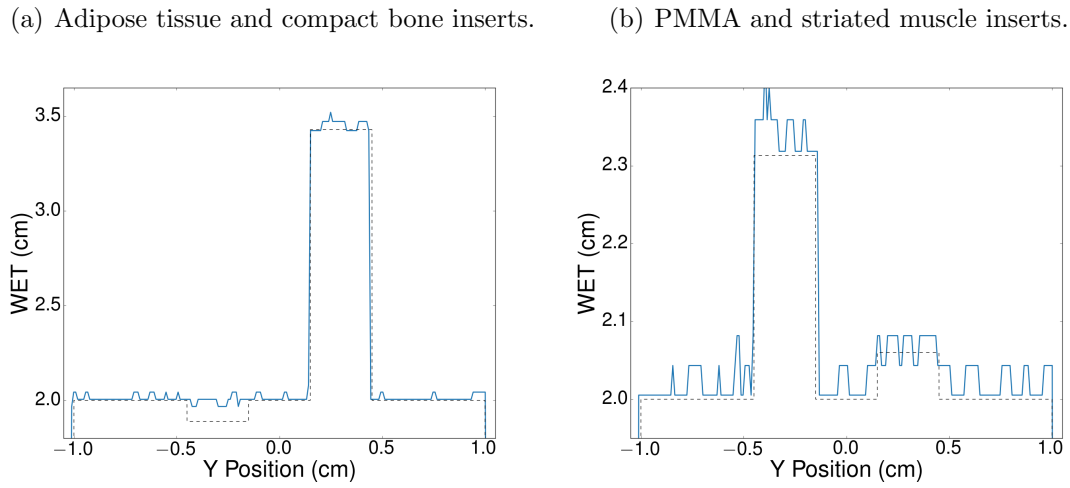

Figure 5.7: WET profiles along the horizontal dimension. The dashed lines correspond to the true WET profiles.

(a) PMMA and adipose tissue inserts.

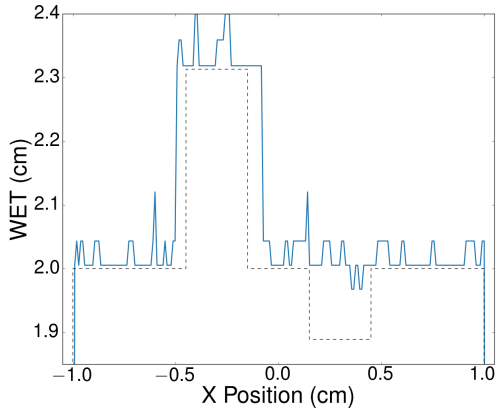

(b) Striated muscle and compact bone inserts.

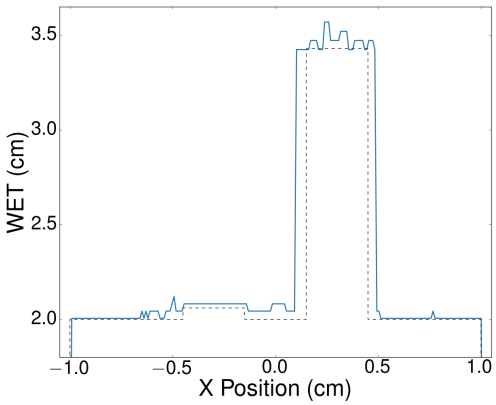

Figure 5.8: WET profiles along the vertical dimension. The dashed lines correspond to the true WET profiles.

Comparing figure 5.6 with figure 5.1, the benefits of choosing the highest peak from the energy deposition vs. initial beam energy profiles can clearly be seen.

Analyzing tables 5.3 and 5.4, the relative errors of the WET reconstruction of compact bone and PMMA decreased to 2.04% and 0.98%, respectively. However, the relative errors of the WET reconstruction of water, adipose tissue and striated muscle increased to 0.84%, 5.98% and 0.67%, respectively.

Table 5.3: RMSE and NRMSE values of the PF method, choosing the highest peak.

Entity	RMSE (cm)	NRMSE (%)
Water	0.05	2.26
Adipose tissue	0.12	6.11
Compact bone	0.39	11.38
PMMA	0.03	1.41
Striated muscle	0.02	1.15

Table 5.4: Comparison between the true WET values and the mean WET values of the PF method, choosing the highest peak, in terms of the relative error.

Entity	True WET (cm)	Mean WET (cm)	Relative error (%)
Water	2.00	2.02	0.84
Adipose tissue	1.89	2.00	5.98
Compact bone	3.43	3.36	2.04
PMMA	2.31	2.34	0.98
Striated muscle	2.06	2.07	0.67

Moreover, one can notice a non-accurate attribution of the compact bone WET value close to the interfaces of the insert. This can be explained by cases such as the ones depicted in figure 5.9. Even though the analyzed detector pixels are behind compact bone, the peaks with the highest energy deposition correspond to water contributions. One can therefore conclude that regardless of choosing the first or the highest peak of the energy deposition vs. initial beam energy profiles, the peak finding approach will always yield a binary (right or wrong) solution in such simple cases with well-defined inserts.

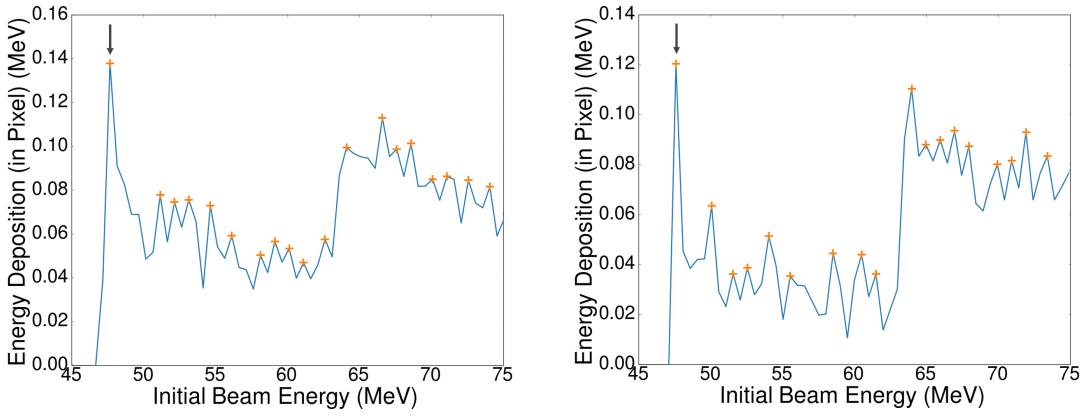

Figure 5.9: Energy deposition vs. initial beam energy profiles of two exemplary pixels corresponding to the compact bone insert. The orange markers correspond to the peaks found by the *scipy.signal.argrelextrema* function. The black arrows correspond to the chosen peaks for the WET reconstruction.

5.1.2 Signal Decomposition

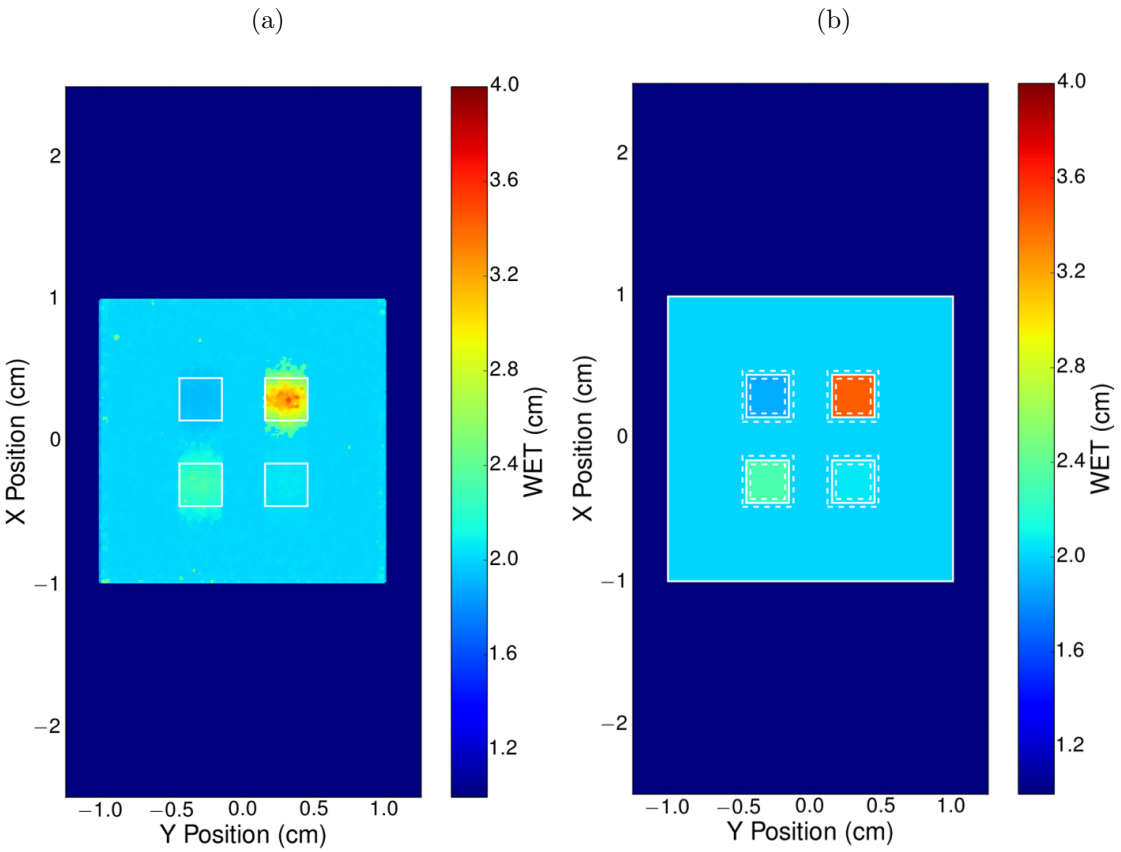

Figure 5.10: Comparison between (a) the reconstructed WET image and (b) the true WET image. In (b), from left to right, top to bottom the inserts are: adipose tissue, compact bone, PMMA and striated muscle.

(a) Adipose tissue and compact bone inserts.

(b) PMMA and striated muscle inserts.

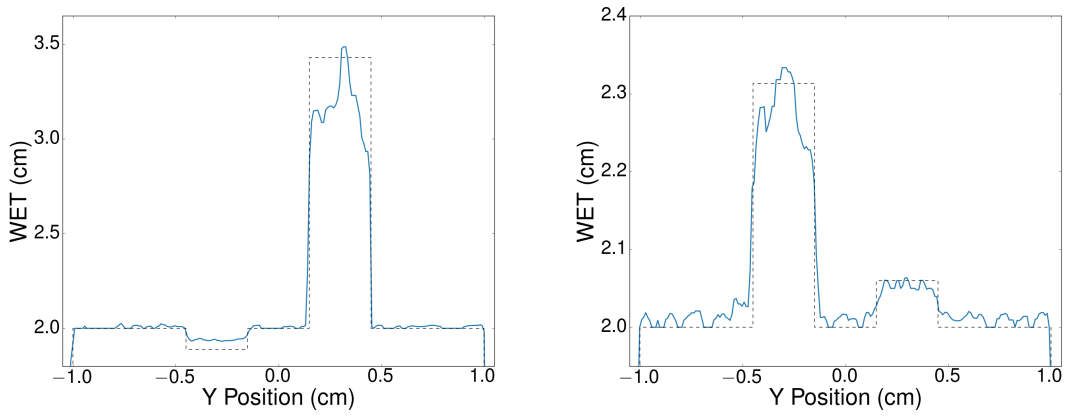

Figure 5.11: WET profiles along the horizontal dimension. The dashed lines correspond to the true WET profiles.

(a) PMMA and adipose tissue inserts.

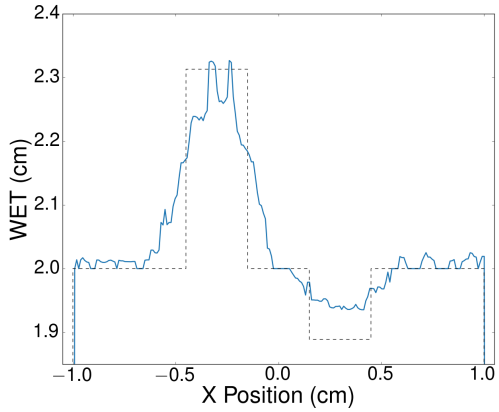

(b) Striated muscle and compact bone inserts.

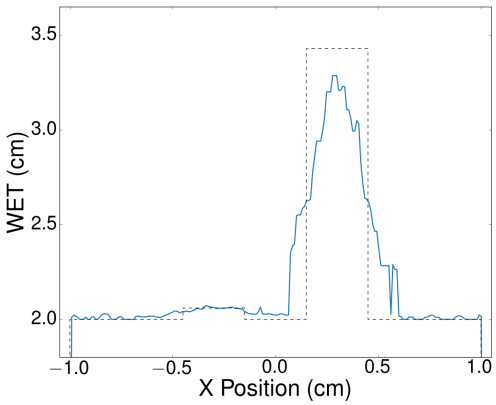

Figure 5.12: WET profiles along the vertical dimension. The dashed lines correspond to the true WET profiles.

WET distributions and one-dimensional WET profiles are shown in figures 5.10 to 5.12. The improvements when compared to the PF method are indisputable. All inserts can now be identified and in the adipose tissue, and striated muscle better agreement between the reconstructed and true WET values was obtained.

A comparison of figures 5.11 and 5.12 reveals that the agreement between reconstructed and true WET values strongly depends on the dimension of the fan beam extension. In this case, the agreement along the dimension where the fan beam goes through (y dimension) is superior to the perpendicular dimension to the fan beam movement (x dimension). This justifies the *blurring* effect present on the vertical dimension of the reconstruction.

RMSE, NRMSE and mean WET values are summarized in tables 5.5 and 5.6. One can notice an overestimation of the WET value in the case of adipose tissue and underestimations for the rest of the inserts. These are explained by the inclusion of all the different signal contributions, coming from the combination of the chosen 10% threshold with the use of the weighted arithmetic mean. As a consequence, the WET values will be shifted towards higher and lower values, resulting in artifacts in the reconstruction method. Furthermore, the largest discrepancy was found for the compact bone insert, with a relative error of approximately 13%, followed by the PMMA and adipose tissue inserts, with relative errors of roughly 3%. Good agreement with differences below 1% was found for water and striated muscle.

Comparing tables 5.5 and 5.6 with tables 5.1 and 5.2, the advantages of the SD method are once again evident. The relative error between mean and true WET values improved to 2.99%, 12.80% and 2.84%, in the cases of the adipose tissue, compact bone, and PMMA inserts, respectively. When compared to tables 5.3 and 5.4, the relative errors increased, but the reconstruction does not have a binary profile anymore. With these findings, it is obvious to conclude that the PF approach is not suitable for the aimed proton radiographic reconstruction. Thus, all the results presented from now on were obtained using the SD method.

Table 5.5: RMSE and NRMSE values of the SD method.

Entity	RMSE (cm)	NRMSE (%)
Water	0.04	2.00
Adipose tissue	0.06	3.03
Compact bone	0.48	14.03
PMMA	0.08	3.58
Striated muscle	0.01	0.62

Table 5.6: Comparison between the true WET values and the mean WET values of the SD method in terms of the relative error.

Entity	True WET (cm)	Mean WET (cm)	Relative error (%)
Water	2.00	2.01	0.71
Adipose tissue	1.89	1.95	2.99
Compact bone	3.43	2.99	12.80
PMMA	2.31	2.25	2.84
Striated muscle	2.06	2.05	0.36

5.2 Beam Shape Comparison

In this section, the influence of the beam shape on the quality of the reconstructed WET distributions will be analyzed. Table 5.7 presents the common parameters to all the types of proton beam.

Table 5.7: Common parameters to the beam shape tests.

Phantom-detector distance	1.5 cm
Energy range	45 – 75 MeV
Energy step	0.5 MeV
Total number of particles	128 000 000

For all obtained results to be comparable, the total number of protons (N_{total}) for each beam shape has to be the same. This quantity is determined by the total number of scanned beams (n_b), the total number of beam energies (n_e) and the number of primaries for each of these simulations (n_p):

$$N_{total} = n_b \times n_e \times n_p. \tag{5.1}$$

The total number of scanned beams depends on the chosen beam type. As the total number of particles and the total number of energies remain unchanged, the only adjusted variable will be the total number of primaries within each simulation, depending on the modality being studied.

5.2.1 Fan Beam

In the fan beam approach, there are two independent cases: the x fan beam and the y fan beam. Furthermore, the possibility of merging the information coming from these two cases introduces a third variation: the merged fan beam (section 4.3.3).

The y fan beam results in terms of WET resolution have already been presented in section 5.1.2. Here, the spatial resolution will be analyzed and presented. Figure 5.13 gives an example of the performed scans.

(a) Vertical scan lines.

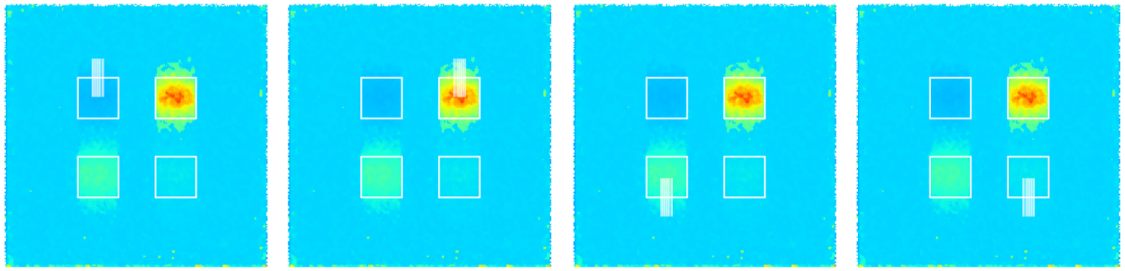

(b) Horizontal scan lines.

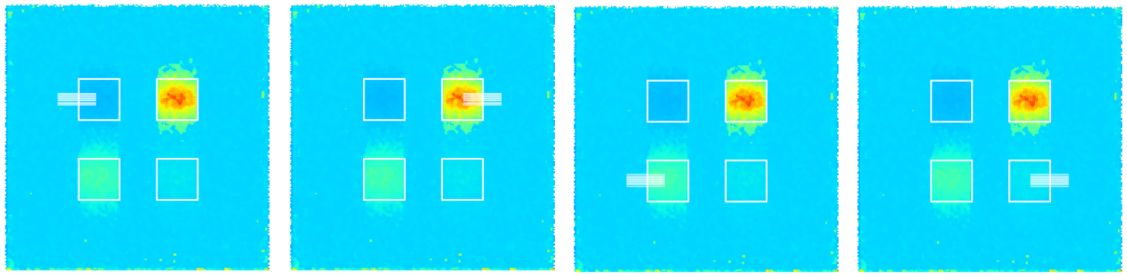

Figure 5.13: Scan lines (white) used for the spatial resolution assessment. From left to right, top to bottom the inserts are: adipose tissue, compact bone, PMMA and striated muscle.

A sigmoid function is fitted to the averaged scan lines (figure 5.14). Afterwards, the LSF is obtained (figure 5.15) by creating a Gaussian with the FWHM, the physical distance between the 25% and 75% points. Finally, the MTF is obtained by applying a discrete Fourier transform to the LSF and the spatial resolution values correspond to the 10% MTF points (figure 5.16).

Figures 5.14 to 5.16 show examples of the followed steps to reach the final spatial resolution results. The obtained spatial resolution values for both dimensions are summarized in table 5.8 for the fan beam moving along the horizontal dimension (y dimension).

Considering the results presented in table 5.8, a better WET calculation in the dimension of the fan beam movement is once more confirmed, showing spatial resolution values below 0.4 mm for all the interfaces. In contrast, the spatial resolution in the dimension perpendicular to the beam movement (x dimension) is about one order of magnitude lower. Calculating the mean resolution, one can conclude that, for the y fan beam approach, the overall spatial resolution in the x dimension equals to (1.74 ± 0.08) mm and the overall spatial resolution in the y dimension equals to (0.24 ± 0.01) mm. The indicated uncertainty represents the variance of the results, meaning their squared deviation from the mean.

(a) Vertical scan lines. (b) Horizontal scan lines.

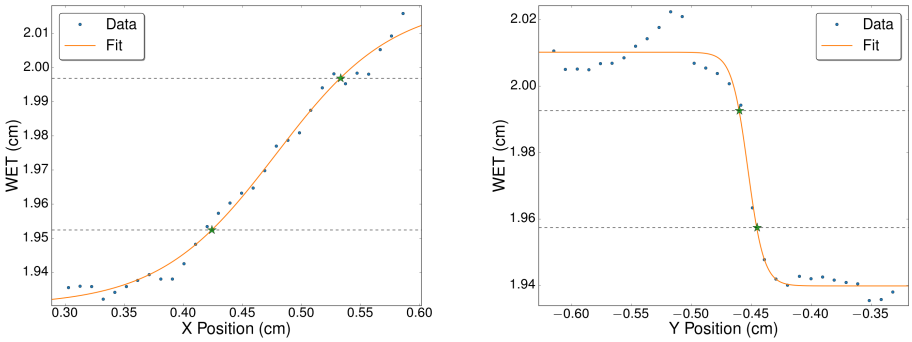

Figure 5.14: Example of the sigmoidal fit. The 25% and 75% points shown in green and highlighted by the horizontal lines were used to obtain the FWHM of the LSF. These figures correspond to the interface between adipose tissue and water.

(a) Vertical scan lines. (b) Horizontal scan lines.

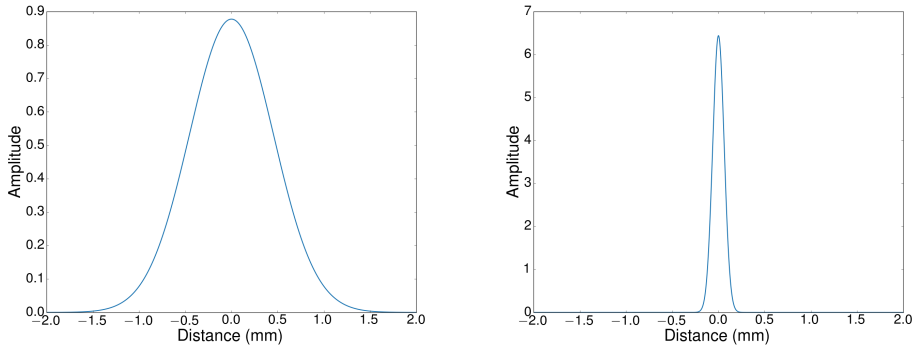

Figure 5.15: Example of the line-spread function. These figures correspond to the interface between adipose tissue and water.

(a) Vertical scan lines. (b) Horizontal scan lines.

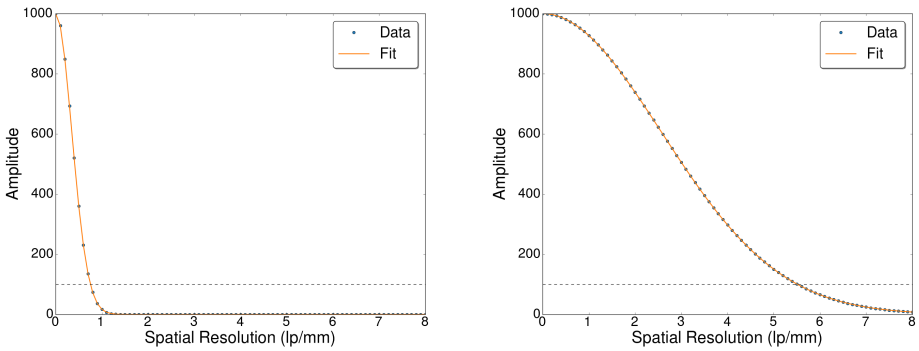

Figure 5.16: Example of the modulation transfer function and of the 10% points. These figures correspond to the interface between adipose tissue and water.

Table 5.8: Spatial resolution of the y fan beam approach.

Interface	Dimension	Spatial resolution (mm)
Adipose tissue/water	x	1.34
	y	0.18
Compact bone/water	x	1.68
	y	0.19
PMMA/water	x	2.00
	y	0.21
Striated muscle/water	x	2.05
	y	0.39

Simulations were also performed with a fan beam moving along the x dimension, using the same simulation parameters.

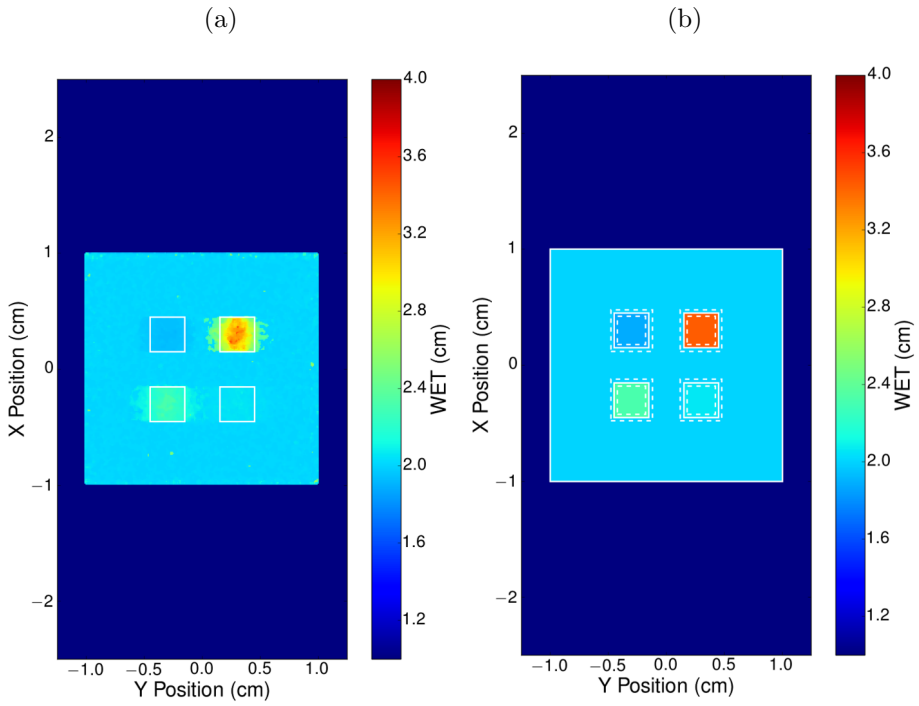

Figure 5.17: Comparison between (a) the reconstructed WET image and (b) the true WET image. In (b), from left to right, top to bottom the inserts are: adipose tissue, compact bone, PMMA and striated muscle.

(a) Adipose tissue and compact bone inserts.

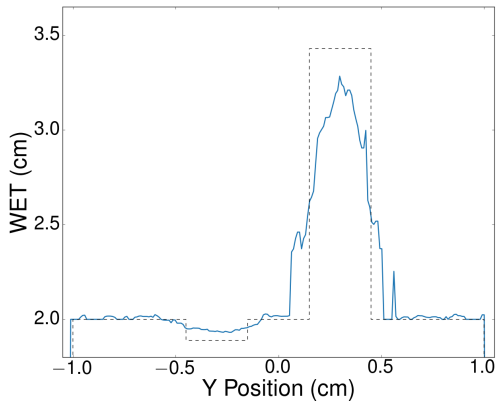

(b) PMMA and striated muscle inserts.

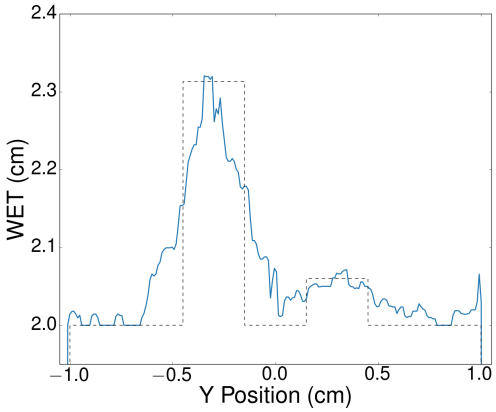

Figure 5.18: WET profiles along the horizontal dimension. The dashed lines correspond to the true WET profiles.

(a) PMMA and adipose tissue inserts.

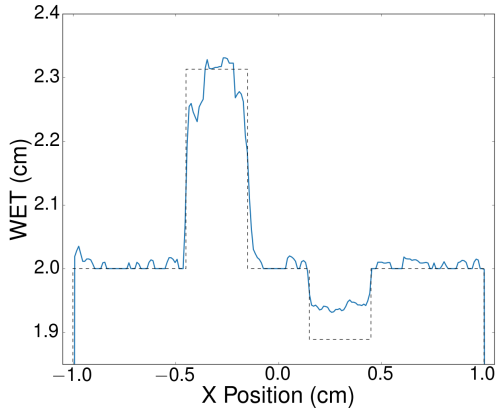

(b) Striated muscle and compact bone inserts.

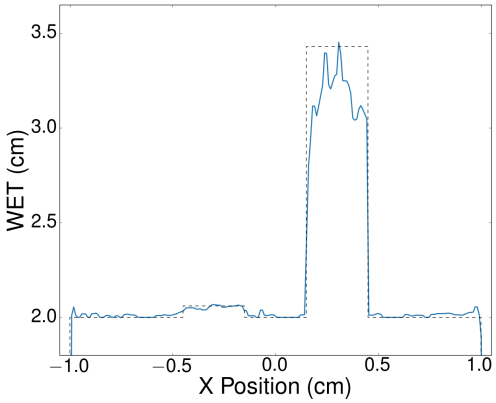

Figure 5.19: WET profiles along the vertical dimension. The dashed lines correspond to the true WET profiles.

Comparing figure 5.17 with figure 5.10, similar results were obtained. As expected, the *blurring* effect is now encountered in the opposite dimension. Accordingly, analyzing figures 5.18 and 5.19, the agreement between reconstructed and true WET values along the x dimension (vertical dimension) is now superior to the one along the y dimension (horizontal dimension). Nevertheless, the overestimation on the adipose tissue WET value, as well as the underestimations on the compact bone, PMMA and striated muscle WET values, are still present.

In terms of RMSE, NRMSE and relative error, the results shown in tables 5.9 and 5.10 are analogous to the ones previously presented in tables 5.5 and 5.6.

The spatial resolution (table 5.11) results also meet the expectations: better performance in the vertical dimension (x dimension) and worse performance in the horizontal dimension (y dimension). Calculating the mean resolution, one can conclude that, for the x fan beam approach, the overall spatial resolution in the x dimension equals to (0.15 ± 0.01) mm and the overall spatial resolution in the y dimension equals to (2.19 ± 0.12) mm.

Table 5.9: RMSE and NRMSE values of the x fan beam approach.

Entity	RMSE (cm)	NRMSE (%)
Water	0.04	1.97
Adipose tissue	0.06	2.99
Compact bone	0.47	13.68
PMMA	0.08	3.64
Striated muscle	0.01	0.64

Table 5.10: Comparison between the true WET values and the mean WET values of the x fan beam approach in terms of the relative error.

Entity	True WET (cm)	Mean WET (cm)	Relative error (%)
Water	2.00	2.01	0.71
Adipose tissue	1.89	1.94	2.96
Compact bone	3.43	3.00	12.50
PMMA	2.31	2.24	3.06
Striated muscle	2.06	2.05	0.49

Table 5.11: Spatial resolution of the x fan beam approach.

Interface	Dimension	Spatial resolution (mm)
Adipose tissue/water	x	0.11
	y	2.56
Compact bone/water	x	0.07
	y	2.06
PMMA/water	x	0.14
	y	2.47
Striated muscle/water	x	0.26
	y	1.68

Because each fan beam case — x and y — provides a good spatial resolution along the dimension perpendicular to its extension, the combination of both data arrays could in principle provide a good spatial resolution in both dimensions. For a fair comparison, the total number of particles and consequently the total dose to the object had to be the same in the merged fan beam variation. As this approach requires separate simulations for each one of the independent fan beams, it obligated the total number of primaries within each simulation to be reduced by half, when compared to the previous situations. Figures 5.20 to 5.22 and tables 5.12 to 5.14 present the results of this approach.

Examining figure 5.20, the overall WET reconstruction of each insert enhanced when compared to the isolated x and y fan beam approaches. Moreover, the *blurring* effect previously encountered is now considerably reduced.

The WET profiles shown in figures 5.21 and 5.22 are more accurate than the ones obtained before: merging the information of both fan beams compensated some of the underestimations noted earlier. However, the overestimation of the WET value of the adipose tissue insert is still present.

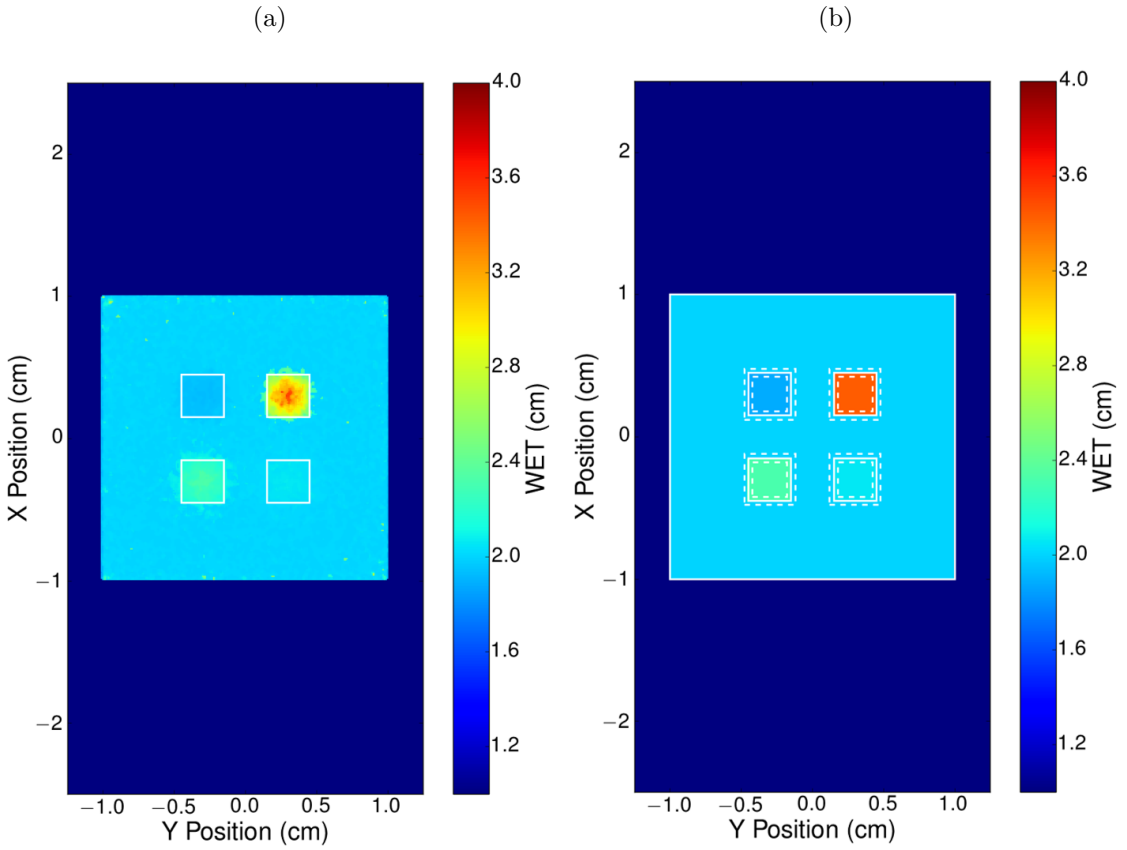

Figure 5.20: Comparison between (a) the reconstructed WET image and (b) the true WET image. In (b), from left to right, top to bottom the inserts are: adipose tissue, compact bone, PMMA and striated muscle.

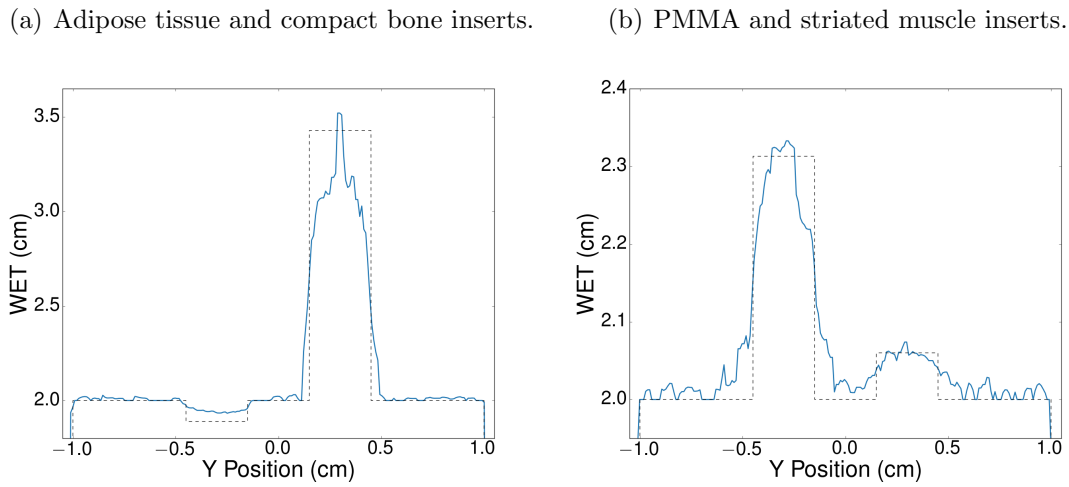

Figure 5.21: WET profiles along the horizontal dimension. The dashed lines correspond to the true WET profiles.

(a) PMMA and adipose tissue inserts.

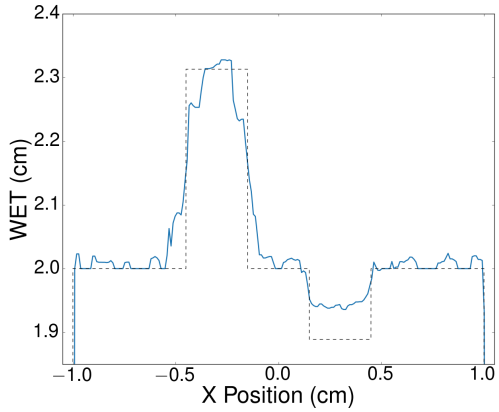

(b) Striated muscle and compact bone inserts.

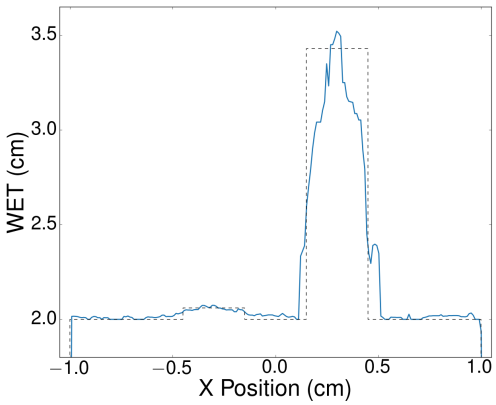

Figure 5.22: WET profiles along the vertical dimension. The dashed lines correspond to the true WET profiles.

When it comes to the RMSE, NRMSE and relative error, the values presented in tables 5.12 and 5.13 agree with the expectations. As before, the largest deviations were found for compact bone with a relative error of approximately 12%, followed by the PMMA and adipose tissue, with again relative errors of roughly 3%. As before, good agreements with differences below 1% were found for water and striated muscle.

Finally, the obtained spatial resolution supports the advantage of the merged fan beam approach as it is comparable in both dimensions. The individual results are in general superior to the ones presented in tables 5.8 and 5.11, yet the spatial resolution values of each insert in both dimensions (x and y) are now in agreement with each other, not having discrepancies larger than 0.24 mm. Calculating the mean resolution, one can conclude that, for the merged fan beam approach, the overall spatial resolution in the x dimension equals to (0.59 ± 0.02) mm and the overall spatial resolution in the y dimension equals to (0.67 ± 0.01) mm.

Comparing the three variants of the fan beam modality, although the x and y fan beam approaches have a better spatial resolution in their dimension of scanning, the spatial resolution in the perpendicular dimension to that one is significantly worse. Even though the merged fan beam approach does not considerably improve the WET resolution it provides good results in terms of spatial resolution. Thus, it can be considered as the adequate fan beam modality.

Table 5.12: RMSE and NRMSE values of the merged fan beam approach.

Entity	RMSE (cm)	NRMSE (%)
Water	0.03	1.30
Adipose tissue	0.06	3.07
Compact bone	0.47	13.69
PMMA	0.08	3.47
Striated muscle	0.01	0.58

Table 5.13: Comparison between the true WET values and the mean WET values of the merged fan beam approach in terms of the relative error.

Entity	True WET (cm)	Mean WET (cm)	Relative error (%)
Water	2.00	2.01	0.58
Adipose tissue	1.89	1.95	3.05
Compact bone	3.43	3.00	12.46
PMMA	2.31	2.25	2.94
Striated muscle	2.06	2.05	0.41

Table 5.14: Spatial resolution of the merged fan beam approach.

Interface	Dimension	Spatial resolution (mm)
Adipose tissue/water	x	0.42
	y	0.48
Compact bone/water	x	0.82
	y	0.71
PMMA/water	x	0.51
	y	0.75
Striated muscle/water	x	0.59
	y	0.74

5.2.2 Spot Scanning

The second beam shape studied in this thesis was the spot scanning approach. Two adjustments were performed to assure a fair comparison to the results obtained with the fan beam approach. Firstly, as the total number of beam spots required to cover the entire phantom is 441, the number of primaries within each individual simulation had to be decreased to maintain the same total number of particles and hence the same imaging dose (equation 5.1). Secondly, as the total number of primaries within each simulation decreased, the total number of primaries per beam also decreased. As a consequence, the total number of particles per detector pixel in the spot scanning approach was approximately 50% smaller than the total number of particles per detector pixel in the fan beam approach. This resulted in larger fluctuations and thus a more noisy data. To compensate that, a higher threshold had to be used in the signal decomposition. Instead of the original 10% threshold, a 15% threshold was chosen for the WET reconstruction presented in this section.

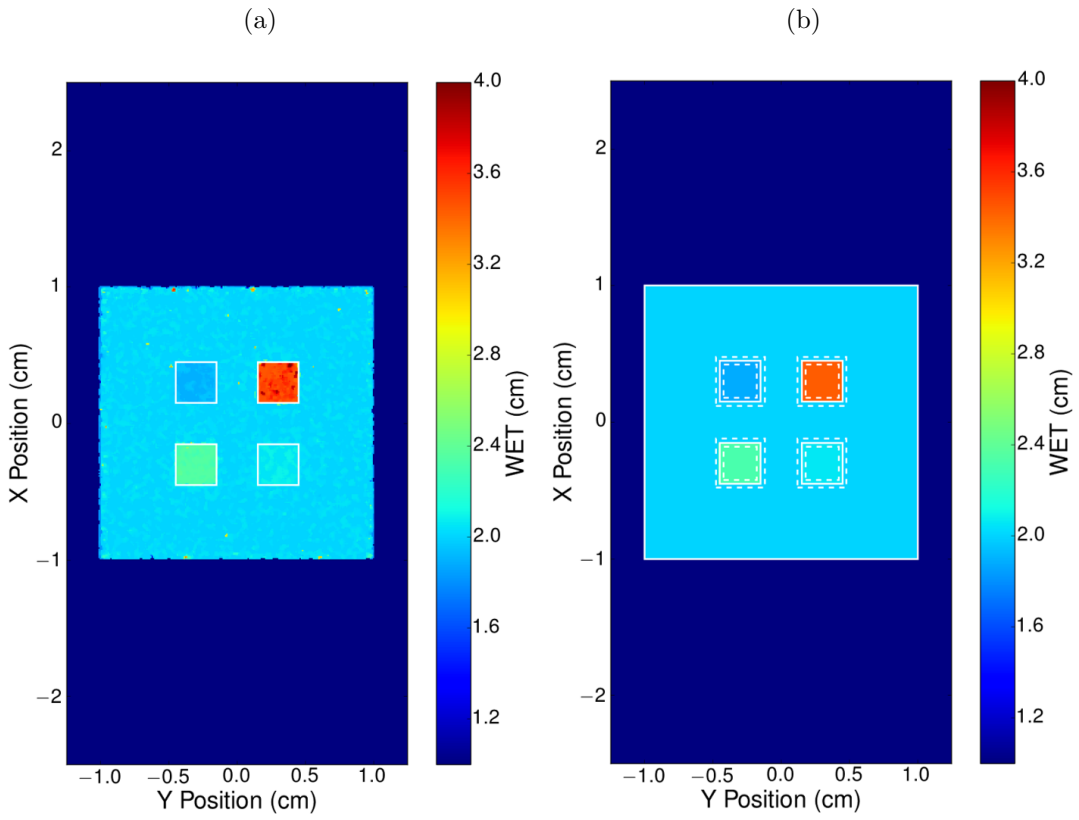

Figure 5.23: Comparison between (a) the reconstructed WET image and (b) the true WET image. In (b), from left to right, top to bottom the inserts are: adipose tissue, compact bone, PMMA and striated muscle.

(a) Adipose tissue and compact bone inserts.

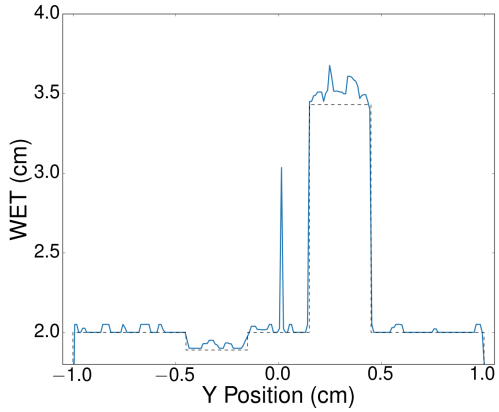

(b) PMMA and striated muscle inserts.

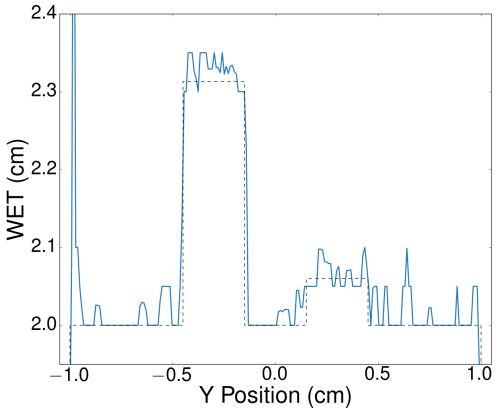

Figure 5.24: WET profiles along the horizontal dimension. The dashed lines correspond to the true WET profiles.

(a) PMMA and adipose tissue inserts.

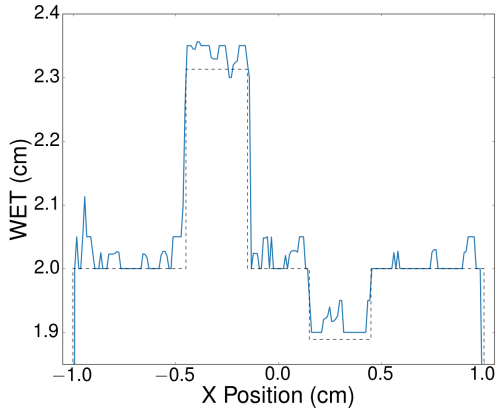

(b) Striated muscle and compact bone inserts.

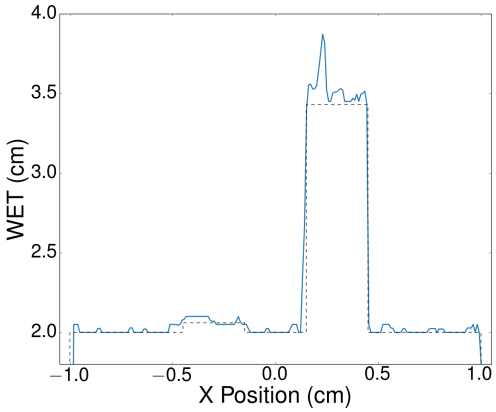

Figure 5.25: WET profiles along the vertical dimension. The dashed lines correspond to the true WET profiles.

Comparing the reconstructed WET image of this beam modality (figure 5.23) with the ones presented before (figures 5.10, 5.17 and 5.20), the improvements in the adipose tissue, compact bone and PMMA inserts are evident. Furthermore, the *blurring* effect present before is now completely suppressed in both dimensions. However, the WET distribution in the water block is less homogeneous than in the previous cases and the agreement between reconstructed and true WET values of striated muscle decreased.

The slight decrease in the overall homogeneity of the reconstruction can be explained when studying figures 5.28 to 5.27. Due to the combination of the increased noise

with the use of the weighted arithmetic mean, in some pixels the calculated WET value is shifted towards even higher WET values (figures 5.26 and 5.27), yielding outliers such as the ones present in figure 5.24. Consequently, the underestimations observed before in the compact bone, PMMA and striated muscle inserts are now overestimations of the WET values (figures 5.24 and 5.25). Moreover, due to not only the increased noise in the signal but also the different applied threshold, in other pixels, the weights obtained from the signal decomposition are not high enough to reach the threshold, and thus no information for the WET calculation is obtained (figure 5.28). In those cases, the final attributed WET value is the mean of the WET values of the 8 neighboring pixels. Nonetheless, the global WET calculation accuracy is still better than in the fan beam approach. Still concerning figures 5.26 and 5.27, the outliers observed in the 4.5 cm thickness come from the high statistical fluctuations raised by the low number of delivered protons.

Tables 5.15 to 5.17 support the conclusions drawn from figures 5.23 to 5.25 and the reason why the spot scanning approach yields superior results. A smaller beam reduces the contributions of multiple Coulomb scattering. Yet, one can notice that the WET profiles became steeper, meaning that using a 15% threshold slowly approaches the binary solution characteristic of the peak finding method. In terms of RMSE, NRMSE and relative error, the poorest WET reconstruction is still the one corresponding to the compact bone insert, but with a relative error of only 2.8%. Also, the relative errors encountered for PMMA and adipose tissue are smaller than 1.5%. For the water block and striated muscle, the mean WET values are comparable to the ones obtained before.

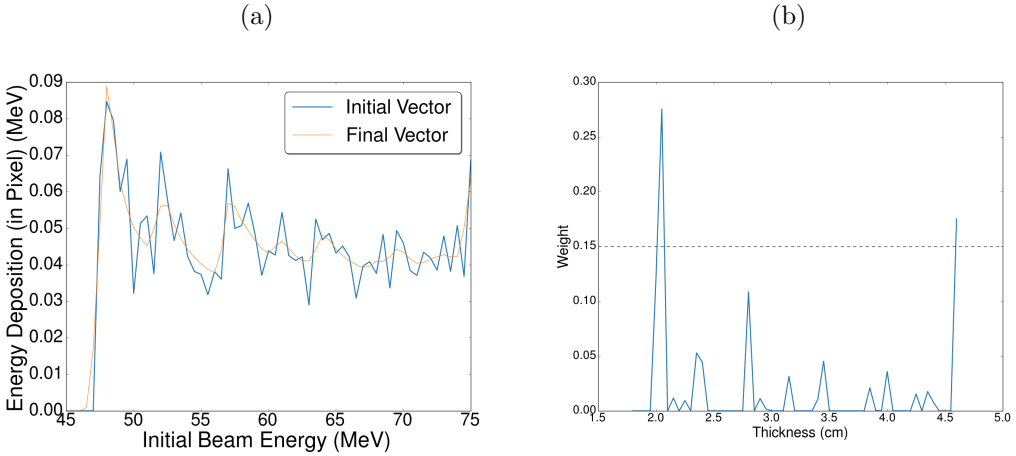

Figure 5.26: (a) Energy deposition vs. initial beam energy profile and (b) weight profile of a lower water pixel.

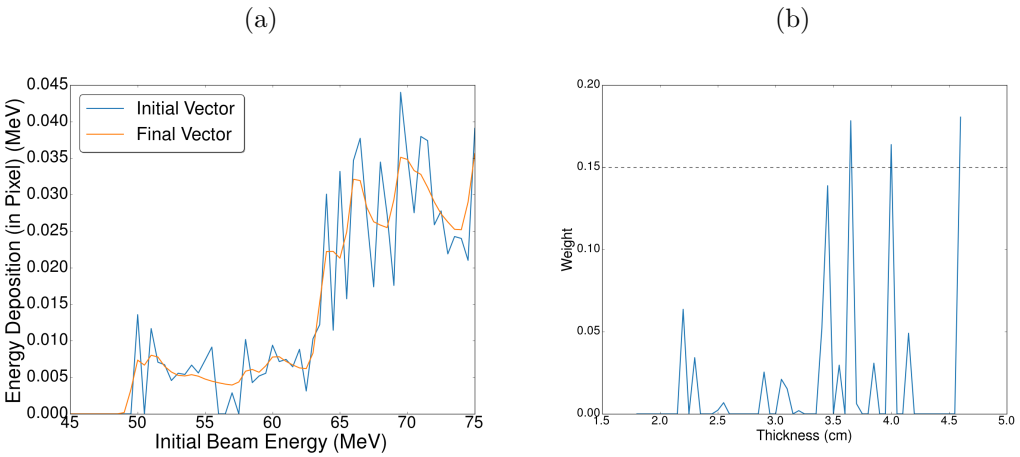

Figure 5.27: (a) Energy deposition vs. initial beam energy profile and (b) weight profile of a compact bone pixel.

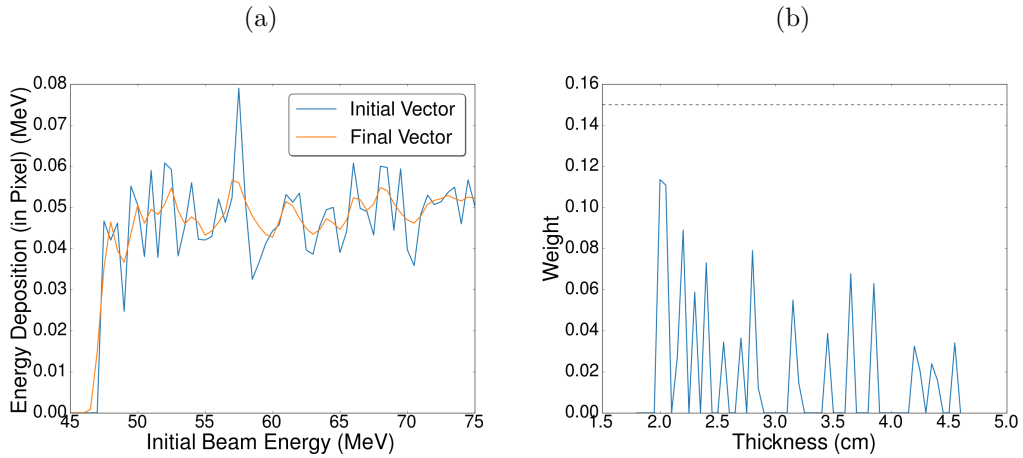

Figure 5.28: (a) Energy deposition vs. initial beam energy profile and (b) weight profile of an upper water pixel.

Table 5.15: RMSE and NRMSE values of the spot scanning approach.

Entity	RMSE (cm)	NRMSE (%)
Water	0.04	1.95
Adipose tissue	0.03	1.79
Compact bone	0.13	3.71
PMMA	0.03	1.47
Striated muscle	0.02	1.17

Table 5.16: Comparison between the true WET values and the mean WET values of the spot scanning approach in terms of the relative error.

Entity	True WET (cm)	Mean WET (cm)	Relative error (%)
Water	2.00	2.02	0.78
Adipose tissue	1.89	1.92	1.45
Compact bone	3.43	3.53	2.80
PMMA	2.31	2.34	1.27
Striated muscle	2.06	2.07	0.58

Calculating the mean of the spatial resolution results, one can conclude that, for the spot scanning approach, the overall spatial resolution in the x dimension equals to (0.100 ± 0.001) mm and the overall spatial resolution in the y dimension equals to (0.34 ± 0.18) mm. The 1.08 mm in the y dimension of the striated muscle/water interface can be explained by the proximity between the WET values of these two materials (section 4.3.2, table 4.1). Because of the small difference in the two respective WET values, the sigmoidal fit fails and thus the spatial resolution is worse.

Table 5.17: Spatial resolution of the spot scanning approach.

Interface	Dimension	Spatial resolution (mm)
Adipose tissue/water	x	0.14
	y	0.12
Compact bone/water	x	0.05
	y	0.06
PMMA/water	x	0.11
	y	0.10
Striated muscle/water	x	0.09
	y	1.08

5.2.3 Broad Field

The last beam shape tested was the broad field approach. This approach consists of one single square beam covering the entire dimensions of the object. As a result, the contributions of multiple Coulomb scattering would be more pronounced, and thus a worse reconstruction performance was expected.

For a fair comparison with the other techniques, some adjustments were made to achieve an equivalent total dose to the object. The total number of primaries within each simulation was increased by a factor of approximately 20 as compared to the fan beam approach.

The comparison between the final WET reconstruction and the true WET image is shown in figure 5.29, while figures 5.30 and 5.31 depict the WET profiles along the both dimensions of the phantom. The performance of the reconstruction in terms of RMSE, NRMSE, relative error and spatial resolution results is summarized in tables 5.18 to 5.20.

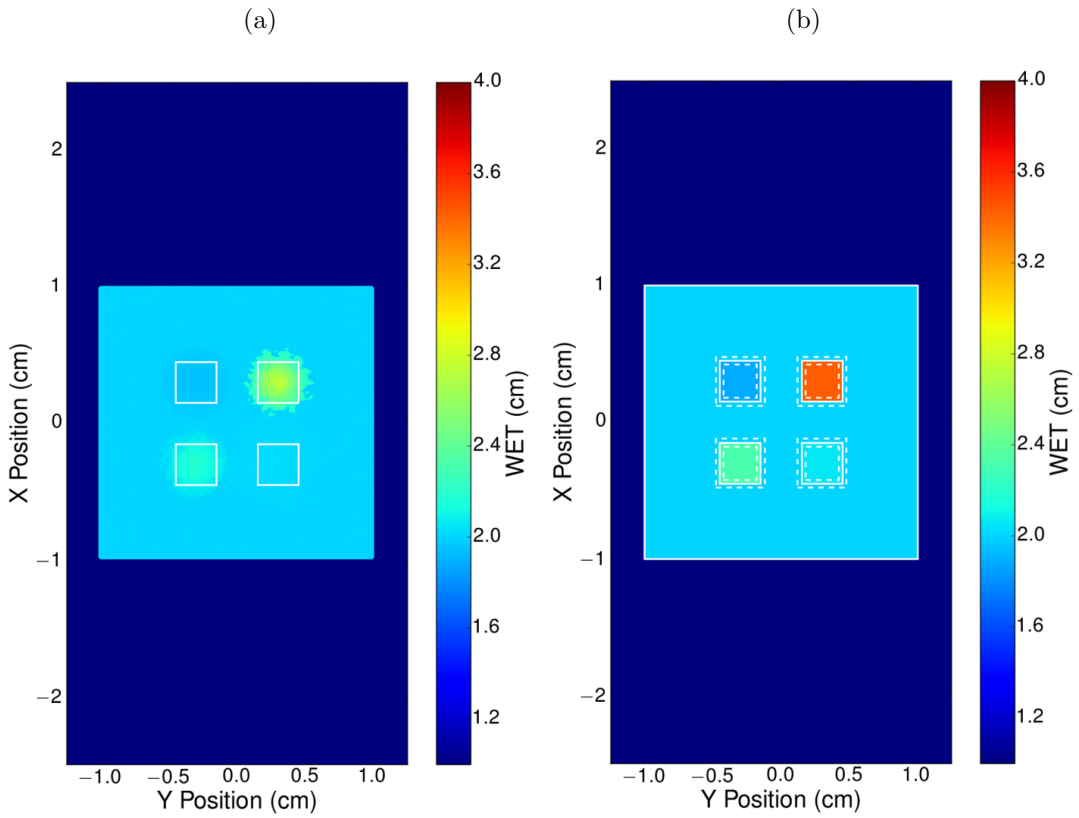

Figure 5.29: Comparison between (a) the reconstructed WET image and (b) the true WET image. In (b), from left to right, top to bottom the inserts are: adipose tissue, compact bone, PMMA and striated muscle.

(a) Adipose tissue and compact bone inserts.

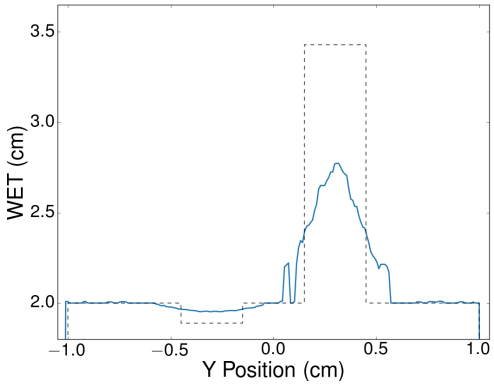

(b) PMMA and striated muscle inserts.

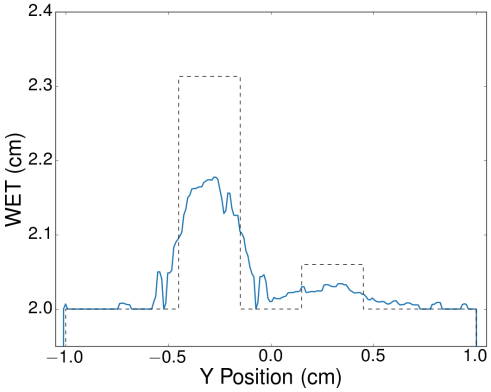

Figure 5.30: WET profiles along the horizontal dimension. The dashed lines correspond to the true WET profiles.

(a) PMMA and adipose tissue inserts.

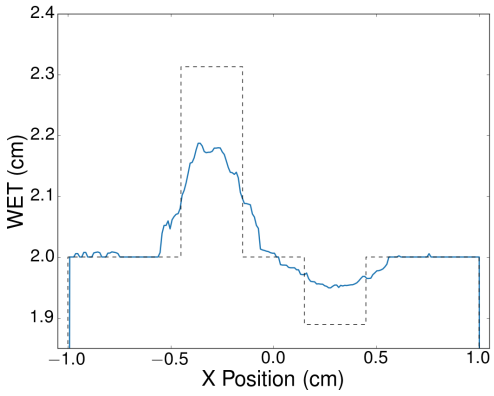

(b) Striated muscle and compact bone inserts.

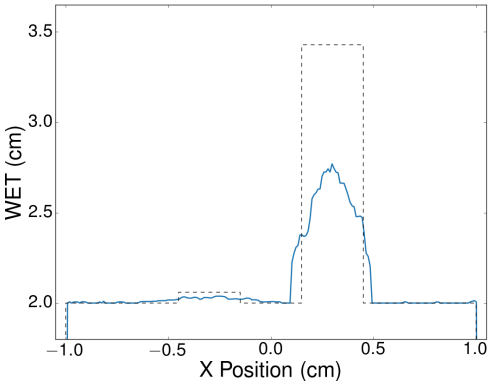

Figure 5.31: WET profiles along the vertical dimension. The dashed lines correspond to the true WET profiles.

Analyzing figure 5.29, the large impact of the increased multiple Coulomb scattering is confirmed. Besides the poor WET reconstruction of the compact bone insert, the *blurring* effect is again notorious. Figures 5.30 and 5.31 highlight the considerable decrease in the WET calculation accuracy. The underestimations of the compact bone, PMMA and striated muscle inserts are even more evident than in the previous approaches.

When it comes to the RMSE, NRMSE and relative error, the values presented in tables 5.18 and 5.19 also agree with the expectations. The largest discrepancies between reconstructed and true WET values are found for compact bone, with a relative error of approximately 26%, followed by the PMMA and adipose tissue, with

relative errors of roughly 7% and 4%, respectively. Contrarily to the other beam shapes, the mean WET of the striated muscle insert differed by 1.7% from the true WET. However, the mean WET of the water block was in better agreement with the true WET value.

Calculating the mean of the spatial resolution results, one can conclude that, for the broad field approach, the overall spatial resolution in the x dimension equals to (1.51 ± 0.24) mm and the overall spatial resolution in the y dimension equals to (1.67 ± 0.13) mm.

Table 5.18: RMSE and NRMSE values of the broad field approach.

Entity	RMSE (cm)	NRMSE (%)
Water	0.02	1.11
Adipose tissue	0.07	3.71
Compact bone	0.90	26.24
PMMA	0.17	7.53
Striated muscle	0.03	1.69

Table 5.19: Comparison between the true WET values and the mean WET values of the broad field approach in terms of the relative error.

Entity	True WET (cm)	Mean WET (cm)	Relative error (%)
Water	2.00	2.01	0.25
Adipose tissue	1.89	1.96	3.69
Compact bone	3.43	2.54	26.02
PMMA	2.31	2.14	7.44
Striated muscle	2.06	2.03	1.67

Table 5.20: Spatial resolution of the broad field approach.

Interface	Dimension	Spatial resolution (mm)
Adipose tissue/water	x	2.32
	y	1.78
Compact bone/water	x	1.07
	y	2.07
PMMA/water	x	1.47
	y	1.09
Striated muscle/water	x	1.18
	y	1.74

5.3 Number of Primaries Comparison

In this section, the image quality in terms of WET accuracy and spatial resolution is investigated as a function of the number of primaries and hence dose. Table 5.21 presents the common parameters to all the performed tests.

Table 5.21: Common parameters to the number of primaries tests.

Phantom-detector distance	1.5 cm
Energy range	45 – 75 MeV
Energy step	0.5 MeV
Beam shape	Merged fan beam
Beam width and spacing	1 mm

The total number of primaries within each simulation is directly related to the total dose delivered to the object. In other words, increasing/decreasing the total number of primaries by a factor of 10 increases/decreases the total dose by the same factor.

Up to this point, the number of primaries used for the individual fan beam simulations was 50 000. This translates into a total number of primaries of 100 000 and a total dose of approximately 69.7 mGy. For an increased number of primaries, the total number of primaries chosen for the individual fan beam simulations was 100 000. After the merging, that translated into a total number of primaries of 200 000 and a total dose of approximately 139.3 mGy. For a decreased number of primaries, the total number of primaries chosen for the individual fan beam simulations was 20 000. Ultimately, that translated into a total number of primaries of 40 000 and a total dose of approximately 27.9 mGy.

Figure 5.32 shows the comparison between the different final WET reconstructions and the true WET image, while figures 5.34 and 5.35 depict the different WET profiles along the both dimensions of the phantom. Tables 5.22 and 5.23 assess the performance of the reconstruction in terms of RMSE, NRMSE and relative error. The reason why no spatial resolution table is presented is that although the spatial resolution values are independent of the total number of primaries, the same does not happen with the performance of the reconstruction. A lower number of primaries implies noisier data and thus larger fluctuations. As a consequence, in some cases, the used method for spatial resolution assessment will not hold anymore. Figure 5.33 depicts one of those situations. Although a sigmoidal fit is performed, it does not follow the data points. Therefore, there will be no data close to the 25% and 75% points of the sigmoid, ultimately not allowing the calculation of spatial resolution values.

Comparing figures 5.32 (a) and (b), the decrease in the performance of the reconstruction of the former one is evident, especially in the case of water. However, in terms of the compact bone WET calculation, a lower total number of primaries seems to be beneficial, judging by figure 5.34 (a) and (d). In contrast, comparing figures 5.32 (b) and (c), there is a slightly worse performance in terms of the compact bone reconstruction of the latter one. This fact is also corroborated by figure 5.35 (a) and (d). Tables 5.22 and 5.23 support these findings.

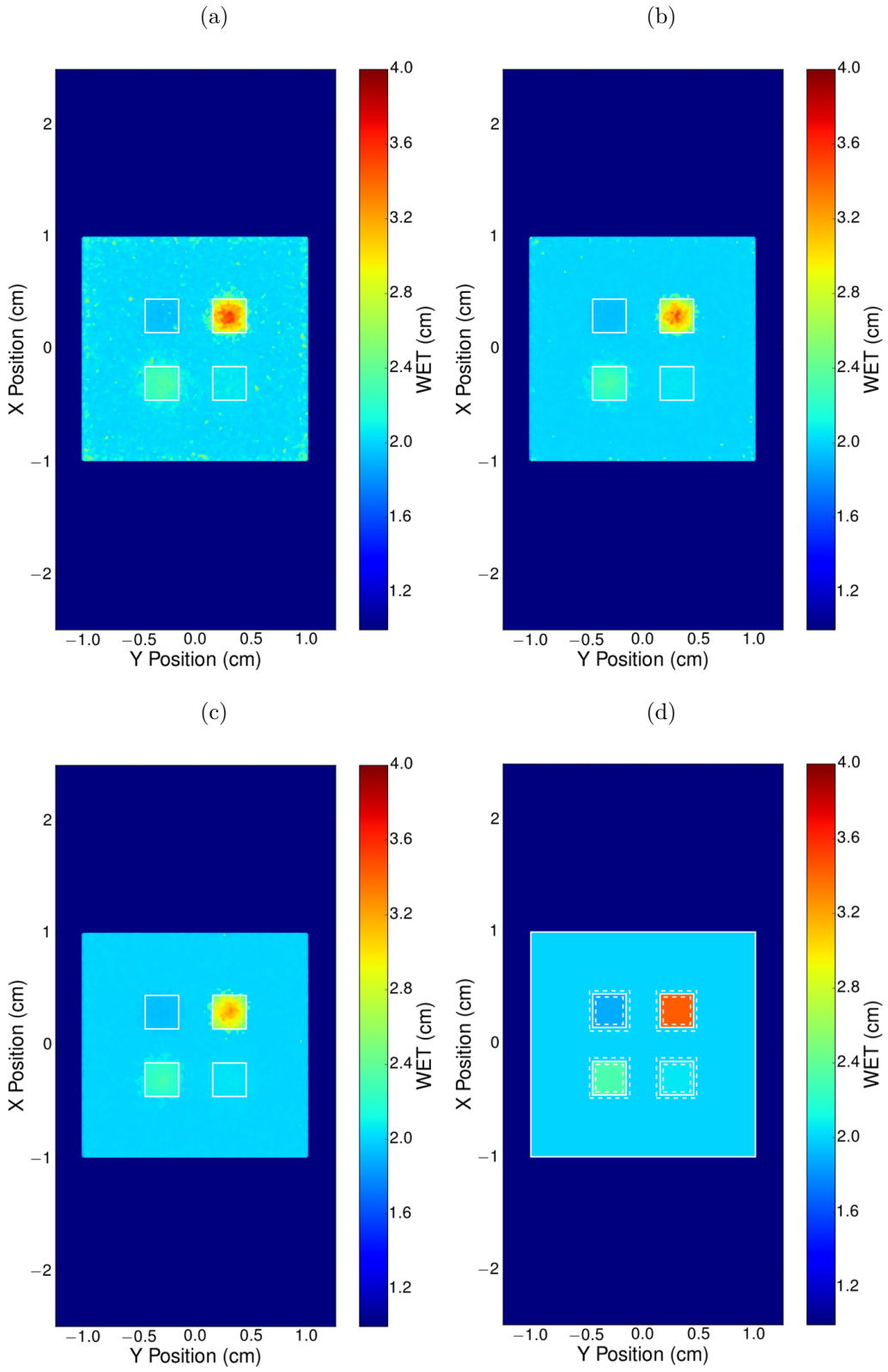

Figure 5.32: Comparison between the reconstructed WET images of (a) the decreased number of primaries, (b) the standard number of primaries, (c) the increased number of primaries and (d) the true WET image. In (d), from left to right, top to bottom the inserts are: adipose tissue, compact bone, PMMA and striated muscle.

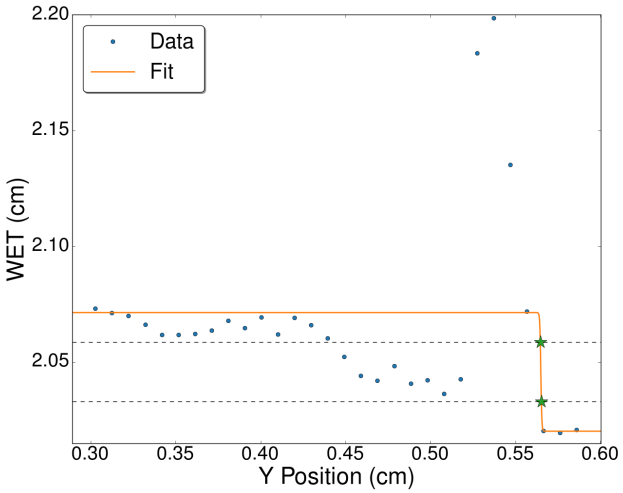

Figure 5.33: Example of a failed sigmoidal fit. Figure corresponds to the interface between striated muscle and water.

(a) Adipose tissue and compact bone inserts.

(b) PMMA and striated muscle inserts.

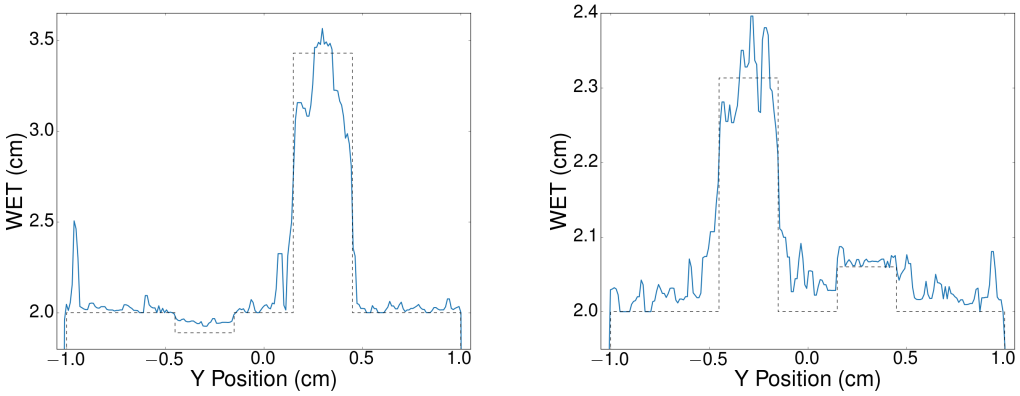

(c) PMMA and adipose tissue inserts.

(d) Striated muscle and compact bone inserts.

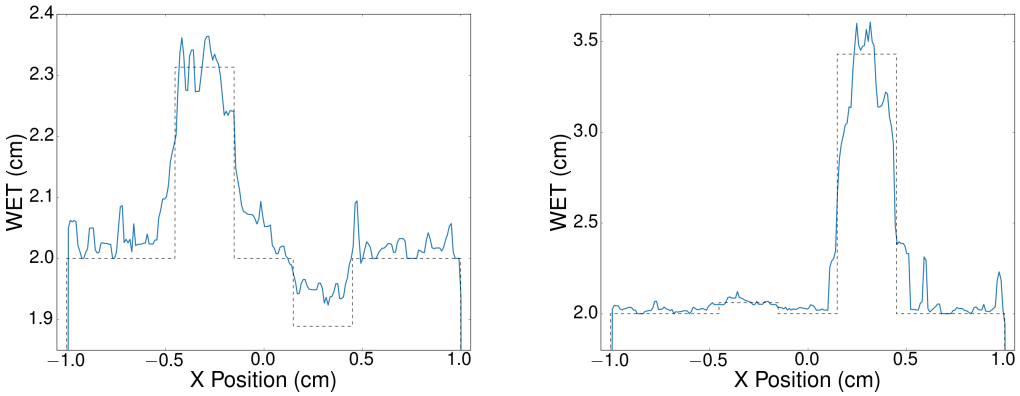

Figure 5.34: WET profiles of the decreased number of primaries test. The dashed lines correspond to the true WET profiles.

(a) Adipose tissue and compact bone inserts.

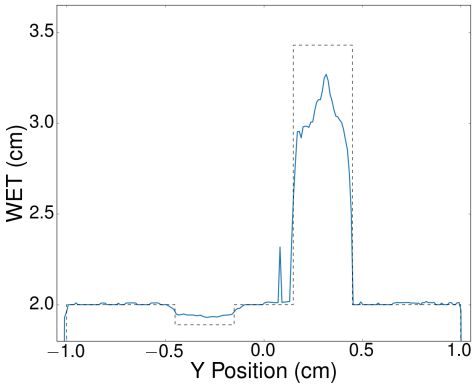

(b) PMMA and striated muscle inserts.

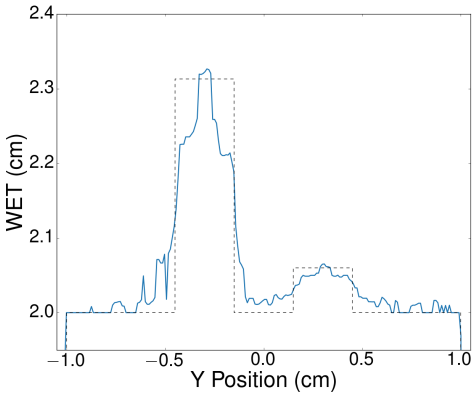

(c) PMMA and adipose tissue inserts.

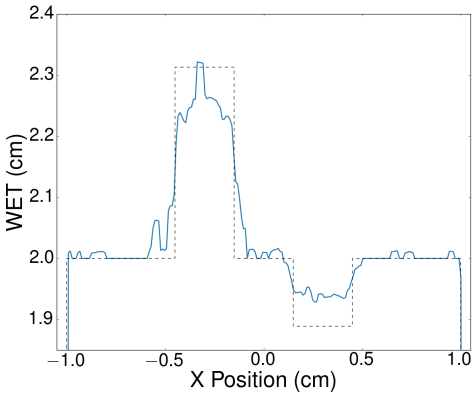

(d) Striated muscle and compact bone inserts.

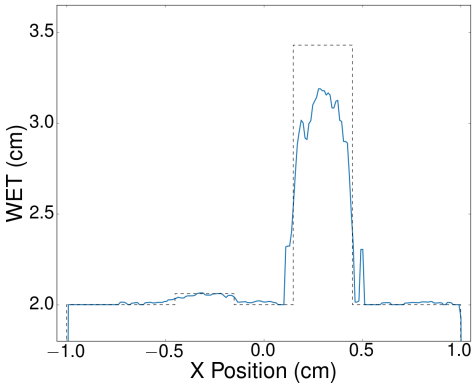

Figure 5.35: WET profiles of the increased number of primaries test. The dashed lines correspond to the true WET profiles.

Table 5.22: RMSE and NRMSE values of the number of primaries tests.

	Decreased number of primaries		Increased number of primaries	
Entity	RMSE (cm)	NRMSE (%)	RMSE (cm)	NRMSE (%)
Water	0.06	3.14	0.01	0.69
Adipose tissue	0.08	4.23	0.06	2.91
Compact bone	0.36	10.46	0.52	15.21
PMMA	0.06	2.39	0.09	3.90
Striated muscle	0.02	1.05	0.02	0.75

Table 5.23: Comparison between the true WET values and the mean WET values of the number of primaries tests in terms of the relative error.

		Decreased number of primaries	
Entity	True WET (cm)	Mean WET (cm)	Relative error (%)
Water	2.00	2.03	1.69
Adipose tissue	1.89	1.96	3.72
Compact bone	3.43	3.13	8.70
PMMA	2.31	2.29	1.20
Striated muscle	2.06	2.06	0.19
		Increased number of primaries	
Entity	True WET (cm)	Mean WET (cm)	Relative error (%)
Water	2.00	2.01	0.33
Adipose tissue	1.89	1.94	2.89
Compact bone	3.43	2.93	14.57
PMMA	2.31	2.23	3.56
Striated muscle	2.06	2.05	0.66

A lower number of primaries provides a relative error between reconstructed and true WET values of 8.7% in contrast to the 14.6% of a higher number of primaries. Furthermore, the WET accuracies of PMMA and striated muscle are enhanced in the former one as compared to all the other particle numbers. However, decreasing the number of primaries has a detrimental effect on the WET calculation of water and adipose tissue.

Taking a look at figure 5.36, it is easier to state that different total numbers of primaries influence the NRMSE values of the several areas of interest in distinct ways. In conclusion, WET resolution seems to be better for lower doses, being this potentially explained by effects caused by lower statistics. However, no spatial resolution information can be obtained and thus an intermediate number of primaries and, consequently, an intermediate dose represents a better option for imaging.

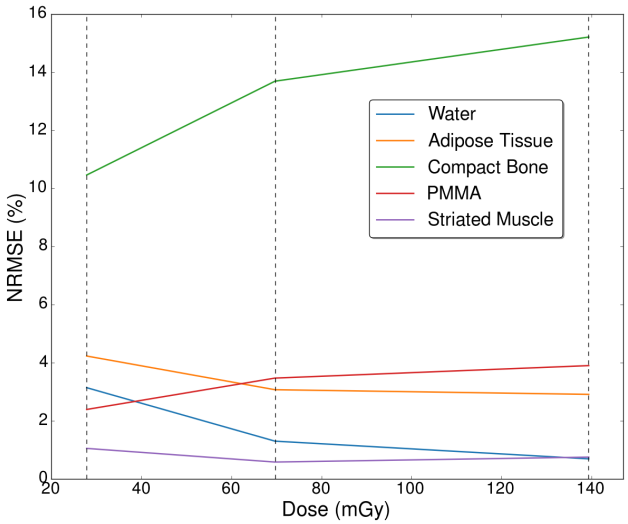

Figure 5.36: Comparison between different total doses to the object in terms of the NRMSE values. The vertical lines correspond to the tested doses.

In terms of similar studies, Schneider *et al.* used, in contrast to the approach proposed in this thesis, a proton-tracking system consisting of a 214 MeV proton beam with *a spot size of 15 × 15 mm² FWHM* [59] to obtain radiographic images of a canine subject. In this publication, the WET values were determined with a precision of 0.6 mm and the spatial resolution, stated to be limited by the lateral scattering of protons, *by measuring for each proton separately its coordinate in front of and behind the patient was approximately 1 mm* [59], in contrast to the (0.59 ± 0.02) mm and (0.67 ± 0.01) mm of the merged fan beam approach. A total dose exposure of 0.03 mGy was obtained, being this result significantly smaller than the 27.9,

69.7 and 139.3 mGy provided by the tests performed in this section [59]. In 2017, a group in Dresden proposed a method to *perform dual-energy proton radiography for inline positioning verification and treatment planning* [88]. With that approach and a 150 MeV 10 × 10 cm^2 extended proton field, proton imaging doses ranged from 274 mGy to 6.5 mGy, similarly to the ones presented, proving that *rigid registration could even be reproducibly achieved for a high noise level (doses as low as 22 mGy)* [88]. A positioning uncertainty of approximately 0.6 mm was obtained. Sadrozinski *et al.* reported on *the operation and performance tests of a preclinical head scanner developed for pCT*. With 200 MeV protons, the tracking detectors allowed a relative stopping power accuracy better than 1% being the dose required for a complete scan equal to approximately 1.1 mGy [89].

5.4 Phantom-Detector Distance Comparison

In this section, the impact of changing the distance between the phantom and the detector will be shown and analyzed. Spatial resolution is mainly determined by scattering. By changing the distance between the phantom and the detector, the overall spatial resolution was hence the quantity of interest in this study. Table 5.24 presents the common parameters to all the performed tests.

Table 5.24: Common parameters to the phantom-detector distance tests.

Energy range	45 – 75 MeV
Energy step	0.5 MeV
Beam shape	y fan beam
Beam width and spacing	1 mm
Total number of particles	128 000 000

Up to this point, the phantom-detector distance was set to 1.5 cm. Decreasing this distance implies having the detector rather close to the subject. In a potential experimental setup, movement of the phantom is required, which makes smaller distances unfeasible. Therefore, only simulations with increased distances of 2.0, 2.5 and 3.0 cm are shown in this section.

Figure 5.38 shows the comparison between the different final WET reconstructions and the true WET image, while figures 5.39 and 5.40 depict the WET profiles along

the both dimensions of the phantom. In terms of RMSE, NRMSE, relative error and spatial resolution results, tables 5.25 to 5.27 allow to draw conclusions about the performance and image quality of the reconstructions.

Only the spatial resolution of a phantom-detector distance of 2.0 cm is presented. The reason for this is that when increasing the air gap between the phantom and the detector, the over and underestimations of the WET values get worse in some cases (figures 5.39 and 5.40). As a result, when assessing the spatial resolution, the fitted sigmoidal function is steeper (figure 5.37). Consequently, the spatial resolution seems to be better in the dimension of the fan beam movement. Because this is in contrast to the expectations, no spatial resolutions results are shown for the 2.5 cm and 3.0 cm distances between the phantom and the detector.

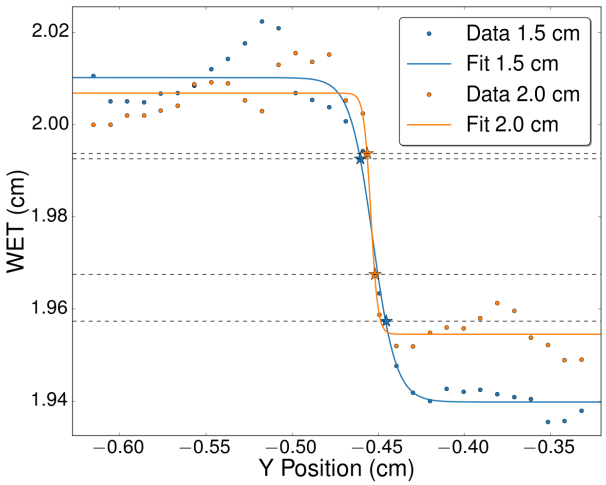

Figure 5.37: Comparison between using a 1.5 cm and a 2.0 cm distance between the phantom and the detector in terms of the sigmoidal fit of the horizontal dimension of the adipose tissue/water interface. The horizontal lines correspond to the 25% and 75% of each one of the sigmoids.

Comparing figure 5.38 (a) with figure 5.10, the major noticeable difference is in terms of the compact bone WET reconstruction. Increasing the distance between the phantom and the detector clearly has a detrimental effect in this case. This fact is even more evident in figure 5.38 (b) and (c). Furthermore, tables 5.25 and 5.26 demonstrate that the agreement between reconstructed and true WET values of the reconstruction decreases not only for compact bone, but also for the remaining areas of interest. Figure 5.41 shows the NRMSE as a function of the phantom-detector distance. One can easily conclude that with increasing distances the accuracy of the WET reconstruction decreases.

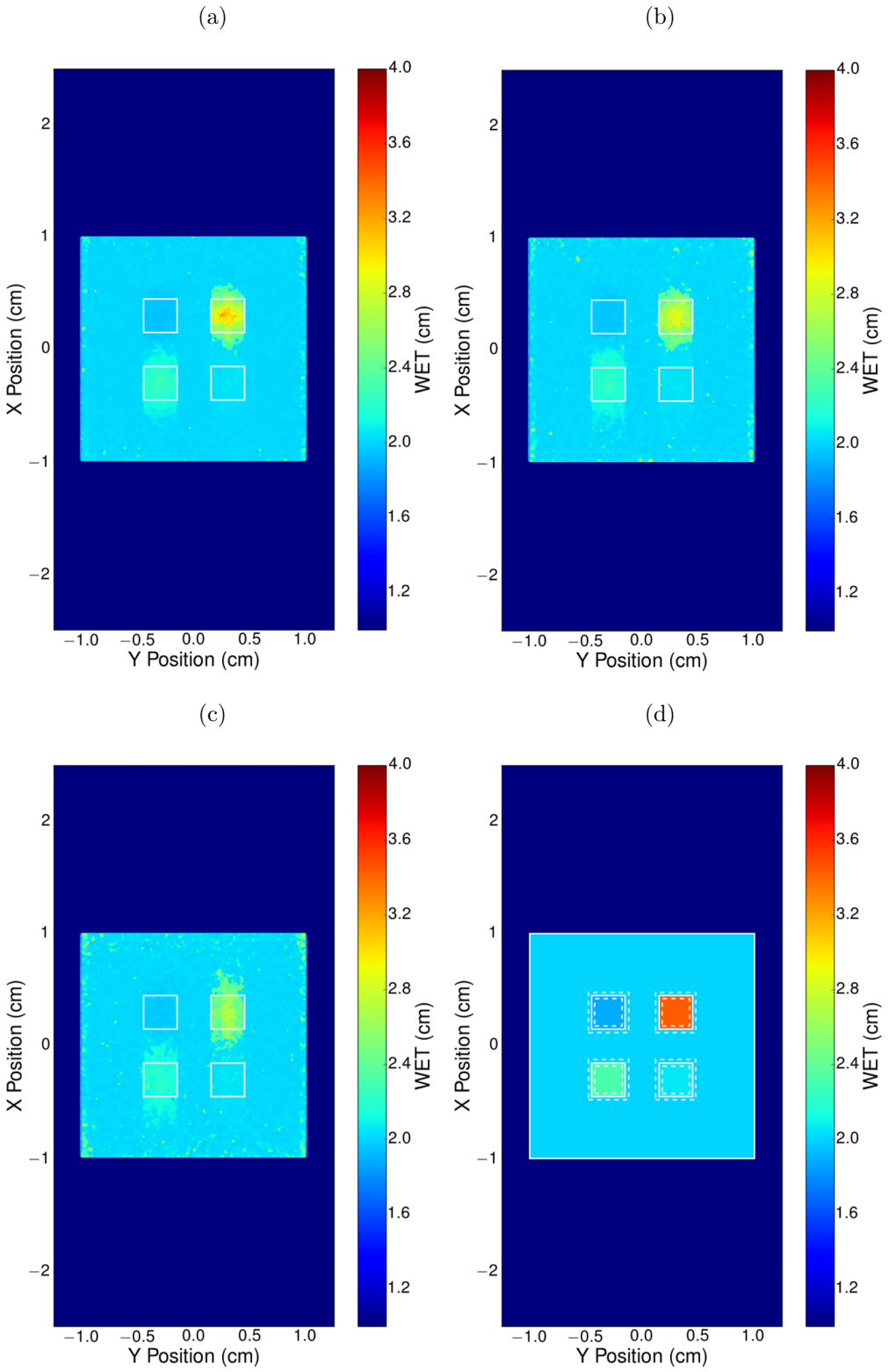

Figure 5.38: Comparison between the reconstructed WET images of (a) a phantom-detector distance of 2.0 cm, (b) a phantom-detector distance of 2.5 cm, (c) a phantom-detector distance of 3.0 cm and (d) the true WET image. In (d), from left to right, top to bottom the inserts are: adipose tissue, compact bone, PMMA and striated muscle.

(a) Adipose tissue and compact bone inserts.

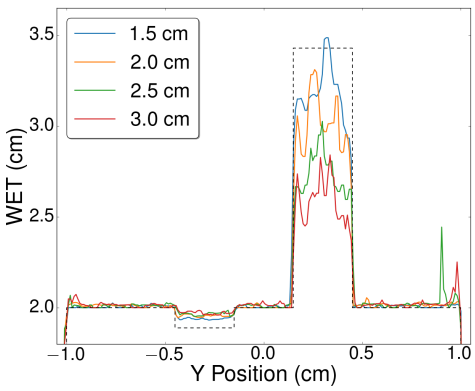

(b) PMMA and striated muscle inserts.

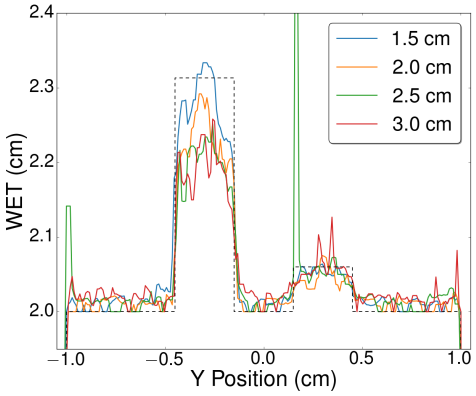

Figure 5.39: WET profiles along the horizontal dimension. The dashed lines correspond to the true WET profiles.

(a) PMMA and adipose tissue inserts.

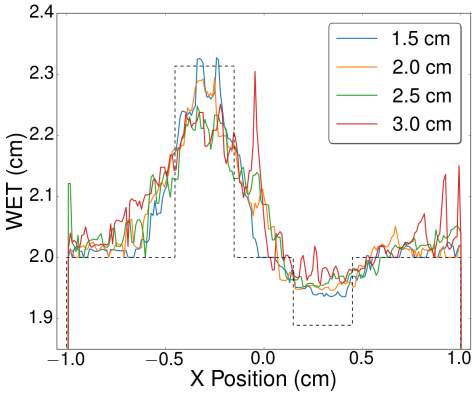

(b) Striated muscle and compact bone inserts.

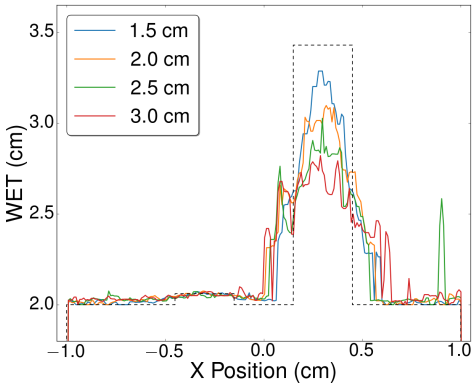

Figure 5.40: WET profiles along the vertical dimension. The dashed lines correspond to the true WET profiles.

Table 5.25: RMSE and NRMSE values of the phantom-detector distance tests.

	2.0 cm		2.5 cm		3.0 cm	
Entity	RMSE (cm)	NRMSE (%)	RMSE (cm)	NRMSE (%)	RMSE (cm)	NRMSE (%)
Water	0.05	2.56	0.07	3.26	0.08	3.99
Adipose tissue	0.07	3.56	0.08	4.13	0.09	4.63
Compact bone	0.64	18.60	0.74	21.62	0.90	26.28
PMMA	0.11	4.71	0.13	5.52	0.15	6.45
Striated muscle	0.02	0.85	0.03	1.36	0.02	1.06

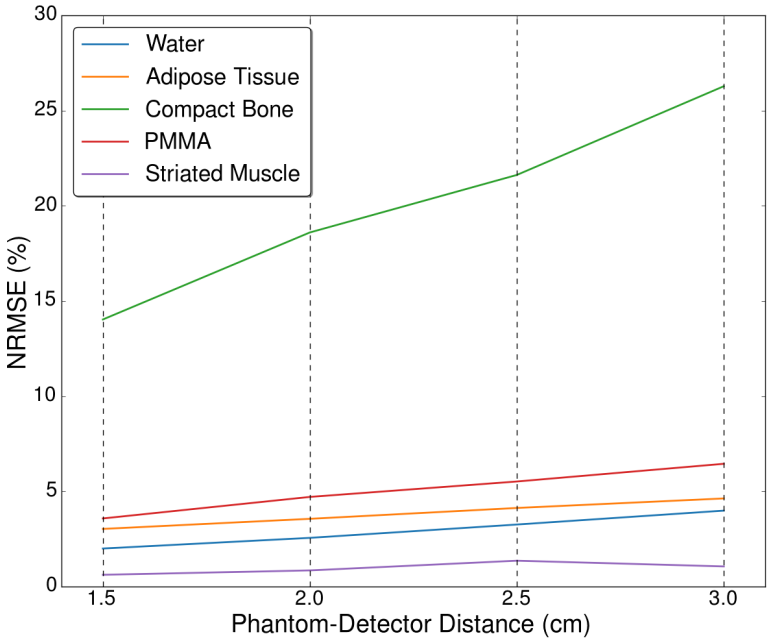

Figure 5.41: Comparison between different phantom-detector distances in terms of the NRMSE values.

Table 5.26: Comparison between the true WET values and the mean WET values of the phantom-detector distance tests in terms of the relative error.

		2.0 cm	
Entity	True WET (cm)	Mean WET (cm)	Relative error (%)
Water	2.00	2.02	1.02
Adipose tissue	1.89	1.96	3.54
Compact bone	3.43	2.81	17.91
PMMA	2.31	2.21	4.44
Striated muscle	2.06	2.05	0.62
		2.5 cm	
Entity	True WET (cm)	Mean WET (cm)	Relative error (%)
Water	2.00	2.03	1.39
Adipose tissue	1.89	1.97	4.10
Compact bone	3.43	2.70	21.29
PMMA	2.31	2.19	5.34
Striated muscle	2.06	2.05	0.47
		3.0 cm	
Entity	True WET (cm)	Mean WET (cm)	Relative error (%)
Water	2.00	2.04	1.81
Adipose tissue	1.89	1.98	4.58
Compact bone	3.43	2.54	26.04
PMMA	2.31	2.17	6.06
Striated muscle	2.06	2.05	0.41

Table 5.27: Spatial resolution of the 2.0 cm phantom-detector distance test.

Interface	Dimension	Spatial resolution (mm)
Adipose tissue/water	x	1.23
	y	0.06
Compact bone/water	x	3.95
	y	0.13
PMMA/water	x	4.16
	y	0.24
Striated muscle/water	x	5.23
	y	0.67

By all the results presented in this section, one can conclude that a 1.5 cm distance between the phantom and the detector represents a better compromise between acceptable spatial resolution and practicability in terms of geometrical constraints.

5.5 Time Estimation for Radiographic Imaging

Considering a detector with a frame rate of 5 frames per second, the required time for irradiation/imaging (t_i) would be 200 ms. Concerning object movement, one can assume that shifting an object by a small distance (1 mm) should take around 0.5 s (t_m). However, when it comes to the energy change, the required time (t_e) depends, for example, on the used accelerator. Using a synchrotron, changing the energy can take up to 3 s, while in the case of cyclotrons this time can be reduced down to 100 ms [90].

Bearing in mind the studied beam shapes and their number of beams (n_b), 441, 42 and 1, respectively for spot scanning, merged fan beam and broad field, the time required for obtaining a radiographic image with 61 energy shots (n_e) was estimated (section 4.6, equations 4.11 and 4.12) (table 5.28).

Analyzing the results in table 5.28, one can conclude that, in an experiment, a spot scanning approach is not feasible due to its long times.

Table 5.28: Estimated times for obtaining radiographic images with the spot scanning, merged fan beam and broad field approaches.

	Accelerator	
Approach	Synchrotron	Cyclotron
Spot scanning	5.5 h	138 min
Merged fan beam	33 min	14 min
Broad field	4 min	19 s

Schneider *et al.* used a proton-tracking system to obtain radiographic images of a canine subject with an acquisition time of approximately 20 seconds [59], comparable to the time obtained when using the broad field approach with a cyclotron. Also with a proton-tracking system, Sadrozinski *et al.* performed full 360° scans within less than 7 minutes [89], in contrast to the 14 minutes obtained with the proposed proton-integrating system when using the merged fan beam approach with a cyclotron. Later on, Johnson *et al.* showed that the same system *is able to make a complete CT scan in six minutes or less, or a single radiograph in a few seconds* [91]. One can therefore conclude that proton-tracking systems provide smaller acquisition times when compared to proton-integrating systems.

6

Conclusion and Outlook

In this work, the feasibility of a novel small-animal proton radiographic imaging setup based on a pixelated silicon detector and the concept of energy stacking was investigated. Several studies were carried out in order to obtain planar radiographies quantified in terms of WET of a $2 \times 2 \times 2$ cm^3 water block including inserts of adipose tissue, compact bone, PMMA, and striated muscle. The quality of the obtained images was assessed in terms of RMSE, NRMSE, relative error and spatial resolution. Moreover, the total dose delivered to the object and the required acquisition duration were estimated.

For an energy range of 45 to 75 MeV, with 0.5 MeV steps, and a phantom-detector distance of 1.5 cm, the energy modulated image reconstruction of the phantom, using a combination of two perpendicular rectangular proton beams, the so-called merged fan beam approach, the mean reconstructed WET was in good agreement with the true WET values, being the relative error of only approximately 3.9%. Spatial resolution was found to be (0.59 ± 0.02) mm and (0.67 ± 0.01) mm in the vertical and horizontal dimensions, respectively. With a total dose to the object of 69.7 mGy, the entire radiographic acquisition time for this approach would range from 14 to 33 minutes, depending on whether the used accelerator would be a cyclotron or a synchrotron. A lower imaging dose can be obtained by reducing the number of protons for each fan beam and each energy. At 27.9 mGy, differences between reconstructed and true WET values were still satisfactory, having a mean accuracy of about 96.9%.

Replacing the fan beams with 1 mm FWHM pencil beams, the so-called spot scanning approach, provided WET calculations with an agreement of about 98.6% with the true WET values and improved spatial resolution values of (0.100 ± 0.001) mm and (0.34 ± 0.18) mm, for the same x and y dimensions. The total time required for acquisition, with the same total dose being delivered, would be equal to, approximately, 5.5 hours using a synchrotron, and 138 minutes using a cyclotron.

Finally, the use of a homogeneous beam covering the entire phantom, the so-called broad field approach, resulted in WET calculations with an agreement of roughly 92.2% with the true WET values and spatial resolution values of (1.51 ± 0.24) mm in the vertical dimension and (1.67 ± 0.13) mm in the horizontal dimension. The entire radiography would be obtained, approximately, within 4 minutes using a synchrotron and within 19 seconds using a cyclotron.

Testing the influence of the distance between the phantom and the detector demonstrated that increased distances, when compared to the 1.5 cm used for the other tests, reduce the agreement between reconstructed and true WET values, not even providing reliable spatial resolution information.

In conclusion, a proton radiographic imaging setup consisting of a combination of perpendicular rectangular beams provides a good compromise between image quality and acquisition time for the subject, achieving sub-millimeter spatial resolutions in both dimensions. However, due to the relatively high delivered doses, such a technique cannot be extended to proton tomography, where multiple projections are required. A possible approach for decreasing the dose values would be to use a smaller energy range, still suitable for the object being studied, resulting in fewer irradiations.

In terms of improving the reconstruction method itself, further studies could be carried out using different filtering techniques and, for example, regularization techniques to post-process the data. Additionally, the benefits of including prior knowledge concerning the object, for example, from previous X-ray CT acquisitions, and additional scattering information coming from the adjacent beams could be assessed, and machine learning techniques could be implemented. Finally, using more realistic beams and objects would significantly improve the reliability of the proposed setup in terms of practical feasibility.

Bibliography

[1] M. Naghavi *et al.*, "Global, regional, and national age-sex specific mortality for 264 causes of death, 1980–2016: a systematic analysis for the Global Burden of Disease Study 2016," *The Lancet*, vol. 390, pp. 1151–1210, sep 2017.

[2] R. L. Siegel, K. D. Miller, and A. Jemal, "Cancer statistics, 2016," *CA: A Cancer Journal for Clinicians*, vol. 66, pp. 7–30, jan 2016.

[3] M. Roser and H. Ritchie, "Cancer," *Published online at Our World In Data*, 2018.

[4] H. Jayasekara, R. J. MacInnis, R. Room, and D. R. English, "Long-Term Alcohol Consumption and Breast, Upper Aero-Digestive Tract and Colorectal Cancer Risk: A Systematic Review and Meta-Analysis," *Alcohol and Alcoholism*, vol. 51, pp. 315–330, may 2016.

[5] B. W. Stewart, C. Wild, International Agency for Research on Cancer, and World Health Organization, *World Cancer Report 2014*. World Health Organization, 2004.

[6] K. D. Miller *et al.*, "Cancer treatment and survivorship statistics, 2016," *CA: A Cancer Journal for Clinicians*, vol. 66, pp. 271–289, jul 2016.

[7] L. Grevillot, *Monte Carlo simulation of active scanning proton therapy system with Gate/Geant4 : Towards a better patient dose quality assurance*. Phd thesis, Institut National des Sciences Appliquées de Lyon, oct 2011.

[8] M. Teoh *et al.*, "Volumetric modulated arc therapy: a review of current literature and clinical use in practice.," *The British journal of radiology*, vol. 84, pp. 967–96, nov 2011.

[9] A. Taylor and M. E. B. Powell, "Intensity-modulated radiotherapy–what is it?," *Cancer imaging : the official publication of the International Cancer Imaging Society*, vol. 4, pp. 68–73, mar 2004.

[10] W. D. Newhauser and R. Zhang, "The physics of proton therapy," *Physics in Medicine and Biology*, vol. 60, pp. R155–R209, apr 2015.

[11] R. R. Wilson, "Radiological Use of Fast Protons," *Radiology*, vol. 47, pp. 487–491, nov 1946.

[12] E. Testa *et al.*, "Dose profile monitoring with carbon ions by means of prompt-gamma measurements," *Nuclear Instruments and Methods in Physics Research Section B: Beam Interactions with Materials and Atoms*, vol. 267, pp. 993–996, mar 2009.

[13] K. Parodi *et al.*, "PET/CT imaging for treatment verification after proton therapy: a study with plastic phantoms and metallic implants.," *Medical physics*, vol. 34, pp. 419–35, feb 2007.

[14] M. Moteabbed, S. España, and H. Paganetti, "Monte Carlo patient study on the comparison of prompt gamma and PET imaging for range verification in proton therapy," *Physics in Medicine and Biology*, vol. 56, pp. 1063–1082, feb 2011.

[15] S. Lehrack *et al.*, "Submillimeter ionoacoustic range determination for protons in water at a clinical synchrocyclotron," *Physics in Medicine & Biology*, vol. 62, pp. L20–L30, aug 2017.

[16] A.-C. Knopf and A. Lomax, "In vivo proton range verification: a review," *Physics in Medicine and Biology*, vol. 58, pp. R131–R160, aug 2013.

[17] N. Depauw and J. Seco, "Sensitivity study of proton radiography and comparison with kV and MV x-ray imaging using GEANT4 Monte Carlo simulations," *Physics in Medicine and Biology*, vol. 56, pp. 2407–2421, apr 2011.

[18] "Small Animal Radiation Research Platform." Available at https://xstrahl.com/life-science-systems/small-animal-radiation-research-platform.

[19] E. B. Podgorsak, *Radiation Physics for Medical Physicists*. Biological and Medical Physics, Biomedical Engineering, Berlin, Heidelberg: Springer Berlin Heidelberg, 2010.

[20] H. Nikjoo, S. Uehara, and D. Emfietzoglou, *Interaction of radiation with matter*. CRC, 2012.

[21] W. R. Leo, *Techniques for Nuclear and Particle Physics Experiments*. Berlin, Heidelberg: Springer Berlin Heidelberg, 1994.

[22] H. Bethe, "Zur Theorie des Durchgangs schneller Korpuskularstrahlen durch Materie," *Annalen der Physik*, vol. 397, no. 3, pp. 325–400, 1930.

[23] F. Bloch, "Zur Bremsung rasch bewegter Teilchen beim Durchgang durch Materie," *Annalen der Physik*, vol. 408, no. 3, pp. 285–320, 1933.

[24] H. Paganetti, *Proton Therapy Physics*. Series in Medical Physics and Biomedical Engineering, CRC Press, 2012.

[25] M. Berger, J. Coursey, M. Zucker, and J. Chang, "PSTAR : Stopping Power and Range Tables for Protons," 2005. Available at https://physics.nist.gov/cgi-bin/Star/ap_table.pl.

[26] W. Barkas, *Nuclear Research Emulsions - Volume 1 Techniques and Theory*. Academic Press, 1963.

[27] D. Schardt, T. Elsässer, and D. Schulz-Ertner, "Heavy-ion tumor therapy: Physical and radiobiological benefits," *Reviews of Modern Physics*, vol. 82, pp. 383–425, feb 2010.

[28] S. M. Seltzer *et al.*, "Fundamental quantities and units for ionizing radiation," *Journal of the ICRU*, vol. 11, pp. 1–41, apr 2011.

[29] M. Würl, *Towards Offline PET Monitoring at a Cyclotron-Based Proton Therapy Facility*. Wiesbaden: Springer Fachmedien Wiesbaden, 2016.

[30] F. H. Attix, *Introduction to radiological physics and radiation dosimetry*. Wiley, 1986.

[31] W. H. Bragg and R. Kleeman, "On the α particles of radium, and their loss of range in passing through various atoms and molecules," *The London, Edinburgh, and Dublin Philosophical Magazine and Journal of Science*, vol. 10, pp. 318–340, sep 1905.

[32] R. Zhang and W. D. Newhauser, "Calculation of water equivalent thickness of materials of arbitrary density, elemental composition and thickness in proton beam irradiation," *Physics in Medicine and Biology*, vol. 54, pp. 1383–1395, mar 2009.

[33] N. Bohr, "On the constitution of atoms and molecules," *The London, Edinburgh, and Dublin Philosophical Magazine and Journal of Science*, vol. 26, pp. 1–25, jul 1913.

[34] P. Vavilov, "Ionization losses of high-energy heavy particles," *Zh.Eksp.Teor.Fiz.*, vol. 32, pp. 749–751, 1957.

[35] L. Landau, "On the energy loss of fast particles by ionization," *J.Phys.(USSR)*, vol. 8, pp. 201–205, 1944.

[36] B. Rossi, *High-energy particles.* New York: Prentice-Hall, 1952.

[37] G. Molière, "Theorie der Streuung schneller geladener Teilchen II. Mehrfach- und Vielfachstreuung," *Zeitschrift für Naturforschung A, Volume 3, Issue 2, pp.78-97*, vol. 3, pp. 78–97, 1948.

[38] V. L. Highland, "Some practical remarks on multiple scattering," *Nuclear Instruments and Methods*, vol. 129, pp. 497–499, nov 1975.

[39] R. Serber, "Nuclear Reactions at High Energies," *Physical Review*, vol. 72, pp. 1114–1115, dec 1947.

[40] International Commission on Radiation Units and Measurements., *Clinical Proton Dosimetry: Part I. Beam Production, Beam Delivery and Measurement of Absorbed Dose.* International Commission on Radiation Units and Measurements, 1998.

[41] S. Meyer, "A systematic Monte Carlo study of the influence of different acquisition and detector parameters on the image quality of carbon ion radiography and tomography using a range telescope," Master's thesis, Ludwig-Maximilians-Universität München, 2015.

[42] "Memo CP-C/347," 2004. Available at https://www-nds.iaea.org/nrdc/memo_cpc/cpc347.doc.

[43] International Atomic Energy Agency., *Absorbed Dose Determination in External Beam Radiotherapy.* International Atomic Energy Agency, 2000.

[44] J. Telsemeyer, O. Jäkel, and M. Martišíková, "Quantitative carbon ion beam radiography and tomography with a flat-panel detector," *Physics in Medicine and Biology*, vol. 57, pp. 7957–7971, dec 2012.

[45] G. Poludniowski, N. M. Allinson, and P. M. Evans, "Proton radiography and tomography with application to proton therapy.," *The British journal of radiology*, vol. 88, p. 20150134, sep 2015.

[46] A. M. Koehler, "Proton radiography.," *Science (New York, N.Y.)*, vol. 160, pp. 303–4, apr 1968.

[47] V. W. Steward and A. M. Koehler, "Proton radiography as a diagnostic tool," *AAPM Bulletin, AAPM Winter Meeting*, vol. 6 (4), p. 194, 1972.

[48] V. W. Steward and A. M. Koehler, "Proton beam radiography in tumor detection.," *Science (New York, N.Y.)*, vol. 179, pp. 913–4, mar 1973.

[49] V. W. Steward and A. M. Koehler, "Proton Radiographic Detection of Strokes," *Nature*, vol. 245, pp. 38–40, sep 1973.

[50] V. W. Steward and A. M. Koehler, "Proton Radiography in the Diagnosis of Breast Carcinoma," *Radiology*, vol. 110, pp. 217–221, jan 1974.

[51] V. W. Steward and A. M. Koehler, "Proton radiography of a human brain tumor within the skull: a preliminary report.," *Surgical neurology*, vol. 2, pp. 283–4, jul 1974.

[52] A. M. Cormack and A. M. Koehler, "Quantitative proton tomography: preliminary experiments," *Physics in Medicine and Biology*, vol. 21, p. 007, jul 1976.

[53] K. M. Hanson *et al.*, "Computed tomography using proton energy loss," *Physics in Medicine and Biology*, vol. 26, pp. 965–983, nov 1981.

[54] K. M. Hanson, "Proton Computed Tomography," *IEEE Transactions on Nuclear Science*, vol. 26, pp. 1635–1640, feb 1979.

[55] J. M. Slater, D. W. Miller, and J. O. Archambeau, "Development of a hospital-based proton beam treatment center.," *International journal of radiation oncology, biology, physics*, vol. 14, pp. 761–75, apr 1988.

[56] U. Schneider and E. Pedroni, "Proton radiography as a tool for quality control in proton therapy," *Medical Physics*, vol. 22, pp. 353–363, apr 1995.

[57] P. Zygmanski, K. P. Gall, M. S. Rabin, and S. J. Rosenthal, "The measurement of proton stopping power using proton-cone-beam computed tomography.," *Physics in medicine and biology*, vol. 45, pp. 511–28, feb 2000.

[58] P. Pemler *et al.*, "A detector system for proton radiography on the gantry of the Paul-Scherrer-Institute," *Nuclear Instruments and Methods in Physics Research Section A: Accelerators, Spectrometers, Detectors and Associated Equipment*, vol. 432, pp. 483–495, aug 1999.

[59] U. Schneider *et al.*, "First proton radiography of an animal patient," *Medical Physics*, vol. 31, pp. 1046–1051, apr 2004.

[60] U. Amaldi *et al.*, "Advanced Quality Assurance for CNAO," *Nuclear Instruments and Methods in Physics Research Section A: Accelerators, Spectrometers, Detectors and Associated Equipment*, vol. 617, pp. 248–249, may 2010.

[61] U. Amaldi *et al.*, "Construction, test and operation of a proton range radiography system," *Nuclear Instruments and Methods in Physics Research Section A: Accelerators, Spectrometers, Detectors and Associated Equipment*, vol. 629, pp. 337–344, feb 2011.

[62] H. F.-W. Sadrozinski *et al.*, "Development of a Head Scanner for Proton CT.," *Nuclear instruments & methods in physics research. Section A, Accelerators, spectrometers, detectors and associated equipment*, vol. 699, pp. 205–210, jan 2013.

[63] R. P. Johnson *et al.*, "Results from a pre-clinical head scanner for proton CT," in *2014 IEEE Nuclear Science Symposium and Medical Imaging Conference (NSS/MIC)*, pp. 1–5, IEEE, nov 2014.

[64] M. Bucciantonio *et al.*, "Development of a fast proton range radiography system for quality assurance in hadrontherapy," *Nuclear Instruments and Methods in Physics Research Section A: Accelerators, Spectrometers, Detectors and Associated Equipment*, vol. 732, pp. 564–567, dec 2013.

[65] M. Scaringella *et al.*, "A proton Computed Tomography based medical imaging system," *Journal of Instrumentation*, vol. 9, pp. C12009–C12009, dec 2014.

[66] Y. Saraya *et al.*, "Study of spatial resolution of proton computed tomography using a silicon strip detector," *Nuclear Instruments and Methods in Physics Research Section A: Accelerators, Spectrometers, Detectors and Associated Equipment*, vol. 735, pp. 485–489, jan 2014.

[67] J. Taylor *et al.*, "Proton tracking for medical imaging and dosimetry," *Journal of Instrumentation*, vol. 10, pp. C02015–C02015, feb 2015.

[68] M. Testa *et al.*, "Proton radiography and proton computed tomography based on time-resolved dose measurements," *Physics in Medicine and Biology*, vol. 58, pp. 8215–8233, nov 2013.

[69] J. Seco and N. Depauw, "Proof of principle study of the use of a CMOS active pixel sensor for proton radiography," *Medical Physics*, vol. 38, pp. 622–623, jan 2011.

[70] G. Poludniowski *et al.*, "Proton-counting radiography for proton therapy: a proof of principle using CMOS APS technology.," *Physics in medicine and biology*, vol. 59, pp. 2569–81, jun 2014.

[71] G. Battistoni *et al.*, "The FLUKA code: description and benchmarking," in *AIP Conference Proceedings*, vol. 896, pp. 31–49, AIP, mar 2007.

[72] A. Ferrari *et al.*, "FLUKA: a multi-particle transport code (Program version 2011)," *CERN 2005-10 (2005), INFN/TC 05/11, SLAC-R-773*, 2011.

[73] F. Sommerer *et al.*, "Investigating the accuracy of the FLUKA code for transport of therapeutic ion beams in matter," *Physics in Medicine and Biology*, vol. 51, pp. 4385–4398, sep 2006.

[74] K. Parodi, A. Ferrari, F. Sommerer, and H. Paganetti, "Clinical CT-based calculations of dose and positron emitter distributions in proton therapy using the FLUKA Monte Carlo code," *Physics in Medicine and Biology*, vol. 52, pp. 3369–3387, jul 2007.

[75] T. T. Böhlen *et al.*, "A Monte Carlo-based treatment-planning tool for ion beam therapy," *Journal of Radiation Research*, vol. 54, pp. i77–i81, jul 2013.

[76] J. Bauer *et al.*, "Integration and evaluation of automated Monte Carlo simulations in the clinical practice of scanned proton and carbon ion beam therapy," *Physics in Medicine and Biology*, vol. 59, pp. 4635–4659, aug 2014.

[77] V. Vlachoudis, *Flair: A powerful but user friendly graphical interface for FLUKA*. Proc. Int. Conf. on Mathematics, Computational Methods & Reactor Physics (M&C 2009), Saratoga Springs, New York., 2009.

[78] I. Moskal, "Investigations on proton radiography with a compact planar detector," tech. rep., Ludwig-Maximilians-Universität München, München, 2017.

[79] "RadEye™1 Large Area Imager," 2001. Available at http://pdf.directindustry.com/pdf/rad-icon-imaging-corporation/radeye-large-area-image-sensors/21698-37747.html.

[80] T. Graeve and G. P. Weckler, "High-resolution CMOS imaging detector," in *Proc. SPIE 4320, Medical Imaging 2001: Physics of Medical Imaging* (L. E. Antonuk and M. J. Yaffe, eds.), vol. 4320, p. 68, International Society for Optics and Photonics, jun 2001.

[81] S. Reinhardt, *Detection of laser-accelerated protons.* PhD thesis, Ludwig–Maximilians–Universität München, 2012.

[82] T. Bortfeld, "An analytical approximation of the Bragg curve for therapeutic proton beams," *Medical Physics*, vol. 24, pp. 2024–2033, dec 1997.

[83] S. N. Boon, *Dosimetry and quality control of scanning proton beams.* PhD thesis, University of Groningen, 1998.

[84] H. Pettersen *et al.*, "Accuracy of parameterized proton range models; A comparison," *Radiation Physics and Chemistry*, vol. 144, pp. 295–297, mar 2018.

[85] S. Meyer *et al.*, "Comparative Monte Carlo study on the performance of integration- and list-mode detector configurations for carbon ion computed tomography," *Physics in Medicine and Biology*, vol. 62, pp. 1096–1112, feb 2017.

[86] N. Krah *et al.*, "An advanced image processing method to improve the spatial resolution of ion radiographies," *Physics in Medicine and Biology*, vol. 60, pp. 8525–8547, nov 2015.

[87] J. Seco *et al.*, "Characterizing the modulation transfer function (MTF) of proton/carbon radiography using Monte Carlo simulations," *Medical Physics*, vol. 40, p. 091717, sep 2013.

[88] J. Müller *et al.*, "Proton radiography for inline treatment planning and positioning verification of small animals," *Acta Oncologica*, vol. 56, pp. 1399–1405, nov 2017.

[89] H. F.-W. Sadrozinski *et al.*, "Operation of the Preclinical Head Scanner for Proton CT.," *Nuclear instruments & methods in physics research. Section A, Accelerators, spectrometers, detectors and associated equipment*, vol. 831, pp. 394–399, sep 2016.

[90] W. Kleeven, "IBA Proton Therapy Systems - Accelerators, beamlines and gantry technology," tech. rep., Belgian Society for Radiation Protection, 2007.

[91] R. Johnson *et al.*, "Results from a Prototype Proton-CT Head Scanner," *Physics Procedia*, vol. 90, pp. 209–214, jan 2017.